Dissertation

VTT PUBLICATIONS 745

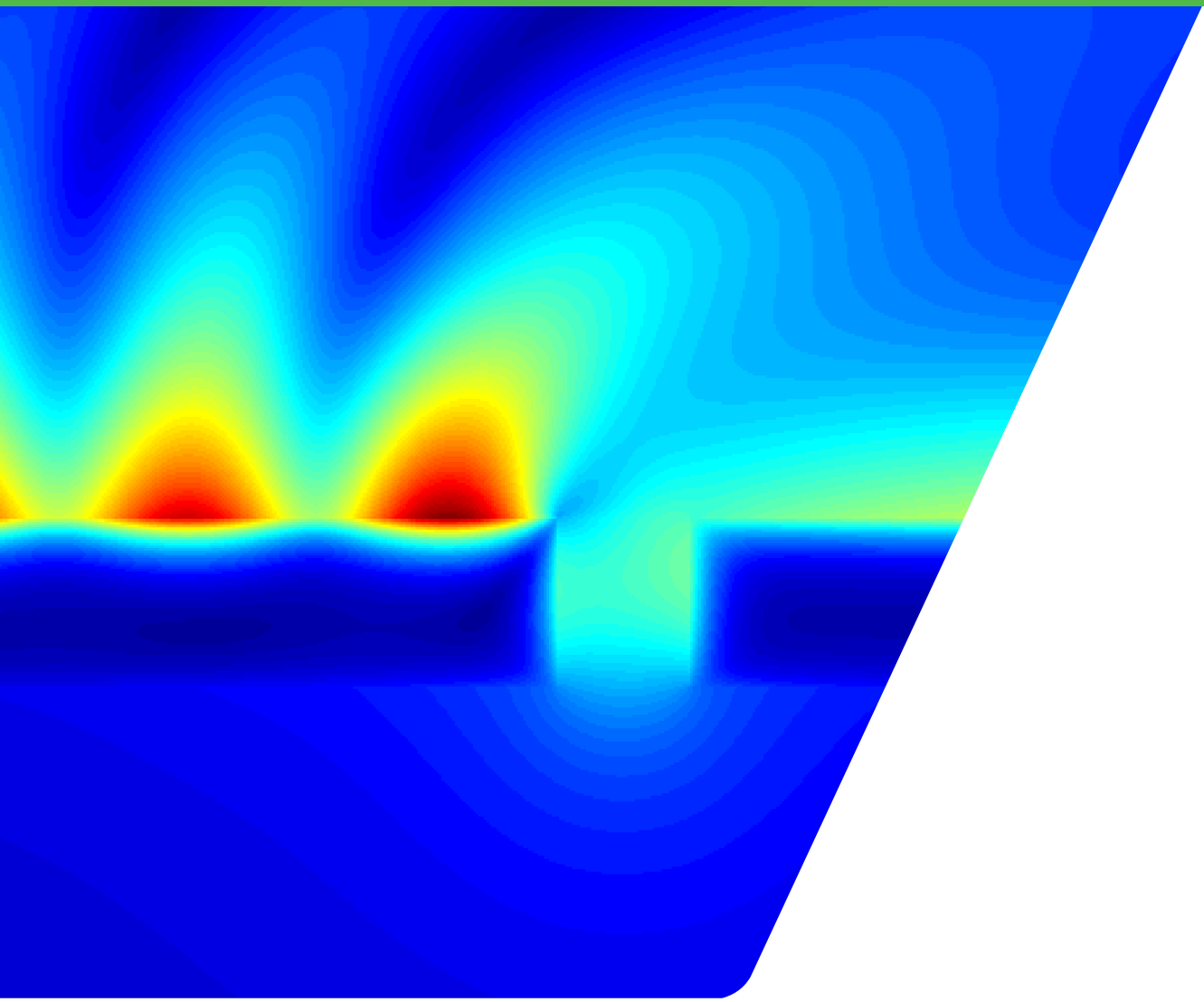

Juuso Olkkonen

Finite difference time domain studies on sub-wavelength aperture structures

VTT PUBLICATIONS 745

Finite difference time domain studies on sub-wavelength aperture structures

Juuso Olkkonen

Academic Dissertation to be presented with the assent of the Faculty of Science, University of Oulu, for public discussion in the Auditorium L10, on November 12th, 2010, at 12 o'clock noon.

ISBN 978-951-38-7410-0 (soft back ed.)
ISSN 1235-0621 (soft back ed.)

ISBN 978-951-38-7411-7 (URL: http://www.vtt.fi/publications/index.jsp)
ISSN 1455-0849 (URL: http://www.vtt.fi/publications/index.jsp)

JULKAISIJA – UTGIVARE – PUBLISHER

VTT, Vuorimiehentie 5, PL 1000, 02044 VTT
puh. vaihde 020 722 111, faksi 020 722 4374

VTT, Bergsmansvägen 5, PB 1000, 02044 VTT
tel. växel 020 722 111, fax 020 722 4374

VTT Technical Research Centre of Finland, Vuorimiehentie 5, P.O. Box 1000, FI-02044 VTT, Finland
phone internat. +358 20 722 111, fax + 358 20 722 4374

Edita Prima Oy, Helsinki 2010

Juuso Olkkonen. Finite difference time domain studies on sub-wavelength aperture structures [FDTD-tutkimuksia aallonpituutta pienemmistä apertuurirakenteista]. Espoo 2010. VTT Publications 745. 76 p. + app. 52 p.

Keywords finite difference time domain method, apertures in metal films, surface plasmon polaritons, data storage

Abstract

Modern optical technologies, such as microscopy, data storage, and lithography, require optical light spots with lateral dimensions that are much smaller than the wavelength of incident light. In free space, no such light spots are known to exist due to diffraction – a phenomenon exhibited by all electromagnetic waves. In this thesis, the formation of highly confined light spots by means of sub-wavelength aperture structures in metal films is studied via finite difference time domain (FDTD) simulations. It is observed that the otherwise weak light transmittance through sub-wavelength apertures can be remarkably enhanced by filling the aperture by a high refractive index material. The transmittance through the aperture can be further increased by introducing surface corrugations that couple the light impinging outside the aperture into surface waves propagating along the film plane. It is also demonstrated that significant transmission enhancement is obtained by inserting a semitransparent metal film in front of the aperture at the distance that fulfills the Fabry-Pérot resonance condition. The gap between the semitransparent metal film and the film containing the aperture works as a light trapping cavity, enhancing the amplitude of the illuminating monochromatic plane wave.

A simple scattered field technique that allows FDTD modeling scattering of obliquely incident plane waves from objects residing in a dispersive multilayer background structure is introduced in this work. The technique is applied to study how a surface plasmon polariton field that is excited in the traditional Otto configuration couples to a 100 nm wide slit in a metal film.

As an application example of the aperture structures, the effect of the embedded non-linear aperture layer in the traditional DVD disk on the data storage density is studied via the 3D FDTD method. It is found that the aperture layer enables distinguishing of data marks smaller than 100 nm in the far field, making it possible to increase the storage density of DVD disks by a factor of four.

Juuso Olkkonen. Finite difference time domain studies on sub-wavelength aperture structures [FDTD-tutkimuksia aallonpituutta pienemmistä apertuurirakenteista]. Espoo 2010. VTT Publications 745. 76 s. + liitt. 52 s.

Avainsanat finite difference time domain method, apertures in metal films, surface plasmon polaritons, data storage

Tiivistelmä

Modernit optiset teknologiat, kuten mikroskopia, tiedontallennus ja litografia, tarvitsevat optisia valopisteitä, joiden lateraalidimensiot ovat paljon pienempiä kuin valon aallonpituus. Vapaassa tilassa tällaisia valopisteitä ei tiedetä esiintyvän johtuen diffraktiosta – ilmiö, jota kaikki sähkömagneettiset aallot noudattavat. Työssä tutkitaan FDTD (Finite Difference Time Domain) -menetelmää käyttäen hyvin pienten valopisteiden muodostamista alle valon aallonpituuden kokoluokkaa olevilla apertuurirakenteilla metallikalvoissa. Työssä havaitaan, että apertuurien hyvin alhaista valonläpäisykykyä voidaan parantaa merkittävästi täyttämällä apertuuri korkean taitekertoimen materiaalilla. Valonläpäisyä voidaan lisäksi kasvattaa ympäröimällä apertuuri pintaurilla, jotka kytkevät apertuurin ympäristöön osuvan valon metallikalvon pintaa pitkin eteneviksi pinta-aalloiksi. Työssä myös demonstroidaan, että merkittävä läpäisykyvyn lisäys saavutetaan asettamalla puoliläpäisevä metallikalvo apertuurin eteen etäisyydelle, joka täyttää Fabry-Pérot-resonanssiehdon. Rako puoliläpäisevän ja apertuurin sisältävän metallikalvon välissä toimii valoloukkuna, joka kasvattaa valaisevan monokromaattisen tasoaallon amplitudia.

Työssä esitetään sirontakenttämenetelmä, jonka avulla voidaan FDTD-menetelmää käyttäen mallintaa, kuinka viistosti valaiseva tasoaalto siroaa dispersiivisessä monikerrosrakenteessa olevista sirottajista. Menetelmää käyttäen tutkitaan, kuinka perinteisessä Otto-konfiguraatiossa herätetty pintaplasmonaalto kytkeytyy 100 nm leveään rakoapertuurin metallikalvossa.

Apertuurirakenteiden sovellusesimerkkinä tutkitaan kolmiulotteisen FDTD-menetelmän avulla DVD-levyn sisässä olevan epälineaarisen apertuurikerroksen vaikutusta tiedontallennustiheyden kasvattamiseen. Havaitaan, että apertuurikerros mahdollistaa alle 100 nm:n kokoisten datamerkkien havaitsemisen kaukokentässä, mikä mahdollistaa DVD-levyjen tallennustiheyden kasvattamisen nelinkertaiseksi.

Preface

The work summarized in this thesis was carried out at the Optical Sciences Center, the University of Arizona, and at the VTT Technical Research Centre of Finland during 2002–2010.

I would like to thank Prof. Dennis Howe and Prof. Tom Milster for their fruitful discussions and support during my stays at the Optical Sciences Center between 2002 and 2005. I would like to express my gratitude to Prof. Harri Kopola, Prof. Arto Maaninen and Prof. Pentti Karioja for all their support and encouragement. I am also deeply grateful to my supervisor Docent Seppo Alanko for all his help, guidance and patience.

I wish to thank VTT, the Tauno Tönninki Foundation, the Finnish Foundation for Technology Promotion, the University of Oulu Scholarship Foundation, the Academy of Finland, and the department of Physical Sciences at the University of Oulu for funding my research.

Scientific work, as such, without the possibility of sharing ideas with colleagues would be absolutely boring. I would therefore like to thank Dr. Kari Kataja, Dr. Janne Aikio, Dr. Armis Zakharian, and Mr. Markus Tuomikoski for valuable discussions and support. My current colleagues, Henrik, Kaisa, Kimmo, Kristiina, Maria, Marja, Reetta, Salme, Teemu and Tomi, here in Micronova are also greatly acknowledged for being such good friends of mine, creating a relaxed working atmosphere, and providing help whenever needed.

Finally, I would like to express my deepest love and gratitude to my daughter Viivi for being the constant sunshine of my life.

List of original publications

This thesis is a review of the author's work on sub-wavelength aperture structures and the finite difference time domain method: it consists of an overview and the following selection of the author's publications in these fields:

I. Olkkonen, J., Kataja, K. and Howe, D. Light transmission through a high index dielectric-filled sub-wavelength hole in a metal film. Opt. Express 2005. Vol. 13, pp. 6980–6989.

II. Olkkonen, J., Kataja, K. and Howe, D. Light transmission through a high index dielectric hole in a metal film surrounded by surface corrugations. Opt. Express 2006. Vol. 14, pp. 11506–11511.

III. Olkkonen, J. Light trapping cavity enhanced light transmission through a single sub-wavelength aperture in a metal film. Opt. Express 2009. Vol. 17, pp. 23992–24001.

IV. Olkkonen, J. FDTD scattered field formulation for scatterers in stratified dispersive media. Opt. Express 2010. Vol. 18, pp. 4380–4389.

V. Kataja, K., Olkkonen, J., Aikio, J. and Howe, D. Readout modeling of super resolution disks. Jpn. J. Appl. Phys 2004. Vol. 43, pp. 4718–4723.

Throughout the overview, these papers will be referred to by their Roman numerals.

Author's contribution

The author had a key role in all aspects of the research work. He performed all the calculations and numerical implementations reported in Papers I–IV. The author programmed the parallel 3D FDTD code used in Paper V. The author wrote the first manuscripts for Papers I–II and actively participated in writing and interpreting the results of Paper V. Papers III and IV were prepared in full by the author.

Other subject-related publications to which the author has contributed:

- Kataja, K., Olkkonen, J., Aikio, J. and Howe, D. Numerical study of the AgOx super resolution structure. Jpn. J. Appl. Phys. 2004. Vol. 43, pp. 160–167.

- Suutala, A., Olkkonen, J., Cox, D. C., Lappalainen, J. and Jantunen, H. Inverted method for fabricating a nano-aperture device with subwavelength structures. J. Vac. Sci. Technol. B 2009. Vol. 27, pp. 2457–2461.

- Aalto, T. and Olkkonen, J. Optical modelling in MEMS. Chapter 13 in the Handbook of silicon based MEMS materials and technologies. Veikko Lindroos, Markku Tilli, Ari Lehto, and Teruaki Motooka (Eds.), William Andrew Publishing, 2010.

Contents

List of abbreviations

ADE	Auxiliary Differential Equation
BOR-FDTD	Body-of-Revolution Finite Difference Time Domain
CD	Compact Disc
DFT	Discrete Fourier Transform
DVD	Digital Versatile Disc
FDTD	Finite Difference Time Domain
HAMR	Heat Assisted Magnetic Recording
MPI	Message Passing Interface
NA	Numerical Aperture
PML	Perfectly Matched Layer
PEC	Perfect Electric Conductor
SF	Scattered Field
SIL	Solid Immersion Lens
SPP	Surface Plasmon Polariton

SR	Super Resolution
Super-RENS	Super Resolution Near Field Structure
TFSF	Total Field Scattered Field
TE	Transverse Electric
TM	Transverse Magnetic
UPML	Uniaxial Perfectly Matched Layer

1. Introduction

Sub-wavelength optics is an optical discipline dealing with optical structures and light fields, the physical dimensions of which are, at least along one dimension, much smaller than the wavelength of incident light. It explores structures and devices such as sub-wavelength interferometers, apertures, beam splitters and optical circuits that can perform guiding, branching, and bending of light waves in the sub-wavelength domain [1–7]. Due to diffraction, which is a natural phenomenon exhibited by optical waves, freely propagating optical beams with sub-wavelength diameter are not known to exist [8]; only light that is guided by abrupt boundaries between material media can reside in the sub-wavelength domain. Such light guidance can be accomplished with, for example, metallic surfaces and waveguides that support propagation of surface plasmon polaritons (SPPs) [5, 6]. SPPs are electromagnetic surface modes that arise from the interaction between light and conduction electrons in metals [9]. Via coupling to electrons, light can squeeze into structures much smaller than the diffraction limit.

After the discovery of the near-field optical microscope in 1984 [10], sub-wavelength optics or, more generally, nano-optics has been a subject of vivid research. The next burst occurred in 1998 when Ebbesen *et al.* [11] discovered extraordinary light transmission through an array of sub-wavelength holes. This resulted in rapid development of the field and a deeper understanding of light interaction with sub-wavelength structures in metal films. The fast progress was promoted by the development of electromagnetic modeling tools, computer hardware and viable fabrication methods, including electron beam lithography [12], focused ion beam milling [13, 14] and nanoimprinting [15–17]. Collectively, these have opened up an exciting world of sub-wavelength optics.

The sub-wavelength aperture and groove structures in metal films allow for the construction of many traditional optical elements, such as lenses, filters, polarizers, and waveplates. For example, a focusing cylindrical lens can be

formed from an array of sub-wavelength slits with constant depth but varying widths [18] or constant width but varying depths [19]. Arrays of small sub-wavelength apertures can be engineered to function as optical color filters [7, 20, 21], surface plasmon sensors [22–24], and as substrates for enhanced fluorescence [25–28] and Raman spectroscopy [29–31]. As sub-wavelength slit apertures are extremely polarization sensitive, a simple polarizer can be realized from an array of slit apertures [16, 32–34]. A waveplate based on an array of nanometric slit grooves in a metal film has also been suggested [35].

Due to the high opacity of metals at optical frequencies, light is only transmitted through dielectric openings in the metal film, enabling spatial light confinement well beyond the fundamental diffraction limit. This property surely benefits many modern optical technologies, including near-field scanning optical microscopy [36–39], data storage [40–44, Paper V] and lithography [45]. The classical theory of Bethe [46], however, predicts that no significant amount of light is transmitted through apertures much smaller than the incident wavelength. This thesis demonstrates via finite difference time domain studies that a significant amount of incident light can indeed be transmitted through a sub-wavelength aperture by properly engineering the aperture structure. The two factors that affect aperture transmittance most are the aperture shape and the filling [Paper I]. The effects of surface grooves [Paper II] and a light trapping cavity [Paper III], and coupling of SPPs into a metallic slit [Paper IV] are also studied.

When a light field interacts with a sub-wavelength aperture in a metal film, strong evanescent waves as well as surface charges and currents are constituted into the aperture and its vicinity, strongly influencing the transmission properties of the aperture. Accurate modeling of the interaction requires all the field components to satisfy Maxwell's equations and appropriate boundary conditions. Thus, scalar diffraction theories are not adequate, and the modeling must resort to methods based directly on Maxwell's equations. In this thesis, the finite difference time domain (FDTD) method that discretizes Maxwell equations in both time and space is used as the main modeling tool. Calculation times are shortened using parallel computing. A scattered field technique enabling modeling of light interaction with dispersive scatterers in dispersive layered media is also introduced [Paper IV].

This thesis is organized as follows. The next section introduces the FDTD method in detail, including Yee's algorithm, dispersive media, absorbing and periodic boundary conditions, techniques to excite illuminating light fields, parallel implementation, and a body-of-revolution algorithm. Section 3 introduces

the transmission properties of various aperture structures in metal films and the factors with most influence on the transmission process. Possibilities of aperture structures in data storage are briefly illustrated in Section 4. Finally, the summary and conclusions are presented.

2. Finite difference time domain method

In 1966, Kane S. Yee introduced [47] the finite difference time domain (FDTD) method to solve the time-dependent Maxwell's equations in a spatially finite computation domain. The FDTD method approximates Maxwell's equations in the differential form by a central difference operator in both time and space. The electric and magnetic fields are then represented by their discrete values on the spatial grid, and are advanced in time. Yee's discrete representation of Maxwell's equations, with a properly sampled spatial grid, provides reliable numerical solutions for electromagnetic problems ranging from optical to radio frequencies.

This chapter addresses the essential parts of the FDTD method. It begins with a brief overview of Maxwell's equations and boundary conditions. Then three-dimensional Yee's algorithm is briefly introduced, followed by a dispersive material model and absorbing and periodic boundary conditions that are typically used to terminate the spatially finite FDTD lattice. Next, techniques to excite incident fields are addressed. Finally, the attention is turned to the body-of-revolution finite difference time domain (BOR-FDTD) method, which is the method of choice for cylindrically symmetric structures illuminated by normally incident plane waves or optical beams.

2.1 Maxwell's equations and boundary conditions

Classical macroscopic electromagnetic phenomena are governed by a set of vector equations known collectively as Maxwell's equations. Maxwell's equations in differential form are [48–51]:

$$\nabla \times \mathbf{E}(\mathbf{r},t) = -\frac{\partial}{\partial t}\mathbf{B}(\mathbf{r},t), \tag{1}$$

$$\nabla \times \mathbf{H}(\mathbf{r},t) = \frac{\partial}{\partial t}\mathbf{D}(\mathbf{r},t) + \mathbf{J}(\mathbf{r},t), \tag{2}$$

$$\nabla \cdot \mathbf{D}(\mathbf{r},t) = \rho(\mathbf{r},t), \tag{3}$$

$$\nabla \cdot \mathbf{B}(\mathbf{r},t) = 0, \tag{4}$$

where $\mathbf{E}$ is the electric field (V/m), $\mathbf{D}$ is the electric flux density (C/m^2), $\mathbf{B}$ is the magnetic flux density (Wb/m^2), $\mathbf{H}$ is the magnetic field (A/m), ρ is the electric charge density (C/m^3), $\mathbf{J}$ is the electric current density (A/m^2), $\mathbf{r}$ is the position vector, and t denotes the time. Equations (1)–(4) are known respectively as *Faraday's law*, *Ampere's law*, *Gauss' law*, and *magnetic Gauss' law*. The divergence free nature of the magnetic flux density means that the B-field lines cannot be interrupted. They can go round in loops or they can form unbroken infinite lines, but they cannot originate or terminate at specific points in space [52]. A similar argument applies to the D-field lines, except in locations where charges exist. When charges are present, lines of D originate on a positive charge and terminate on a negative charge; everywhere else the D-lines can twist and turn in space, but they cannot start or stop. A relationship between the charge density and the current density can be obtained by taking the divergence of (2) and introducing (3). It is found that

$$\nabla \cdot \mathbf{J}(\mathbf{r},t) + \frac{\partial}{\partial t}\rho(\mathbf{r},t) = 0. \tag{5}$$

This is the conservation law for the electric charge and current densities.

When an electromagnetic field is applied to a material medium, the phenomena of conduction, polarization, and magnetization may occur. The constitutive equations [53]

$$\mathbf{D}(\mathbf{r},t) = \varepsilon_0 \mathbf{E}(\mathbf{r},t) + \mathbf{P}(\mathbf{r},t), \tag{6}$$

$$\mathbf{B}(\mathbf{r},t) = \mu_0 \mathbf{H}(\mathbf{r},t) + \mu_0 \mathbf{M}(\mathbf{r},t), \tag{7}$$

provide relations between the four field vectors in a material medium, where $\mathbf{P}$ is the polarization density (C/m^2), $\mathbf{M}$ is the magnetization density (A/m), ε_0 is the permittivity of free space, and μ_0 is the permeability of free space. The polarization and magnetization densities are connected to electric and magnetic dipole moments, respectively, in a given medium. These dipole moments include

both induced effects and permanent dipole moments [53]. For a nondispersive, linear medium $\mathbf{P} = \varepsilon_0(\varepsilon_r - 1)\mathbf{E}$ and $\mathbf{M} = (\mu_r - 1)\mathbf{H} = \mathbf{0}$ and the constitutive equations simplify to the form

$$\mathbf{D}(\mathbf{r},t) = \varepsilon_0\varepsilon_r\mathbf{E}(\mathbf{r},t) = \varepsilon\mathbf{E}(\mathbf{r},t), \tag{8}$$

$$\mathbf{B}(\mathbf{r},t) = \mu_0\mu_r\mathbf{H}(\mathbf{r},t) = \mu\mathbf{H}(\mathbf{r},t), \tag{9}$$

where ε is the permittivity, μ is the permeability of the medium, and ε_r and μ_r are the relative permittivity and relative permeability, respectively. For a conductive medium, the electric current density is directly proportional to $\mathbf{E}$, that is

$$\mathbf{J}(\mathbf{r},t) = \sigma\mathbf{E}(\mathbf{r},t), \tag{10}$$

where σ is the conductivity of the material in siemens per meter. Under a time harmonic field, the conductivity of a medium is related to the complex refractive index (n_c) as $\sigma = \omega\varepsilon_0 \operatorname{Im}\{n_c^2\}$, where ω is the angular frequency.

Maxwell's equations (1)–(4) are applicable to inhomogeneous media, in which ε, μ, and σ vary from point to point in a continuous but otherwise arbitrary manner [54]. Knowledge of a variation in a field quantity across an abrupt boundary between two different media is often necessary to solve electromagnetic problems however. These boundary conditions are usually deduced from the integral form of Maxwell's equations (see, e.g., [49] or [50]), and can be given as

$$\hat{\mathbf{n}}_1 \times (\mathbf{E}_1 - \mathbf{E}_2) = \mathbf{0}, \tag{11}$$

$$\hat{\mathbf{n}}_1 \times (\mathbf{H}_1 - \mathbf{H}_2) = \mathbf{K}, \tag{12}$$

$$\hat{\mathbf{n}}_1 \cdot (\mathbf{D}_1 - \mathbf{D}_2) = \rho_s, \tag{13}$$

$$\hat{\mathbf{n}}_1 \cdot (\mathbf{B}_1 - \mathbf{B}_2) = 0, \tag{14}$$

where $\hat{\mathbf{n}}_1$ is a unit vector normal to the boundary between media 1 and 2, pointing from the boundary to the medium 1, and ρ_s is the surface charge density. $\mathbf{K}$ denotes the surface current density that is non-zero only on a surface of a perfect electric conductor (PEC). The field quantities denoted by the subscript 1 are infinitely close to the boundary in the medium 1, while the field quantities with the subscript 2 are infinitely close to the boundary on the opposite

side. Note that the D-vector was defined earlier as $\mathbf{D} = \varepsilon_r \varepsilon_0 \mathbf{E}$, where ε_r is the relative permittivity. If the D-vector is defined as $\mathbf{D} = \varepsilon_c \varepsilon_0 \mathbf{E}$, where ε_c is the complex relative permittivity that can be expressed for the time harmonic fields as $\varepsilon_c = \varepsilon_r + i\sigma/(\omega\varepsilon_0)$, then the normal component of the D-vector ($D_\perp$) is continuous across the boundary, i.e., $\hat{\mathbf{n}}_1 \cdot (\mathbf{D}_1 - \mathbf{D}_2) = 0$ [54]. The observed continuity of the $D_\perp$-field is due to the surface charges that generate a local D-field. The continuity equation of $\mathbf{D}$ also implies that the normal component of the E-field ($E_\perp$) must be discontinuous across the interface. From the physical standpoint, the $E_\perp$-field's discontinuity is due to interfacial charges that generate a local $E_\perp$ that has the same magnitude but opposite directions on the two sides of the interface [55].

2.2 Yee's algorithm

The spatial unit cell used in the three-dimensional FDTD method is shown in Figure 1, illustrating how the vector fields $\mathbf{E}$ and $\mathbf{H}$ are located with respect to the cell center. When multiple cells form an FDTD lattice, every component of the E-field is surrounded by four circulating components of the H-field, and vice versa. Such a staggered lattice is motivated by the integral form of Maxwell's curl equations. The contour integrals of $\mathbf{E}$ ($\mathbf{H}$) along the edges of the cell in Faraday's law (Ampere's law) circulate around the corresponding magnetic (electric) field component at the center of the cell face. For details, see e.g., Sect. 3.6.8 in Ref. [56].

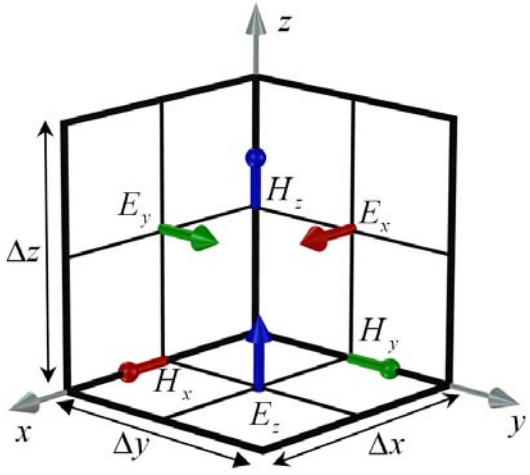

Figure 1. Locations of the electric and magnetic field components in a unit Yee cell with dimensions $\Delta x \times \Delta y \times \Delta z$.

A simple FDTD algorithm for non-dispersive, isotropic media can be constructed from Maxwell's curl equations (1) and (2) in conjunction with the constitutive equations (8)–(10). After substituting the constitutive equations, Maxwell's equations reduce to the form:

$$\frac{\partial}{\partial t}\mathbf{H}(\mathbf{r},t) = -\frac{1}{\mu(\mathbf{r})}\nabla\times\mathbf{E}(\mathbf{r},t), \tag{15}$$

$$\frac{\partial}{\partial t}\mathbf{E}(\mathbf{r},t) = \frac{1}{\varepsilon(\mathbf{r})}\left(\nabla\times\mathbf{H}(\mathbf{r},t) - \sigma(\mathbf{r})\mathbf{E}(\mathbf{r},t)\right), \tag{16}$$

which represent a system of six scalar equations. Following Yee's notation [47], a grid point in the uniform orthogonal mesh is defined as

$$(i, j, k) \equiv (i\Delta x, j\Delta y, k\Delta z), \tag{17}$$

and a scalar function of space and time as

$$F\big|^{n}_{i,j,k} \equiv F(i\Delta x, j\Delta y, k\Delta z, n\Delta t), \tag{18}$$

where Δx, Δy, and Δz are, respectively, the mesh space increments in the x, y, and z coordinate directions, respectively, Δt is the time increment, and i, j, k, and n are integers. Yee discretized the partial space and time derivatives of Eqs. (15) and (16) by the second-order accurate central finite differences. To illustrate this, let us consider the partial space derivative of F in the x-direction, as approximated by the central finite difference, at the fixed time $t = n\Delta t$:

$$\frac{\partial}{\partial x}F\big|^{n}_{i,j,k} = \frac{F\big|^{n}_{i+1/2,j,k} - F\big|^{n}_{i-1/2,j,k}}{\Delta x} + O(\Delta x^2), \tag{19}$$

where $O(\Delta x^2)$ is a remainder term that represents terms that are smaller than Δx^2. In a similar vein, the central finite difference approximation for the partial time derivative of F in a fixed point of space is written as:

$$\frac{\partial}{\partial t}F\big|^{n}_{i,j,k} = \frac{F\big|^{n+1/2}_{i,j,k} - F\big|^{n-1/2}_{i,j,k}}{\Delta t} + O(\Delta t^2). \tag{20}$$

After applying the central finite difference approximation to Maxwell's equations (15) and (16), the following time-domain update equations result for the H_x and E_x components:

$$H_x\Big|_{i+1/2,j,k}^{n+1/2} = H_x\Big|_{i+1/2,j,k}^{n-1/2} - \frac{\Delta t}{\mu_{i+1/2,j,k}} \left[\begin{array}{l} \dfrac{E_z\Big|_{i+1/2,j+1/2,k}^{n} - E_z\Big|_{i+1/2,j-1/2,k}^{n}}{\Delta y} - \\ \dfrac{E_y\Big|_{i+1/2,j,k+1/2}^{n} - E_y\Big|_{i+1/2,j,k-1/2}^{n}}{\Delta z} \end{array} \right], \tag{21}$$

$$E_x\Big|_{i,j+1/2,k+1/2}^{n+1} = \left(\frac{2\varepsilon_{i,j+1/2,k+1/2} - \sigma_{i,j+1/2,k+1/2}\Delta t}{2\varepsilon_{i,j+1/2,k+1/2} + \sigma_{i,j+1/2,k+1/2}\Delta t} \right) E_x\Big|_{i,j+1/2,k+1/2}^{n} + \left(\frac{2\Delta t}{2\varepsilon_{i,j+1/2,k+1/2} + \sigma_{i,j+1/2,k+1/2}\Delta t} \right) \left[\begin{array}{l} \dfrac{H_z\Big|_{i,j+1,k+1/2}^{n+1/2} - H_z\Big|_{i,j,k+1/2}^{n+1/2}}{\Delta y} - \\ \dfrac{H_y\Big|_{i,j+1/2,k+1}^{n+1/2} - H_y\Big|_{i,j+1/2,k}^{n+1/2}}{\Delta z} \end{array} \right]. \tag{22}$$

Note that in the derivation of Eq. (22), the $\sigma\mathbf{E}$ term appearing on the right-hand side of Eq. (16) is approximated in the time domain as

$$\sigma\mathbf{E}\Big|^{n+1/2} = \frac{1}{2}\sigma\left(\mathbf{E}\Big|^{n+1} + \mathbf{E}\Big|^{n} \right), \tag{23}$$

which is an arithmetic average of the stored value of $\mathbf{E}$ at time step n and to be computed value of $\mathbf{E}$ at time step $n+1$. For detailed derivations of Eqs. (21)–(22), see, e.g., Sect. 3.6.3 in Ref. [56].

Update equations (21) and (22), and the corresponding equations for the other electric and magnetic field components form the kernel of Yee's algorithm. An essential property of Yee's algorithm is that it introduces no dissipation into the physical problem due to numerical discretization, and hence energy is conserved [56]. It produces nonphysical numerical dispersion, however, which means that the phase velocity of the simulated wave can differ from the real speed of light varying with the wavelength, direction of propagation, and mesh discretization. It can be shown [56] that the numerical dispersion error diminishes with cell size h as $O(h^2)$, and therefore, it can be reduced to an acceptable level by using a FDTD lattice with about 30 points per the shortest wavelength of interest.

Since Yee's algorithm is developed in the time domain, it can propagate pulsed as well as time harmonic electromagnetic fields. Due to the time-marching nature of Yee's algorithm, electromagnetic waves physically propagate through the FDTD lattice in time steps of Δt. In practice, this means that solutions to resonance problems, in which light experiences multiple reflections and propagates several times through the resonance structure, require a significantly larger number of time-domain iterations than solutions to non-resonance problems.

The numerical stability of Yee's algorithm is determined by the cell size $(\Delta x, \Delta y, \Delta z)$ and the time step (Δt). In Yee's original work [47], the stability criterion was given incorrectly, and it was later corrected by Taflove *et al.* [57] to the form:

$$\Delta t < \frac{1}{c\sqrt{\frac{1}{(\Delta x)^2}+\frac{1}{(\Delta y)^2}+\frac{1}{(\Delta z)^2}}}, \tag{24}$$

where c is the maximum velocity of light in the FDTD lattice. The stability criterion (24) is generally accepted [56, 58–60] and successfully applied in many implementations of Yee's algorithm. In this thesis, the time step was calculated as

$$\Delta t = \frac{q}{c}\Delta \min, \tag{25}$$

where $\Delta \min$ is the smallest Yee cell dimension in the FDTD lattice and q = 0.5 (q = 0.7) in three (two) -dimensional simulations, respectively.

2.3 Dispersive media

The basic Yee's algorithm was introduced for non-dispersive media. To enable modeling of dispersive media with FDTD, Eq. (2) must be considered. Assuming that the complex permittivity of a dispersive medium in the frequency domain is $\varepsilon(\omega)$, where ω is the angular frequency, Ampere's law in the time domain can be rewritten as

$$\nabla \times \mathbf{H}(\mathbf{r},t) = F^{-1}\left\{ j\omega\varepsilon(\omega)\mathbf{E}(\mathbf{r},\omega)\right\}. \tag{26}$$

Here, the conductivity of the medium is included into the complex permittivity and $F^{-1}\{\}$ is the inverse Fourier transform operator. If $\varepsilon(\omega)$ is a Fourier transformable function, the right-hand side of Eq. (26) is typically implemented via the auxiliary differential equation (ADE) [61] or the recursive convolution

[62]. In this thesis, all dispersive media were modeled as single pole Lorentz media using the ADE approach. The single pole Lorentz medium exhibits the relative permittivity of the form [61]

$$\varepsilon_r(\omega) = \varepsilon_\infty + \frac{(\varepsilon_s - \varepsilon_\infty)\omega_0^2}{\omega_0^2 + 2j\omega\delta_0 - \omega^2}, \tag{27}$$

where ε_s is the static permittivity, ε_∞ is the permittivity at infinite frequencies, δ_0 is the damping factor, and ω_0 is the pole location. Now, for a single pole Lorentz medium, Eq. (26) can be written as

$$\begin{aligned} \nabla \times \mathbf{H}(\mathbf{r},t) &= \varepsilon_0\varepsilon_\infty \mathbf{E}(\mathbf{r},t) + \varepsilon_0 F^{-1}\left\{ j\omega \frac{(\varepsilon_s - \varepsilon_\infty)\omega_0^2}{\omega_0^2 + 2j\omega\delta_0 - \omega^2}\mathbf{E}(\mathbf{r},\omega)\right\}, \\ &= \varepsilon_0\varepsilon_\infty \mathbf{E}(\mathbf{r},t) + \mathbf{J}_0(t) \end{aligned} \tag{28}$$

where $\mathbf{J}_0(t)$ is the polarization current. Using the frequency domain expression of the polarization current, it is found that

$$\left(\omega_0^2 + 2j\omega\delta_0 - \omega^2\right)\mathbf{J}_0(\omega) = j\omega\varepsilon_0(\varepsilon_s - \varepsilon_\infty)\omega_0^2\mathbf{E}(\omega). \tag{29}$$

This equation can be transformed into the time domain via the inverse Fourier transform to obtain

$$\frac{d^2}{dt^2}\mathbf{J}_0(t) + 2\delta_0\frac{d}{dt}\mathbf{J}_0(t) + \omega_0^2\mathbf{J}_0(t) = \varepsilon_0(\varepsilon_s - \varepsilon_\infty)\omega_0^2\frac{d}{dt}\mathbf{E}(t). \tag{30}$$

This auxiliary differential equation provides a link between the time domain electric field and the polarization current. The details, how Eq. (31) is solved numerically as a part of Yee's algorithm, is presented in Ref. [61].

The refractive index of metallic materials at optical frequencies is typically such that the imaginary part is greater than the real part, and consequently the real part of the dielectric permittivity is negative. In Yee's algorithm, this means that the first multiplier term in the electric field update equation (see e.g. Eq. (22)) is greater than one, and thus the algorithm remains no stable. This problem can be circumvented by modeling metallic materials as dispersive media. As optical properties of metallic materials are mainly defined by the free electrons, the Lorentz medium is a fairly good model for metals. For example, Lorentz parameters ε_s = 4.7982x10^7, ε_∞ = 4.2167, δ_0 = 1.4046x10^{13} Hz, and ω_0 = 2.0254x10^{12} Hz, provide a good fit with the measured dielectric permittivity of silver given in Ref. [63].

When highly scattering (e.g. metallic) dispersive objects are modeled with FDTD, the material properties of the calculation lattice should be defined so that positions of the electric field components tangential to the scatterer surface define the scatterer boundaries [59]. If the boundary is defined by the normal electric field components, it typically leads to a slower convergence and unphysically high field amplitudes in the discrete points at the boundary. In addition, structures with sharp edges, especially in metallic structures, produce high local field enhancements. These field enhancements typically depend on the used cell size of the model, and thus when field enhancements are compared, the cell size should always be the same; otherwise the comparison is meaningless [64].

2.4 Boundary conditions

The FDTD method solves electromagnetic problems in a finite calculation lattice. Without any boundary conditions, Yee's algorithm assumes that the lattice is surrounded by a perfect electric conductor (PEC) layer. To obtain physically reasonable solutions in scattering problems, the calculation lattice must be truncated at the lattice edges via proper boundary conditions that extend the lattice to infinity, creating an illusion of an unbounded volume. Such a boundary condition could be obtained by a reflectionless absorbing layer that surrounds the lattice and absorbs all incident waves, regardless of the angle of incidence and wavelength. In practice, all numerically implemented absorbing layers are reflective, but one of the most efficient is the uniaxial perfectly matched layers (UPML) [65].

Perfectly matched layers (PML) were first introduced by J. P. Berenger [66]. Berenger's PML is typically referred to as a split field PML because the field components in PML regions are split into two unphysical field components to obtain additional degrees of freedom. This modification allows the creation of a reflectionless interface between a dielectric medium and the PML layer. UPML [65] is based on the artificial absorbing medium with a diagonal permittivity and permeability tensor. To illustrate the physical principles behind UPML, let us consider an interface at $z = 0$ between an ordinary dielectric medium and UPML. A plane wave is incident in a half space $z < 0$, with the relative permittivity ε_r and permeability μ_r. The dielectric permittivity and permeability tensors for UPML can be expressed in the frequency domain as

$$\bar{\bar{\varepsilon}} = \varepsilon_0 \varepsilon_r \begin{bmatrix} a & 0 & 0 \\ 0 & a & 0 \\ 0 & 0 & a^{-1} \end{bmatrix}, \quad \bar{\bar{\mu}} = \mu_0 \mu_r \begin{bmatrix} a & 0 & 0 \\ 0 & a & 0 \\ 0 & 0 & a^{-1} \end{bmatrix}, \tag{31}$$

It can be shown [65] that a reflectionless interface is obtained with any value of the constitutive parameter a. A typical choice is $a = 1 - j\sigma/(\omega\varepsilon_0)$. The conductivity ($\sigma$) is divided by the frequency to obtain frequency independent attenuation. When the incident plane wave enters the UPML layer through the interface at $z = 0$, its tangential wave vector components remain the same while the normal component is of the form: $k_z = ak_z^{\text{inc}}$. Thus, a plane wave propagating in the half space $z < 0$ transmits into the UPML medium by the relation

$$e^{-j\mathbf{k}^{\text{inc}}\cdot\mathbf{r}} \to e^{-j\mathbf{k}^{\text{inc}}\cdot\mathbf{r}} e^{-\alpha z}, \tag{32}$$

with $\alpha = -\text{Im}\{a\}k_z = \sigma\eta_0\sqrt{\varepsilon_r}\cos\theta$, for an incident angle θ. Here, η_0 denotes the free space wave impedance. As both the amplitude and phase are continuous across the boundary, there will be no reflection from this boundary for any incident angle or wavelength. The attenuation constant α depends on the incident angle θ, however, and thus plane waves close to glancing incidence may reflect back to the main calculation lattice via reflection from a PEC layer that terminates the finite thickness UPML layer. In practice, this is not a problem as the reflected wave is readily absorbed by the next absorbing layer perpendicular to the reflective UPML layer. So far, we have assumed that the wave incident into UPML is a real propagating plane wave. If the incident wave is evanescent, that is, k_z^{inc} contains an imaginary part, then absorption of evanescent waves can be enhanced by choosing $a = \kappa - j\sigma/(\omega\varepsilon)$ [65]. Here, we have assumed that a dielectric medium is terminated by a UPML layer. For lossy and dispersive media, UPML formulations can be found from Ref. [67].

The UPML medium characterized by the tensors (31) was presented via the frequency domain Maxwell equations. As FDTD models wave propagation in the time domain, the utilization of UPML in FDTD requires frequency domain equations to be transformed into the time domain. It proves [56] that UPML can be implemented efficiently using the auxiliary differential equation approach in a similar manner to that in which dispersive media are treated in Sect. 2.3. Theoretically, PML is reflectionless, but due to the finite thickness of a PML layer, the PML layer do reflect some of the incident EM waves back to the main lattice via a reflection from the perfect electric conductor layer terminating the calculation domain. If we denote the thickness of the PML layer by δ, the

reflectance of the PML layer is $R(\theta) = \exp[-2(\sigma\eta_0\sqrt{\varepsilon_r}\cos\theta)(2\delta)]$. Thus, the effective reflectance of the UPML layer is defined by the product $\sigma\delta$ [66]. This implies that extremely thin layers with high conductivity could be used as effective absorbers. Due to finite difference approximations of FDTD, however, sharp variations in reflectivity create reflections, and thus the conductivity of a PML layer has to be smoothly increased from zero to a maximum value with the distance from the dielectric/UPML interface. In this thesis, it was assumed that the conductivity exhibits a polynomial profile of

$$\sigma(s) = \left(\frac{s}{\delta}\right)^m \sigma_{\max}, \tag{33}$$

where s is the perpendicular distance from the interface between the main lattice and the UPML layer, m is the polynomial order and $\sigma_{\max}$ is the maximum conductivity.

Periodic structures consisting of an infinite number of unit cells placed sequentially in the directions of periodicity are modeled most efficiently by applying periodic boundary conditions at the edges of the unit cell. In non-periodic directions, the lattice is typically truncated by absorbing boundary conditions. If the structure of interest is periodic, for instance, in the x and y direction, each scalar field component U satisfies the Floque-Bloch theorem [68]:

$$U(x+d_x, y+d_y, z) = U(x,y,z)\exp\left[\, j(k_x^{\text{inc}} d_x + k_y^{\text{inc}} d_y)\,\right], \tag{34}$$

where d_x and d_y are dimensions of the unit cell, and k_x^{inc} and k_y^{inc} are wave vector components of the illuminating plane wave in the incident medium. The use of Eq. (34) as a periodic boundary condition in the basic Yee's algorithm requires field components to have complex values and all incident plane waves exhibit the same lateral wave vector components k_x^{inc} and k_y^{inc}. With oblique incidence, this typically means that the incident plane wave illumination can only contain a single wavelength. In the case of normal incidence, $k_x^{\text{inc}} = k_y^{\text{inc}} = 0$ and thus the incident time domain plane wave pulse can consist of a continuum of wavelengths enabling efficient modeling of frequency dependent responses of periodic structures.

2.5 Electromagnetic sources

As FDTD solves Maxwell's equations in the time domain, an electromagnetic scattering problem can be solved for multiple frequencies by a single simulation

using a time domain pulse. The time dependency of the incident field has to be such that it includes all the frequencies of interest. For example, the time domain electric field of a plane wave pulse in the spatial point $\mathbf{r} = \mathbf{0}$ can be expressed as $\mathbf{E_0} f(t)$, where $\mathbf{E}_0$ is a complex amplitude and $f(t)$ defines the time dependency. For an arbitrary point $\mathbf{r}$, the incident electric field is of the form:

$$\mathbf{E}_{\text{inc}}(\mathbf{r},t) = \mathbf{E}_0 \int_{-\infty}^{\infty} f(\omega) \exp[-j(\mathbf{k}(\omega)\cdot\mathbf{r} - \omega t)] d\omega, \tag{35}$$

where $\mathbf{k}(\omega)$ is the wave vector and $f(\omega)$ is the Fourier transform of $f(t)$. The incident field is typically introduced into the FDTD calculation lattice via the total field scattered field (TFSF) technique [56] or the scattered field (SF) technique [59]. Both techniques are based on the fact that due to the linearity of Maxwell's equations, the total field can be expressed as a sum of the incident field and the scattered field. In the absence of scatterers, only the incident field is present. The TFSF technique utilizes a virtual interface that divides the calculation lattice into a total field region and a scattered field region and guides the incident field through the calculation lattice. In the SF technique, Maxwell's equations are reformulated so that only the scattered fields are calculated by FDTD. The total field is obtained as a sum of the incident and the scattered fields. An essential difference between the techniques is that the TFSF technique requires knowledge of the incident electric and magnetic field components at the virtual interface, whereas the SF technique uses the incident electric field in the locations of scatterers.

In the case of a plane wave pulse propagating in a uniform medium, the incident field is not typically evaluated according to Eq. (35), since its direct numerical evaluation is rather time consuming, but instead a one-dimensional auxiliary FDTD simulation is used. The spatial point, at which the incident field is required to be known, is projected onto the one-dimensional grid of the auxiliary simulation. This approach is described in detail in Ref. [56]. When the propagation direction of a plane wave pulse coincides with one of the FDTD lattice axes, the TFSF technique provides a very simple and efficient way to plant the incident field into the FDTD lattice.

When the scatterers are located in a multilayer background structure, the TFSF technique with a one-dimensional auxiliary simulation can be used directly if the propagation vector of the incident plane wave pulse coincides with the stacking direction of the background structure. When the plane wave impinges with oblique incidence on the multilayer structure, the one-dimensional auxiliary

simulation is not sufficient. The incident field must be calculated analytically [69, 70] or via multiple auxiliary grids [71, 72]. When an analytical approach is used with the TFSF technique, it should be remembered that FDTD suffers from numerical dispersion, and to obtain a non-leaky virtual interface, the effects of numerical dispersion must therefore be taken into account [69].

Paper IV introduces a simple scattered field technique that enables FDTD modeling of obliquely incident light scattering from dispersive objects residing in a dispersive multilayer background structure. The technique is introduced in detail in Paper IV. The technique only calculates the scattered electric and magnetic field components in the FDTD lattice. The incident field is introduced to the scattered electric field components via the source term $\mathbf{S}(\mathbf{r},t)$ in the positions of scatters ($\mathbf{r}$). The source term can be expressed in a general form as:

$$\mathbf{S}(\mathbf{r},t) = F^{-1}\left\{ j\omega\left[\varepsilon(\mathbf{r},\omega) - \varepsilon_{\text{inc}}(\mathbf{r},\omega)\right]\mathbf{E}_{\text{inc}}(\mathbf{r},\omega)\right\}, \tag{36}$$

where $\varepsilon(\mathbf{r},\omega)$ and $\varepsilon_{\text{inc}}(\mathbf{r},\omega)$, respectively, are the complex dielectric permittivity of the scatterer and the incident background structure that would be present at point $\mathbf{r}$ in the absence of the scatterer. An advantage of this approach is that it is independent of the dispersion model used.

The techniques introduced so far for planting incident fields into the FDTD lattice are not limited to plane waves. Equally the incident beam can be, for instance, a focused Gaussian beam or a waveguide mode. For example, in Paper V, a focused, linearly polarized Gaussian beam was used to illuminate an optical disk structure. The field components of the focused monochromatic Gaussian beam were calculated from the integral presentation given in Ref. [73].

2.6 Calculation of phase and amplitude

If the incident field consists of multiple frequencies, the amplitude and phase of each monochromatic field solution must be calculated via the discrete Fourier transformation (DFT). An inherent assumption about DFT is that the transformable signal is periodic. Thus, when DFT is calculated for a data series consisting of N points sampled at time instants $t_k = k\Delta t$, $k = 0,...,N-1$, the transformation is obtained only for frequencies $f_i = i/(N\Delta t)$, $i = -(N-1)/2,...,0,...,(N-1)/2$. However, as the time dependency of the incident field is typically Gaussian, i.e., the field starts from a negligible small value, rises to the maximum, and then lands towards a zero on all points of the FDTD lattice, DFT can be performed at arbitrary frequencies smaller than $1/(2\Delta t)$. This corresponds to the case that N

approaches infinity via the adding of zeros to the transformable signal. DFT is typically run simultaneously with an FDTD simulation. The simulation is terminated when the field values of all the points of the FDTD lattice are negligible, i.e., smaller than the threshold value set by the user.

If the incident field is time harmonic, no Fourier transform is needed. Assume that an FDTD simulation, computing only the real part of the field components, reaches its steady state at the time step N. At this moment in time, an electric field component is of the form: $E_1(\mathbf{r}) = E_0(\mathbf{r})\sin\left[\omega N\Delta t + \phi(\mathbf{r})\right]$. After $\Delta N = (\pi/2)/(\Delta t\omega)$ time steps, the field component exhibits the form $E_2(\mathbf{r}) = E_0(\mathbf{r})\sin\left[\omega(N+\Delta N)\Delta t + \phi(\mathbf{r})\right] = E_0(\mathbf{r})\cos\left[\omega N\Delta t + \phi(\mathbf{r})\right]$. Now, $E_0(\mathbf{r}) = \sqrt{E_1(\mathbf{r})^2 + E_2(\mathbf{r})^2}$ and $\phi(\mathbf{r}) = \tan^{-1}(E_2(\mathbf{r})/E_1(\mathbf{r}))$. Note that this approach requires that Δt is adjusted so that ΔN is an integer.

2.7 Parallel implementation

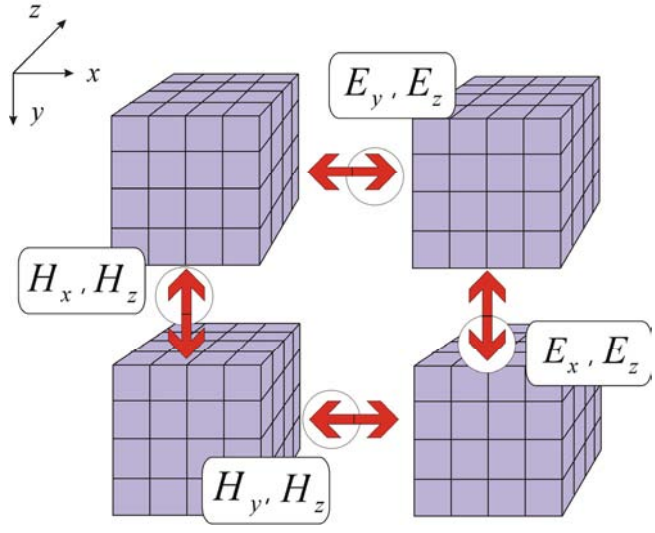

Figure 2. Illustration of a FDTD lattice decomposed in x and y directions. Each sublattice is processed by a separate process. Transverse field components in respect of the communication direction are exchanged between the sublattices so that the uppermost trasversal plane of the electric field components are send to the positive direction and the lowermost transversal plane of the magnetic field components are send to the negative direction.

A significant advantage of the FDTD method is that it is quite easy to implement in a parallel manner. Nowadays, each processor contains multiple cores, and

computer clusters are widely available. Thus, significant savings in calculation time can be achieved with codes dividing the workload into multiple processes. The Yee's algorithm is favorable for parallel computing, as the electric (magnetic) field component is only calculated from the nearest magnetic (electric) field components. Thus, when the FDTD lattice is divided into blocks to be processed by different processes, only the outermost electric and magnetic field components have to be exchanged between the adjacent processes at each iteration step. This is illustrated in Figure 2, in which the lattice is decomposed in the x and y directions. In addition, when DFT is calculated to obtain the amplitude and phase of each monochromatic field solution, no communication between the processes is required. In this thesis, the two- and three-dimensional FDTD codes used were implemented in a parallel manner using the message passing interface (MPI) [74].

2.8 Body-of-revolution FDTD method

The applicability of Yee's algorithm for analysis of large, complicated three-dimensional scatterers is relatively limited in terms of computer storage and run-time. The available memory limits the maximum number of Yee cells residing in the computation domain, while the long computation time restricts the use of the FDTD method for what-if simulations. In many cases, however, the computation burden can be eased by utilizing the symmetry of the studied structure. For example, if a scatterer exhibits an azimuthal symmetry, the problem can be simplified into a two-dimensional problem by expressing the azimuthal dependency as a Fourier series. In fact, this is the underlying idea of the body-of-revolution finite difference time domain (BOR-FDTD) method [56, 75, 76] introduced next.

Our starting point for the derivation of the BOR-FDTD method is Maxwell's equations in the differential form as given by (15) and (16), where $\mathbf{E} = \mathbf{E}(\rho, \phi, z, t)$ and $\mathbf{H} = \mathbf{H}(\rho, \phi, z, t)$ are now vectors in cylindrical coordinates (ρ, ϕ, z). As $\mathbf{E}$ and $\mathbf{H}$ are periodic in the azimuthal angle ϕ, these vectors can be represented as real-valued Fourier series:

$$\mathbf{E}(\rho, \phi, z) = \sum_{m=0}^{\infty} \mathbf{E}_m^{(e)}(\rho, z)\cos(m\phi) + \mathbf{E}_m^{(o)}(\rho, z)\sin(m\phi), \tag{37}$$

$$\mathbf{H}(\rho, \phi, z) = \sum_{m=0}^{\infty} \mathbf{H}_m^{(e)}(\rho, z)\cos(m\phi) + \mathbf{H}_m^{(o)}(\rho, z)\sin(m\phi), \tag{38}$$

where m is the index of the azimuthal harmonic. Substituting (37) and (38) in (15) and (16), where the curl operator is expressed in cylindrical coordinates, multiplying the resulting equations by $\cos(n\phi)$ or $\sin(n\phi)$, where n is an integer, and finally integrating over ϕ from $-\pi$ to π, due to the orthogonality of sine and cosine functions the following is obtained for [56]

$$\begin{bmatrix} 0 & -\partial_z & \pm\frac{m}{\rho} \\ \partial_z & 0 & -\partial_\rho \\ \mp\frac{m}{\rho} & \frac{1}{\rho}\partial\rho_\rho & 0 \end{bmatrix} \begin{bmatrix} E_{\rho,m} \\ E_{\varphi,m} \\ E_{z,m} \end{bmatrix} = -\mu \begin{bmatrix} \partial_t H_{\rho,m} \\ \partial_t H_{\varphi,m} \\ \partial_t H_{z,m} \end{bmatrix}, \tag{39}$$

$$\begin{bmatrix} 0 & -\partial_z & \mp\frac{m}{\rho} \\ \partial_z & 0 & -\partial_\rho \\ \pm\frac{m}{\rho} & \frac{1}{\rho}\partial\rho_\rho & 0 \end{bmatrix} \begin{bmatrix} H_{\rho,m} \\ H_{\varphi,m} \\ H_{z,m} \end{bmatrix} = \varepsilon \begin{bmatrix} \partial_t E_{\rho,m} \\ \partial_t E_{\varphi,m} \\ \partial_t E_{z,m} \end{bmatrix} + \sigma \begin{bmatrix} E_{\rho,m} \\ E_{\varphi,m} \\ E_{z,m} \end{bmatrix}, \tag{40}$$

where the upper and lower signs correspond to the upper and lower terms inside the brackets of the following expressions:

$$\begin{aligned} E_{\rho,m} &= \begin{pmatrix} E^{(o)}_{\rho,m} \\ E^{(e)}_{\rho,m} \end{pmatrix}, \qquad H_{\rho,m} = \begin{pmatrix} H^{(e)}_{\rho,m} \\ H^{(o)}_{\rho,m} \end{pmatrix}, \\ E_{\phi,m} &= \begin{pmatrix} E^{(e)}_{\phi,m} \\ E^{(o)}_{\phi,m} \end{pmatrix}, \qquad H_{\phi,m} = \begin{pmatrix} H^{(o)}_{\phi,m} \\ H^{(e)}_{\phi,m} \end{pmatrix}, \\ E_{z,m} &= \begin{pmatrix} E^{(o)}_{z,m} \\ E^{(e)}_{z,m} \end{pmatrix}, \qquad H_{z,m} = \begin{pmatrix} H^{(e)}_{z,m} \\ H^{(o)}_{z,m} \end{pmatrix}. \end{aligned} \tag{41}$$

Here, the ρ, z, and t dependences are not shown for simplicity. The upper and lower components are independent as long as the medium causes no coupling between them [56]. This is always the case with isotropic media, whereas the independency may be lost with anisotropic materials. Without loss of generality, the upper terms in Eq. (41) will be used in deriving the difference equations. The superscripts of even and odd modes and the mode number m will be omitted for simplicity.

Update equations of the BOR-FDTD method are obtained by expressing Eqs. (39) and (40) via central finite differences in a two-dimensional mesh comprised of lattice cells shown in Figure 3. For example, the update equations of H_ρ,

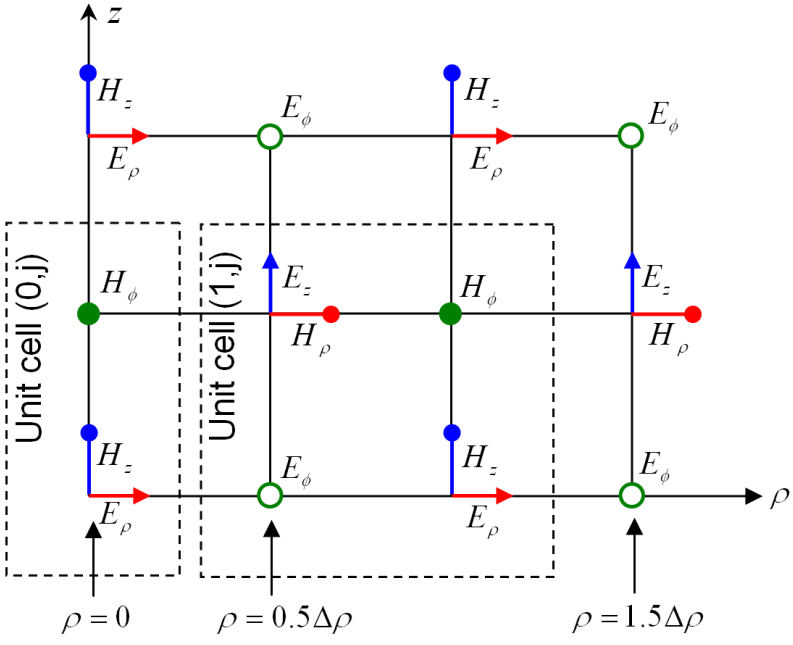

Figure 3. BOR-FDTD lattice.

E_ϕ, and E_z can be written as

$$H_\rho^{n+1/2}(i,j) = H_\rho^{n-1/2}(i,j) - \frac{\Delta t}{\mu}\left[\frac{m}{\rho(i)}E_z^n(i,j) - \frac{E_\phi^n(i,j+1) - E_\phi^n(i,j)}{\Delta z}\right], \tag{42}$$

$$E_\phi^{n+1}(i,j) = \frac{2\varepsilon - \sigma\Delta t}{2\varepsilon + \sigma\Delta t}E_\phi^n(i,j) + \frac{2\Delta t}{2\varepsilon + \sigma\Delta t} \left[\frac{H_\rho^{n+1/2}(i,j) - H_\rho^{n+1/2}(i,j-1)}{\Delta z} - \frac{H_z^{n+1/2}(i,j) - H_z^{n+1/2}(i-1,j)}{\Delta\rho}\right], \tag{43}$$

$$E_z^{n+1}(i,j) = \frac{2\varepsilon - \sigma\Delta t}{2\varepsilon + \sigma\Delta t}E_z^n(i,j) + \frac{2\Delta t}{2\varepsilon + \sigma\Delta t} \left[\frac{1}{\rho(i)}\frac{\rho(i+1/2)H_\phi^{n+1/2}(i,j) - \rho(i-1/2)H_\phi^{n+1/2}(i-1,j)}{\Delta\rho} + \frac{m}{\rho(i)}H_\rho^{n+1/2}(i,j)\right], \tag{44}$$

where $\rho(i) = (i - 1/2)\Delta\rho$, $\rho(i + 1/2) = i\Delta\rho$, and (i, j) of a field component refers to the location of the field component in the (i, j) unit cell. Note that $E_\phi(1, j)$ and $E_z(1, j)$, respectively, depend on the $H_z(0, j)$ and $H_\phi(0, j)$ located on the z-axis. The on-axis components cannot be updated directly using the above equations. Hower, as $H_\phi(0, j)$ is multiplied by $\rho(1/2) = 0$ in the $E_z(1, j)$ update equation, the value of $H_\phi(0, j)$ is not explicitly needed. In addition, Eq. (40) shows that $H_z(0, j) = 0$ for all $m > 0$. Only $H_z(0, j)$ with $m = 0$ must be solved via Faraday's law, resulting in [56]

$$H_z^{n+1/2}(0, j) = H_z^{n-1/2}(0, j) - \frac{\mu}{\Delta t}\frac{4}{\Delta\rho}E_\phi^n(1, j) . \tag{45}$$

The update equations remains stable when $\Delta t \le \Delta / (qc)$, where c is the maximum speed of light in the lattice, Δ is the smallest space increment, and $q \approx m + 1$ for $m > 0$, and $q = \sqrt{2}$ for $m = 0$ [56].

Boundary conditions and electromagnetic sources are implemented in BOR-FDTD via the same principles as in conventional FDTD. Details on how UPML is implemented in BOR-FDTD can be found from Refs. [56, 77]. The incident field determines the mode numbers m that must be solved to obtain complete solution. For example, if the incident field is a linearly polarized plane wave or a Gaussian beam that propagates along the z axis, the complete solution is obtained with the mode $m = 1$.

3. Light interaction with sub-wavelength apertures

The diffraction of light by an aperture in an opaque film is a fundamental phenomenon in optics and has been the subject of many studies since the end of the 19th century [46, 78–87]. Apertures in the classical Kirchhoff and Rayleigh-Sommerfeld diffraction theories are treated simply: the incident wavefront impinging on the aperture entrance appears in the aperture exit as such, whereas light falling outside the aperture is completely blocked. This approach is fairly accurate as long as the aperture dimensions are large compared with the wavelength of incident light (λ). When the aperture diameter approaches λ, the diffraction of light waves becomes more dominant and the problem has to be solved rigorously, with all the field components satisfying Maxwell's equations. One of the first rigorous solutions for the transmittance of a sub-wavelength aperture in an infinitely thin, perfectly conducting screen was provided by Bethe [46] in 1944. It states that when the aperture radius (r) is much smaller than the wavelength and the aperture is illuminated by a normally incident plane wave, the normalized transmission efficiency (η) of the aperture can be expressed as

$$\eta = \frac{64}{27\pi^2}(kr)^4, \tag{46}$$

where k is the wavenumber of the incident light. The normalized transmission efficiency is obtained by dividing the power transmitted through the hole by the incident power impinging on the geometrical entrance of the aperture. It was later shown by Bouwkamp [88] that Bethe's expression for the transmittance is only correct in the far field. A more accurate expression for the transmittance was found to be

$$\eta = \frac{64}{27\pi^2}(kr)^4\left[1+\frac{22}{25}(kr)^2+\frac{7312}{18375}(kr)^4+...\right]. \quad (47)$$

Due to the strong assumptions of Bethe's and Bouwkamp's laws, they only superficially describe the transmission properties of sub-wavelength holes in real metal films with finite thickness and conductivity. Surface plasmon and Fabry-Pérot effects, for instance, are not present in infinitely thin perfectly conducting apertures [89]. Thus, an analysis of practical, physical realizations of small apertures requires rigorous electromagnetic modeling tools such as the FDTD method, the multiple multi-pole technique [89, 90], the finite element method [91–94], the volume integral method [95], or the Fourier modal method [96]. In this thesis, transmission properties of sub-wavelength apertures are studied via the FDTD method.

3.1 Surface plasmon polaritons

Many phenomena that occur in sub-wavelength aperture structures are connected to surface plasmon polaritons (SPPs), which are electromagnetic surface waves propagating along a planar dielectric/metal interface [5]. SPPs are constituted by the free electrons of a conductor oscillating collectively in resonance with a light wave [9]. Due to the resonant interaction with (induced) surface charges, these surface waves are trapped on the surface of the metal. The conditions for the formation of an SPP are: (1) the metal film must exhibit a dielectric constant with a negative real part at the frequency of the incident light (in order to satisfy the required continuity of the normal component of the electric displacement vector at the dielectric/metal boundary), and (2) the component of the wave vector of the incident light that is parallel to the dielectric/metal interface must be matched with the SPP wave vector (the phase matching condition required to conserve momentum). At optical frequencies, only metals, such as aluminum, silver and gold, can satisfy the first condition. In addition, as the boundary conditions of Maxwell's equations state that the induced surface charge density is proportional to the discontinuity of the electric field component normal to the interface, only transverse magnetic (TM) polarized light can excite SPPs. The electric field spans from positive surface charges and terminates on negative ones, as illustrated in Figure 4.

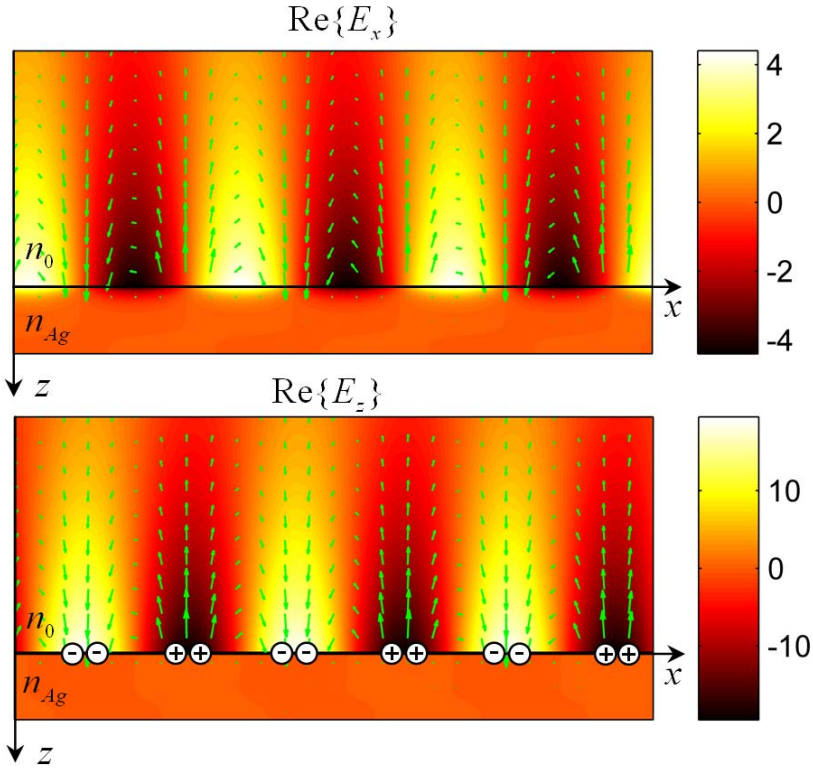

Figure 4. Electric field components of a monochromatic surface plasmon polariton field propagating along the x-axis at the interface between air and silver. Green arrows show the direction of the total electric field (E_x, E_z). The electric field starts from positive surface charges and terminates on negative ones. The surface charge density is proportional to the discontinuity of E_z at the interface.

Depending on the thickness of the metal film and the refractive indices of the adjacent media, only certain SPP modes can propagate on the dielectric/metal interface [97]. For example, a semi-infinite dielectric/metal-interface, in which both the metal and dielectric media are very thick, can only support a bound SPP mode whose field amplitude decays exponentially with distance on the both sides of the interface. The SPP propagation constant is then of the form [9]:

$$\beta_{SPP} = \sqrt{\frac{\varepsilon_m \varepsilon_d}{\varepsilon_m + \varepsilon_d}} k_0 , \tag{48}$$

where ε_m and ε_d are dielectric constants of the metal and the dielectric, respectively, and $k_0 = 2\pi / \lambda_0$ is the free space wavenumber. In optically thin

metal films there is a coupling between the SPPs associated with each dielectric/ metal-interface, i.e., the SPPs associated with the upper and lower surfaces of the thin metal layer. Four thickness-dependent SPP modes result [97]: these are the symmetric (*s*) and antisymmetric (*as*) modes, each of which branch into a pair of modes: one bound and the other leaky. The nature of these modes depends strongly on the thickness of the metal film as well as the refractive indices of the adjacent media. In the antisymmetric mode, the surface charges are in the same phase at the opposite sides of the metal film and thus the amplitude of the electric field component normal to the metal film exhibits a zero inside the film. In the symmetric mode, the surface charges are in the opposite phase at opposite sides of the film and, consequently, the electric field maintains its phase across the film. In the bound mode, the SPP field amplitude decays exponentially with distance on both sides of the thin film, while the leaky mode radiates some power into an adjacent dielectric medium. A thin film with the same dielectric materials on both sides (symmetric structure) can support only bound SPP modes [97].

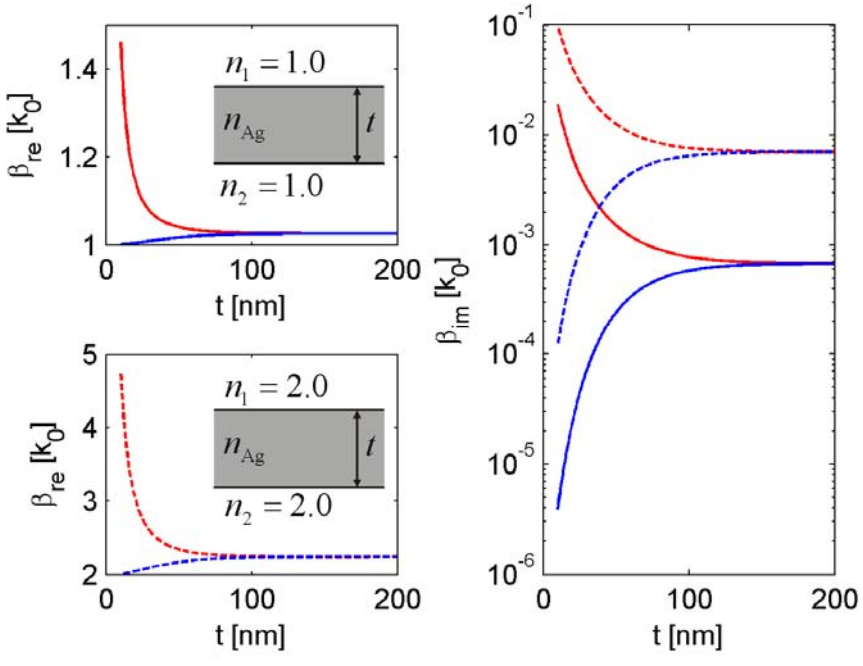

Figure 5. Complex propagation constant ($\beta = \beta_{re} + j\beta_{im}$) of anti-symmetric (red solid and dashed lines) and symmetric (blue solid and dashed lines) bound SPP modes as a function of the silver film thickness (t) for symmetric structures: $n_1 = n_2 = 1.0$ (solid lines) and $n_1 = n_2 = 2.0$ (dashed lines). $n_{Ag} = 0.054 + j4.41$, $k_0 = 2\pi / \lambda_0$, $\lambda_0 = 650$ nm.

The complex propagation constants ($\beta = \beta_{re} + j\beta_{im}$) of the symmetric and antisymmetric bound modes, as a function of the silver film thickness, are presented in Figure 5. The results were calculated according to Ref. [97]. Two cases are considered: the background medium is air or a dielectric medium with a refractive index of 2.0. When the film thickness increases, the solutions of symmetric and antisymmetric modes converge to the solution of Eq. (48). The antisymmetric mode is typically more confined to the interface than the symmetric mode but β_{im} is also higher. Figure 5 also illustrates that the higher the refractive index of the dielectric medium, the higher the attenuation losses.

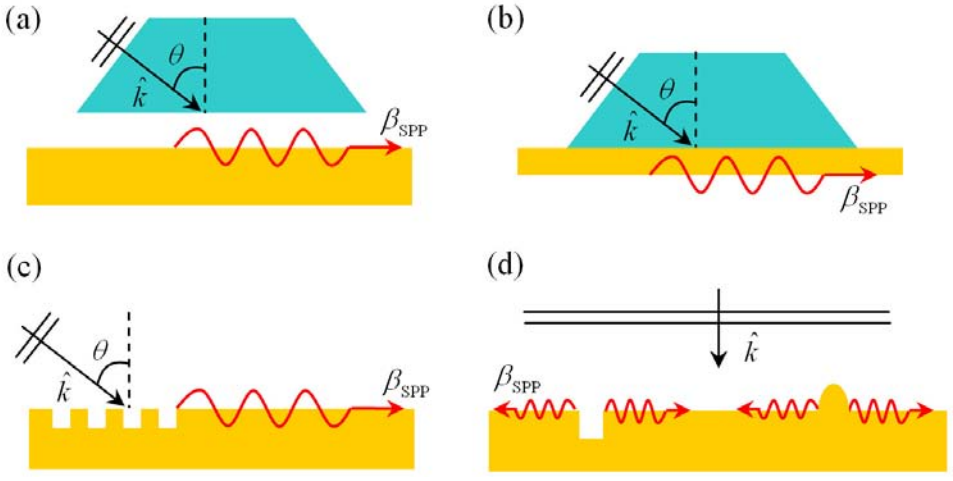

Figure 6. Four common SPP excitation geometries: (a) Otto configuration, (b) Kretschmann configuration, (c) grating diffraction, and (d) single sub-wavelength groove or a bump.

SPPs with frequency ω have greater momentum than light that propagates in the dielectric medium with the same frequency. Directly incident light impinging on a planar metal film therefore cannot excite any SPP modes. Traditionally, SPPs are excited with the Otto [98] or the Kretschmann [99] configuration in which the evanescent light, produced by the total internal reflection in a prism base, is coupled to a metal film. The Otto configuration has an air-gap between the prism and the metal layer, while the prism is in direct contact with the metal layer in the Kretschmann configuration, as illustrated in Figure 6(a) and (b). The Kretschmann configuration is only viable with thin metal films, as SPP is excited on the back side of the metal film. This only happens in relatively thin films (< ~60 nm at optical frequencies). Figure 6(c) and (d) show two alternative

methods for prism configurations. A grating in a metal film may provide the necessary momentum for excitation of SPPs via diffraction. A single defect such as a groove or a bump may also excite SPPs if the defect is of the sub-wavelength size [7]. The coupling efficiency is dependent on the particular profile of the defect.

3.2 Slit apertures

The light transmittance through sub-wavelength slits in metal films depends strongly on the polarization state of incident light. When the slit width is smaller than approximately half of the incident wavelength ($w < \lambda / 2$), the transmittance of TE-polarized light (electric field parallel to the slit's long axis) approaches to zero with the increasing film thickness, while under TM-polarized illumination, more optical power can transmit through the slit than directly impinges on the geometrical slit entrance [100–104, Paper III]. In the TM case, the incident light induces surface charges on the slit walls in such a way that surface charges are in opposite phases at opposite sides of the slit walls [102, 105]. The induced surface charges and currents carry an electric field spanning from a positive charge to a negative charge and thus enable efficient light transport through the slit.

An alternative way to understand the polarization sensitivity of sub-wavelength slits is to calculate the complex propagation constants ($\beta = \beta_{re} + j\beta_{im}$) of the slit waveguide modes via the standard waveguide theories [50, 106]. The dependency of β on the slit width (w) and the refractive index of the slit (n_0) are shown in Figure 7 for the TE_0 and TM_0 modes of a silver cladding waveguide at the free space wavelength of 650 nm. The pertinent waveguide geometry is depicted in the inset of Figure 7. It is seen that by increasing the slit refractive index, the cutoff slit width of the TE_0 mode can be significantly decreased. For example, when $n_0 = 1.0$, the effective cutoff width (w_c) is $0.43\lambda_0$, whereas with $n_0 = 3.8$, $w_c = 0.07\lambda_0$. The black line in the TE_0 graph shows β_{re} for an air-cladding waveguide with a core index of 3.8. When the slit width is larger than $0.4\lambda_0$, β_{re} of the silver- and air-cladding waveguide are almost identical, indicating that light is strongly confined to the core. In contrast to the TE_0 case, the TM_0 modes suffer from the increased refractive index of the slit. The TM_0 modes exhibit no clear cut-off width, but the mode attenuation strongly increases when the slit width approaches to zero.

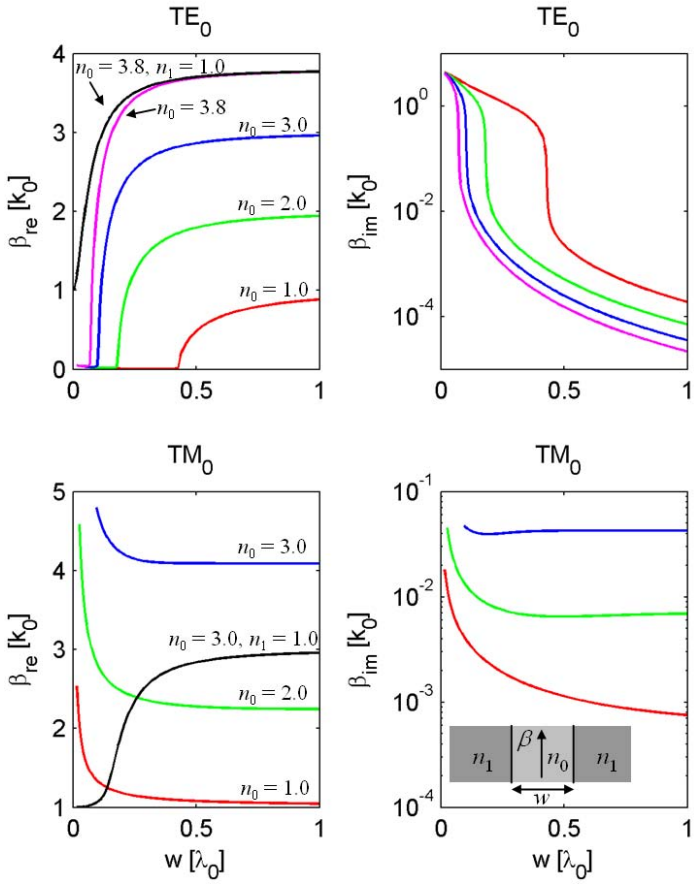

Figure 7. Complex propagation constants $\beta = \beta_{re} + j\beta_{im}$ of the TE_0 and TM_0 slab waveguide modes with silver cladding ($n_1 = n_{Ag}$) as a function of the core width (w) for various refractive indices of the core (n_0). The black lines show β for air cladding. λ_0 = 650 nm, $k_0 = 2\pi / \lambda_0$, $n_{Ag} = 0.054 + j4.41$.

The extraordinary transmission phenomenon, i.e., the slit transmits more optical power than directly impinges on its geometrical entrance, observed with slits under the TM-polarized plane wave illumination is widely explained as being due to Fabry-Pérot resonances occurring in the slit [100–102]. The sharpness of the slit edges seems to have a negligible effect on the transmittance [102]. The TM_0 mode propagating in the slit is guided through the slit via surface charges and currents, which experience the slit exit and entrance interfaces and produce a TM_0 field reflected back towards the opposite face of the slit. Thus, the field within the slit consists of two TM_0 fields propagating up- and downward along

the slit, the phase difference of which defines the emergency of transmission maxima and minima. The reflectivity of the slit end faces is also due to the large difference between the effective index of the waveguide mode and the refractive index of the surrounding medium. The effective index increases with the decreasing slit width, and thus Fabry-Pérot resonance peaks seen in the slit-length dependent transmission curves appear sharper with narrower slits [101].

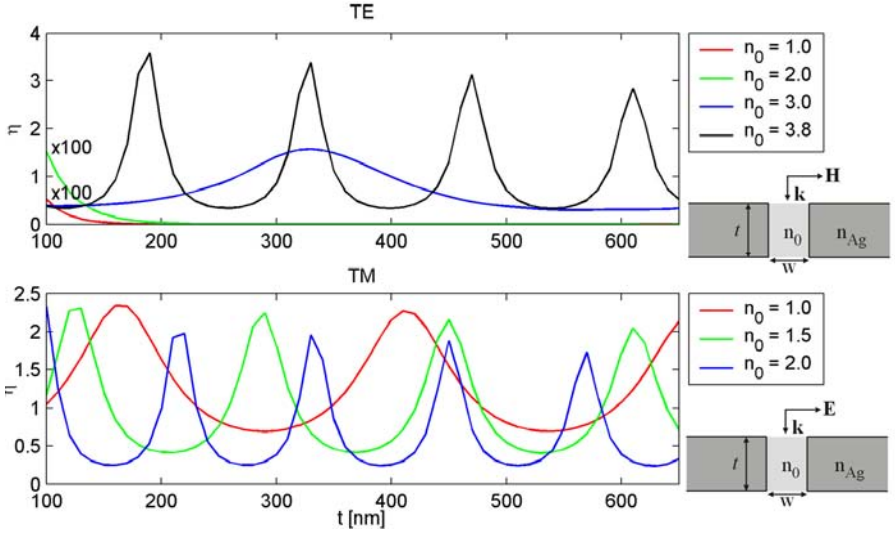

Figure 8. Normalized transmission efficiency (η) of TE- and TM-polarized normally incident plane waves (λ_0 = 650 nm) through a 70nm wide (w) slit in a free standing silver film with thickness t. The slit is filled with a dielectric medium with refractive index n_0. The red and green lines in the upper graph are multiplied by a factor of 100.

Fabry-Pérot resonance behaviour is also observed with sub-wavelength slits under TE-polarized illumination if the slit is filled by a high index dielectric medium [Paper III]. The refractive index difference between the slit and the surrounding medium creates the reflective interfaces required for a Fabry-Pérot cavity. Figure 8 shows transmission efficiencies of TE- and TM-polarized normally incident plane waves (λ_0 = 650 nm) through a 70 nm wide slit in a silver film, as calculated by the two-dimensional FDTD method. The dielectric filling of the slit greatly enhances the transmittance in the TE case, whereas no positive influence is observed in the TM case.

When two adjacent slits in a metal film are separated by the proper distance and illuminated by a TM-polarized plane wave, both of the slits transmit more optical power than a single slit alone [102, 107]. This is seen as being due to

surface waves, e.g., SPPs, excited by the slit entrances. The surface waves couple into adjacent slits and interfere with the waveguide mode coupled from the incident plane wave. As a function of the phase difference between the surface wave and the incident plane wave, which is controlled by the distance between the slits, the transmission is enhanced or suppressed through the slits. Due to the absence of surface charges, which are a necessity for surface waves on metal films, no similar effect is observed with TE-polarized illumination.

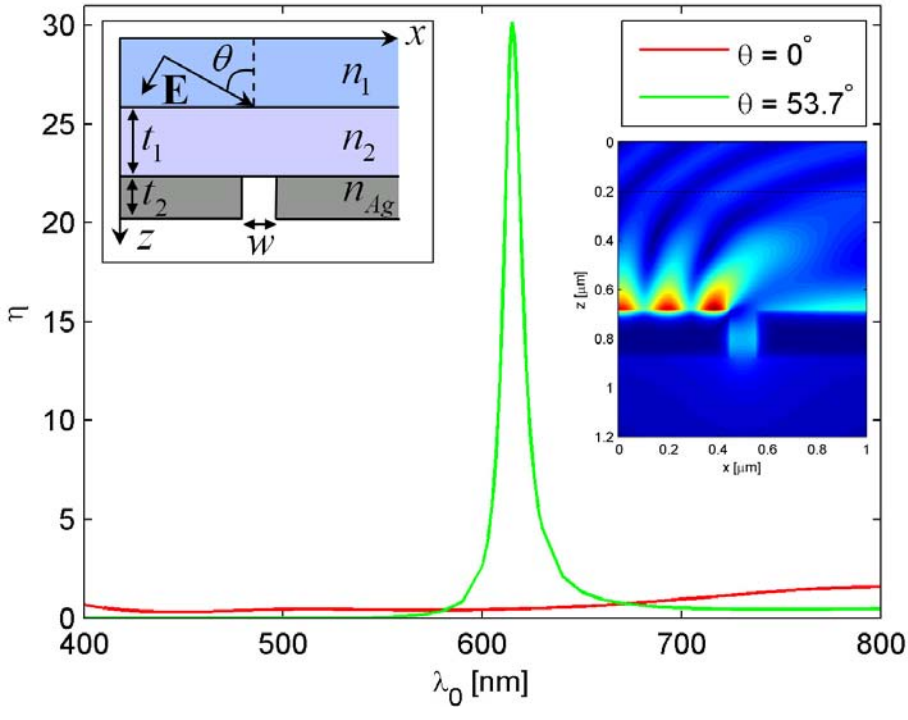

Figure 9. Normalized transmission efficiency of a TM-polarized plane wave through a slit structure shown in the inset (n_1 = 2.0, n_2 = 1.5, t_1 = 480 nm, t_2 = 200 nm, w = 100 nm) as a function of the free space wavelength λ_0. The plane wave is incident in the n_1-layer with an incidence angle of θ. The medium below silver film is air. When θ = 53.7 deg and λ_0 = 615 nm, light transmission through the slit is enhanced due to the excitation of SPPs. The inset shows the magnetic field amplitude in the structure when the SPP resonance is strongest. [Paper IV]

Paper [IV] studies how spectral transmittance of a 100 nm wide slit in a 200 nm thick silver film changes if the illuminating plane wave excites SPPs on the incident surface of the silver film. The excitation of SPPs is accomplished via

the modified Otto configuration, in which the air gap between the metal film and the prism is filled by a dielectric medium. The normalized transmittance through the slit as a function of the free space wavelength of the illuminating plane wave at normal incidence and the SPP resonance angle is shown in Figure 9. The normalized transmission efficiency was calculated with the both angles of incidence so that the transmitted power behind the slit was divided by the power that would impinge on the slit entrance at normal incidence in the absence of the gap between the prism and the metal film. Clearly, when the SPP resonance conditions are fulfilled, the incident light is collected transversally from a wider area as compared to the case of normal incidence, resulting in a significant transmission enhancement. The coupling of SPPs into the slit is far from optimal however. This is seen from the inset of Figure 9, in which the magnetic field component of the incident and reflected SPP fields interfere on the left side of the slit.

3.3 Circular apertures

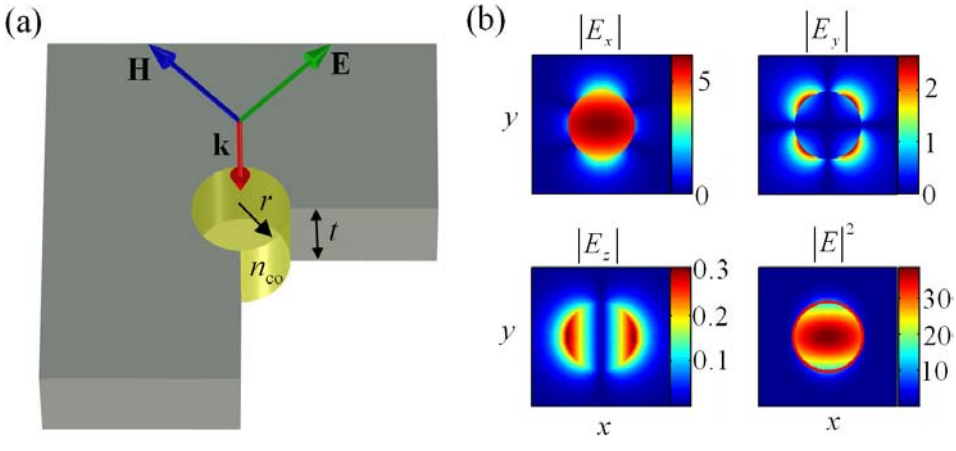

Figure 10. (a) Circular aperture with radius of r in a metal film with thickness t. The aperture is filled with a dielectric medium with a refractive index of n_{co}. (b) Amplitudes of electric field components (V/m) and intensity in the central xy-plane of the 100nm diameter aperture when $n_{co} = 2.4$ and t = 100 nm. The aperture is illuminated by a normally incident E_x polarized plane wave with a free space wavelength of 650 nm and amplitude of 1.0 V/m.

A distinct difference between circular apertures and slit structures in real metal films is that circular apertures do not support any propagating modes at optical

frequencies when the aperture diameter is smaller than 0.4λ [Paper I, Paper II], where λ is the wavelength of the illuminating light. An example of the circular aperture is shown in Figure 10. The propagation constant β for the waveguide mode (m,n) of a cylindrical waveguide with metallic cladding can be found by solving Maxwell's equations in cylindrical coordinates for the electric and magnetic field components of the form $\psi(\rho,\phi,z,t) = \psi_n(r)\exp[jm\phi]\exp[j(\omega t - \beta z)]$, where n and m are in integers, and $\beta = \beta_{\mathrm{re}} + j\beta_{\mathrm{im}}$. By matching the boundary conditions, it is obtained that β obeys the transcendental equation [106, 108–110]

$$\left[\frac{J_m'(u)}{uJ_m(u)} + \frac{K_m'(w)}{wK_m(w)}\right]\left[\frac{J_m'(u)}{uJ_m(u)} + \left(\frac{n_{\mathrm{cl}}}{n_{\mathrm{co}}}\right)^2 \frac{K_m'(w)}{wK_m(w)}\right] = m^2\left(\frac{1}{u^2} + \frac{1}{w^2}\right)\left[\frac{1}{u^2} + \left(\frac{n_{\mathrm{cl}}}{n_{\mathrm{co}}}\right)^2 \frac{1}{w^2}\right], \tag{49}$$

where n_{co} and n_{cl} are refractive indices of the core and cladding, respectively, $u = r\sqrt{k_0^2 n_{\mathrm{co}}^2 - \beta^2}$ and $w = r\sqrt{\beta^2 - k_0^2 n_{\mathrm{cl}}^2}$ are normalized transverse wave numbers, r is the radius of the waveguide core, $J_m(u)$ is the Bessel function of the first kind, and $K_m(u)$ is the modified Bessel function of the second kind. The prime denotes differentiation with respect to their argument. The values of β satisfying the transcendental equation were found numerically in the complex β domain using the argument principle of complex analysis [111] and a derivative-free multivariable minimum search algorithm [112].

The electric and magnetic field components of plane waves and focused Gaussian beams propagating along the z-axis in cylindrical coordinates exhibit $\exp[j\phi]$ dependency in the azimuthal angle ϕ. Thus, these electromagnetic fields, when impinging normally a cylindrical hole in a metal film, excite only waveguide modes that satisfy the transcendental equation (49) with $m = 1$. These modes are so-called hybrid modes with the nonzero longitudinal magnetic and electric field components, i.e., $E_z \neq 0$ and $H_z \neq 0$. Modes with relatively strong E_z are referred as EH_{1n} modes ($n = 1,2,3,\ldots$), and modes with relatively strong H_z as HE_{1n} modes. The modes of the metal-cladding waveguides found from the transcendental equation with $m = 1$ typically exhibit strong H_z and are thus referred to as HE_{1n} modes. In this thesis, the modes are labeled so that the mode index $n = 1$ refers to the mode with the smallest cut-off radius.

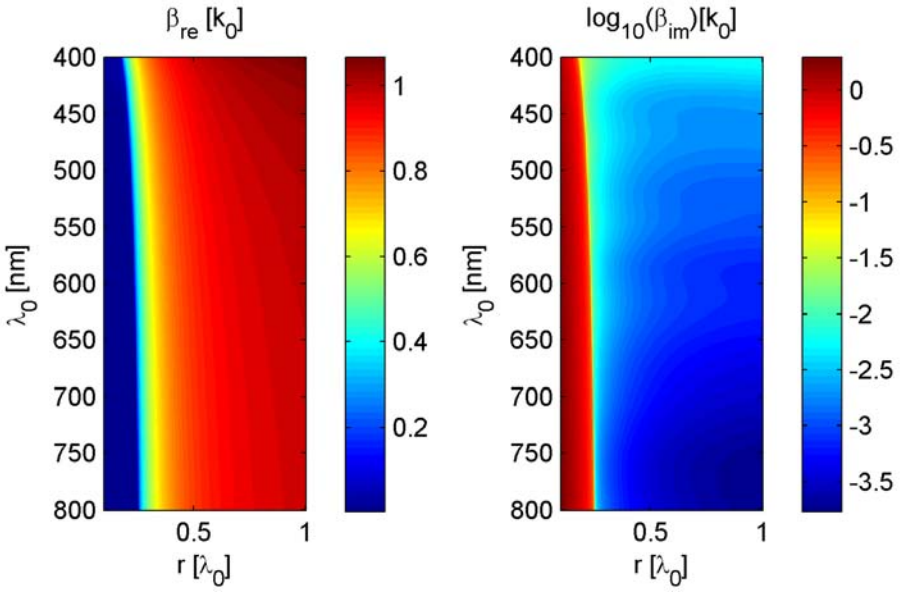

Figure 11. Complex propagation constant ($\beta = \beta_{\mathrm{re}} + j\beta_{\mathrm{im}}$) of the HE_{11} mode of a cylindrical waveguide with an air core and a silver cladding as function of the core radius (r) and the free space wavelength (λ_0). $k_0 = 2\pi / \lambda_0$.

The complex propagation constant of HE_{11} mode for a cylindrical waveguide with an air core and a silver cladding is shown in Figure 11 as a function of the core radius and the free space wavelength. The wavelength-normalized cut-off radius slightly increases with the increasing wavelength. For example, the cut-off radii at wavelengths 400, 600, and 800 nm are 0.18, 0.23 and $0.25\lambda_0$, respectively. This is due to the fact that $\mathrm{Im}\{n_{\mathrm{cl}} = n_{\mathrm{Ag}}\}$ is closer to the refractive index of the core ($n_{\mathrm{co}} = 1$) at the shorter wavelengths. Assuming that the metal cladding is completely lossless, i.e., $\mathrm{Re}\{n_{cl}\} = 0$, it can be shown [108, 110, 113] that there is always a propagation mode with $m = 1$ if $\mathrm{Im}\{n_{\mathrm{cl}}\} / n_{\mathrm{co}} \approx 1$, regardless of how small the core is. With real metals, such as silver, a similar kind of behavior is observed. Figure 12 shows β for the HE_{11} mode of a silver cladding waveguide as a function of the core refractive index at the free space wavelength of 488 nm. The core radii are 50, 25, 10, and 5 nm. When n_{co} is between 1 and 3.8, the studied core radii support no other modes than the HE_{11} mode. The refractive index of silver is assumed to be $0.05 + 3.02j$ [63]. The core refractive index that provides the smallest β_{im} clearly depends on the core radius, and when the hole radius decreases, the optimal n_{co} shifts towards $\mathrm{Im}\{n_{\mathrm{Ag}}\}$.

Due to the nonzero $\mathrm{Re}\{n_{Ag}\}$, β_{im} increases with the decreasing core radius. In addition, with the core radii of 5 and 10 nm, β approaches to $n_{\mathrm{Ag}}k_0$ when n_{co} is small enough. It should be noted that when the β_{re} is larger than $n_{\mathrm{co}}k_0$, the modes are so-called surface modes that have evanescent field amplitudes both in the core and the cladding [110].

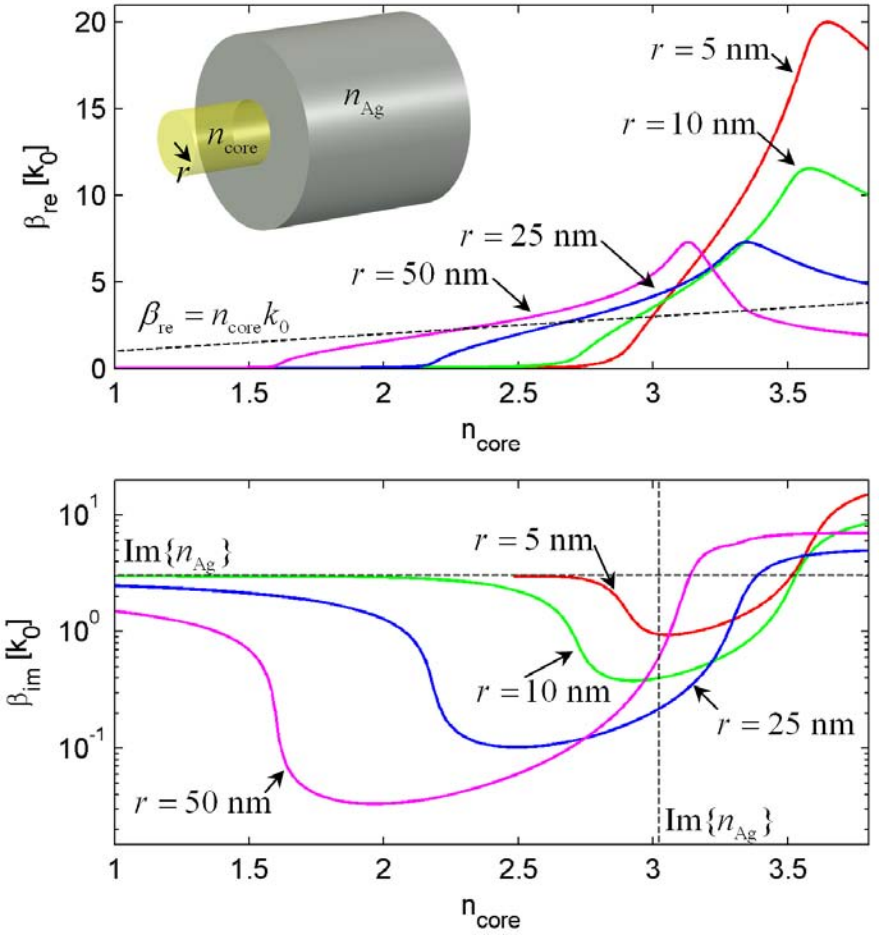

Figure 12. Complex propagation constant ($\beta = \beta_{\mathrm{re}} + j\beta_{\mathrm{im}}$) of the HE_{11} mode as a function of the core refractive index for a cylindrical waveguide with a silver cladding and the core radius (r) of 5, 10, 25, or 50 nm. The results are calculated at the free space wavelength (λ_0) of 488 nm. $k_0 = 2\pi / \lambda_0$, $n_{\mathrm{Ag}} = 0.05 + j3.02$.

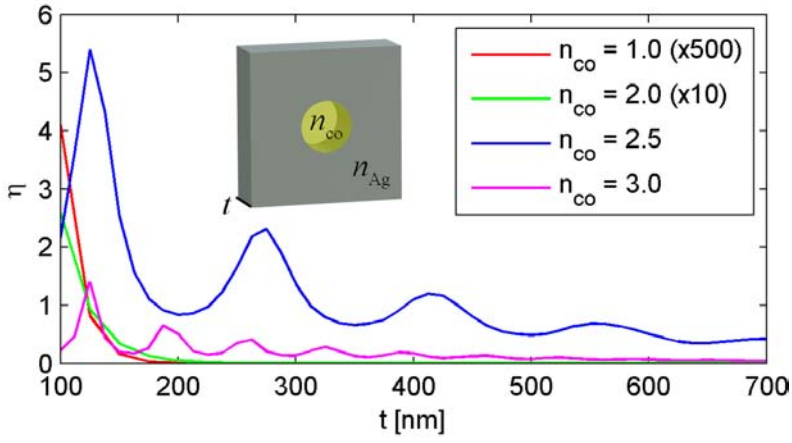

Figure 13. Normalized transmission efficiency (η) of a normally incident, linearly polarized plane wave (λ_0 = 488 nm) through a 50 nm diameter hole in a silver film with thickness t. The hole is filled with a dielectric medium with a refractive index of n_{co}. The red line is magnified by a factor of 500 and the green line by a factor of 10. The data were originally presented in Paper I.

As the high refractive index of the core enables the formation of a guided HE_{11} mode exhibiting a complex propagation constant, the imaginary part of which is relatively small, transmission properties of cylindrical holes in metal films can be changed drastically by filling the hole with a proper dielectric medium [Paper I, 108, 113]. This is illustrated in Figure 13, which shows the normalized transmission efficiency (η) of a normally incident, linearly polarized plane wave (λ_0 = 488 nm) through a 50 nm diameter hole in a silver film. When the hole is filled with a medium that has a refractive index of 2.5, it transmits over 500 times more power than the hole without the filling. If the media above and below the aperture exhibit the same refractive index as the dielectric filling, the transmission efficiency decreases significantly and the η versus thickness curve is also less modulated [Paper I]. This implies that the reflecting entrance and exit interfaces of the dielectric-filled hole form a Fabry-Pérot resonator, which additionally boosts light transmission through the hole. The fact that light propagates several round-trips in the resonator magnifies the importance of the small imaginary part of the propagation constant.

When a circular aperture is illuminated by a radially polarized beam, such as a Bessel beam, that is focused on the central point of the aperture, the incident field can excite the TM_{0n} mode ($n \geq 1$) mode of a cylindrical metallic

waveguide. The cut-off radii of TM_{0n} modes are significantly larger than the corresponding HE_{1n} modes [Paper I] however. The physical explanation for this is as follows: under a radially polarized illumination, the surface charges generated by the incident field are in the same phase over the entire contour of the aperture edge, whereas under linearly polarized illumination, the surface charges are in opposite phases, at opposite sides of the aperture, in the direction of the linearly polarized incident electric field. As the electric field can only span directly from a positive charge to a negative charge, it explains why the HE_{1n} modes exhibit smaller cut-off radii than the TM_{0n} modes.

3.4 C-apertures

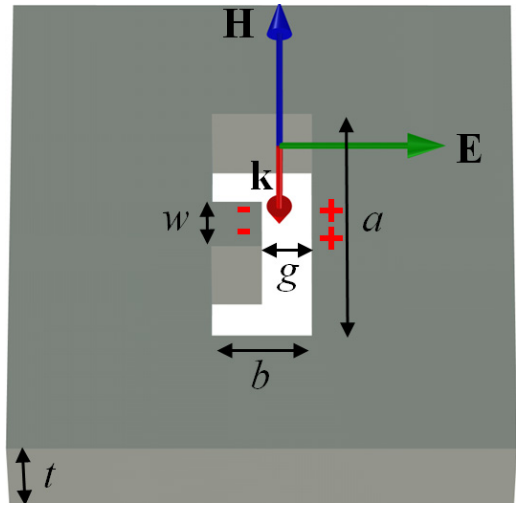

Figure 14. Illustration of a C-aperture in a metal film.

The aperture shape has a strong influence on its transmission properties. Sect. 3.2 demonstrated that unfilled slit structures are extremely polarization sensitive; only TM-polarized light (electric field parallel to the direction of the slit width) squeezes through a slit much narrower than the incident wavelength (λ). Circular apertures block light propagation simultaneously in all transversal directions and no light is transmitted through unfilled apertures with a diameter smaller than 0.4λ. In a C-aperture [114–119], the aperture shape is engineered so that a rectangular aperture exhibits a tongue in its central part. The tongue narrows the aperture locally, promoting good conditions for an electric dipole

created by the incident light polarized along the tongue axis. The electric dipole consists of induced surface charges that are in opposite phases at the opposite sides of the aperture [94], as illustrated in Figure 14. This dipole creates a local field that is confined to the gap between the tongue and the opposite side of the aperture. Typically, the total C-aperture length (a) can be smaller than the cut-off width of the corresponding rectangular aperture [64].

3.5 Cavity apertures

Paper III investigates a new kind of aperture structure that is formed from two parallel metal films separated by a small distance. The first metal film is semitransparent and the second opaque. A single sub-wavelength aperture, slit or cylindrical hole, is formed into the opaque metal film. The distance between the metal films is selected so that in the absence of the aperture all the incident monochromatic light is trapped into the space between the films. That is, the structure works as a light trapping cavity. Zero reflectance is obtained when the distance between the films is such that light interferes constructively in the gap. Due to the constructive interference, the amplitude of the incident light impinging on the opaque metal film is enhanced by a factor of 6.5 in the structure studied in Paper III. In practice, this means that in maximum the transmittance could be enhanced by a factor of $42.25\ (=6.5^2)$. An advantage of the cavity aperture structure is that it also enhances light transmission through the slit aperture under TE-polarized light, in contrary to the surface-wave-based mechanisms that require TM-polarized illumination.

When light transmission through an aperture in a metal film is considered, the aperture can be thought of as a scatterer residing in a background structure consisting of a metal film in a uniform medium. Assuming that the field present in the background structure is the incident field, the scattered field due to the aperture is obtained by subtracting the incident field from the total field present in the complete structure. If the metal film that contains an aperture is completely opaque, the scattered field behind the slit is the same as the total field. On the incident side of the aperture film, the scattered field emanates from the slit entrance back towards the light source. This scattered field has an

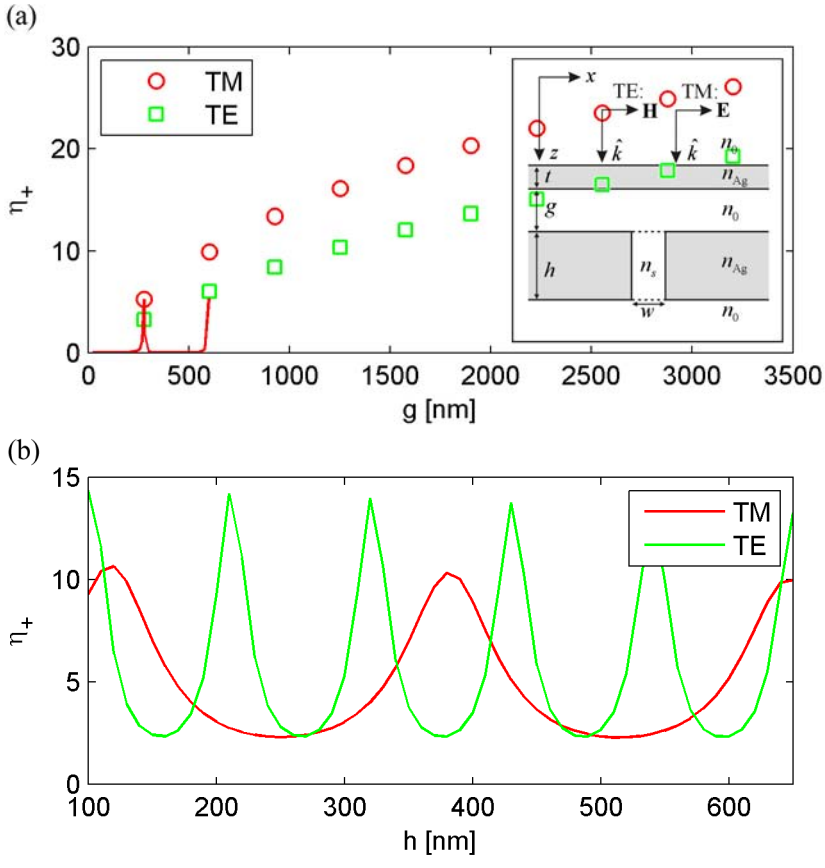

Figure 15. Normalized transmission efficiency of a normally incident plane wave through a 100 nm wide slit with a light trapping cavity as a function of the distance between the semitransparent metal film (t = 40 nm) and the opaque metal film (g = 277.5 nm + $m\lambda_0/2$, m = 0, 1, 2,…,9). TM-polarization: n_s = 1.0, h = 165 nm. TE-polarization: n_s = 3.8, h = 130 nm. Red solid line depicts the transmission efficiency in the TM case when g is varied from 10 to 600 nm in 10 nm steps. (b) Normalized transmission efficiency as a function of the opaque metal film thickness with a fixed gap thickness of 277.5 nm. Other parameters are the same as in (a). $n_0 = 1.0$ and λ_0 = 650 nm. [Paper III]

essential influence on the transmission properties of the cavity apertures. Paper III shows that a scattered field emanating from a slit towards the semitransparent metal film and then reflecting back to the slit will excite a waveguide mode that interferes destructively with the waveguide mode excited by the incident light, resulting in suboptimal transmission enhancement. The effect can be weakened by increasing the distance between the metal films in such a manner that the

Fabry-Pérot resonance condition remains valid. This way, the scattered field emanating from the slit spreads to a larger area and less optical power couples back to the slit. The effect is illustrated in Figure 15(a). A second alternative is to change the slit length, as it influences on both the phase and the amount of the scattered light. Paper III analyzed that the destructive interference occurs regardless of the slit length, and transmittance maximums are obtained with the slit lengths that minimize the amount of back-scattered light. Figure 15(b) shows how the transmission efficiency changes as a function of the thickness of the opaque metal film with a fixed cavity length.

With three-dimensional apertures, such as a cylindrical hole, the influence of the back-coupled scattered light is much weaker, as the optical power of the scattered light emanating from a cylindrical aperture spreads in inversely proportional way to the square of the distance ($1/d^2$). Paper III demonstrates an enhancement factor of 40 for light transmission through a cylindrical hole filled with a high index dielectric medium.

3.6 Corrugated apertures

Dimensions of sub-wavelength aperture entrances are typically smaller than the spot size of a focused beam. Some incident light thus always falls outside the entrance and is lost. Highly focused beams also require precise alignment with the aperture, which may be problematic in practical realizations. It would therefore be advantageous if less focused light could be used in the illumination via exploitation of light impinging outside the aperture.

Many theoretical [104, 120–124, Paper II] and experimental studies [125–128], have found that properly designed surface corrugations around the aperture entrance enhance light transmission under normally incident plane wave illumination. A generally accepted explanation at optical frequencies in real metal films is that the interaction of the incident light with grooves generates a bound SPP mode that propagates along the metal film and couples to the aperture as a waveguide mode. Depending on the phase difference between the waveguide modes excited by the normally incident light and SPP, the transmittance is either enhanced or suppressed. In addition to the SPP mode, the interaction with a groove generates a short-range field that couples to the aperture if the groove is within a distance of a few wavelengths from the aperture [122–124]. This kind of short-range field is essentially required for matching boundary conditions in the vicinity of the aperture [123].

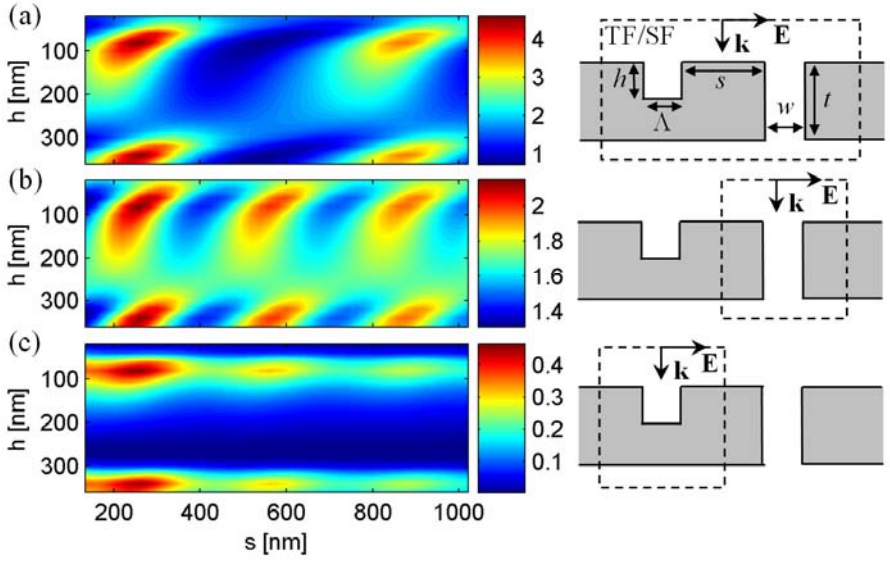

Figure 16. Normalized transmission efficiency (η) of a 100 nm wide slit flanked by a single groove parallel to the slit in a metal film as a function of s and h. In the absence of the groove, η = 1.7. (a) The entire structure is illuminated by a TM-polarized normally incident plane wave with a wavelength of 650 nm, whereas in (b) and (c), the plane wave impinges only on the slit or the groove. The plane wave was excited by the TFSF technique. Λ = 100 nm, t = 430 nm.

The simplest corrugated aperture structure is probably a single slit flanked by a single groove. Such a structure is illustrated in Figure 16. In this particular case, a 100 nm wide slit is located in a 430 nm thick free-standing silver film. A 100 nm wide groove with a depth of h is located at distance of s from the slit edge. The wavelength of the normally incident, TM-polarized plane wave is 650 nm. Using the TFSF technique in the 2D FDTD method, it is possible to illuminate the entire structure by a plane wave, or only the slit or the groove. This approach provides a better understanding of the factors influencing on transmittance. Figure 16(a) shows the normalized transmission efficiency (η) of the slit as a function of s and h when the entire structure is illuminated. Clearly, η varies periodically in both s and h. In the absence of the groove, η = 1.7. The periodicity in η with groove depth h is due to the interference of a down- and upward propagating TM_0 waveguide mode in the groove. The maximum in η appears at h = 80 nm and 342 nm. The transmission efficiency periodically depends on s due to the phase difference between the waveguide modes excited

into the slit by the incident plane wave and surface waves, including SPPs and short range-fields, generated by the groove. It can be seen that the first maximum along the s-axis is stronger than the second. This is due to the coupling of short-range fields generated by the groove entrance. The propagation constant of a bound SPP mode (β_{SPP}) on the silver/air interface is $(1.027 + j0.00068)\,k_0$. Due to the small imaginary part of β_{SPP}, the effect cannot be due to attenuation of SPPs. In Figure 16(b), only the slit is illuminated by a plane wave. Clearly, the slit entrance also excites surface waves that reflect from the groove back to the slit. Figure 16(c) shows η when the incident plane wave impinges only on the groove. The groove generates surface waves that partially couple into the slit and partially reflect from the slit back towards the groove, causing periodic variations into η as a function of s.

It is studied in Paper II how circular corrugations around a cylindrical hole affect its transmission properties. A 100 nm diameter hole in a silver film is filled by a dielectric medium with a refractive index of 2.8 to obtain a propagating HE_{11} mode that enables efficient light transmission through the aperture. First, a hole in 515 nm thick silver film is surrounded by a single circular 300 nm wide groove with a depth of h, as illustrated in Figure 17(a). Figure 17(b) shows the dependency of the hole's normalized transmission efficiency on the groove depth and the distance from the central hole (s_1). Compared with the case of a single slit flanked by a single groove (Figure 16), the results are surprisingly similar. The groove depth affects the strength of the surface waves generated by the groove due to Fabry-Pérot resonances, and the distance s_1 changes the phase of the mode excited into the aperture by the surface waves. The interference between the modes excited by the incident light and the surface waves defines the appearance of the transmission maxima and minima. In difference to the slit case, the second maxima, which appears at $s_1 \approx 900$ nm, is now stronger than the first at $s_1 \approx 200$ nm. This occurs as the length of the groove's circular contour, which excites surface waves, increases with s_1. Note that when the incident electric field is parallel to the groove's tangent, no surface waves in that region are excited. It is further examined in Paper II the influence of multiple grooves and found out that the optimal distance between the grooves is 300 nm. When the aperture is surrounded by 13 grooves, the normalized transmission efficiency attains a value of ~1000. More than 13 grooves provide no further transmission enhancement.

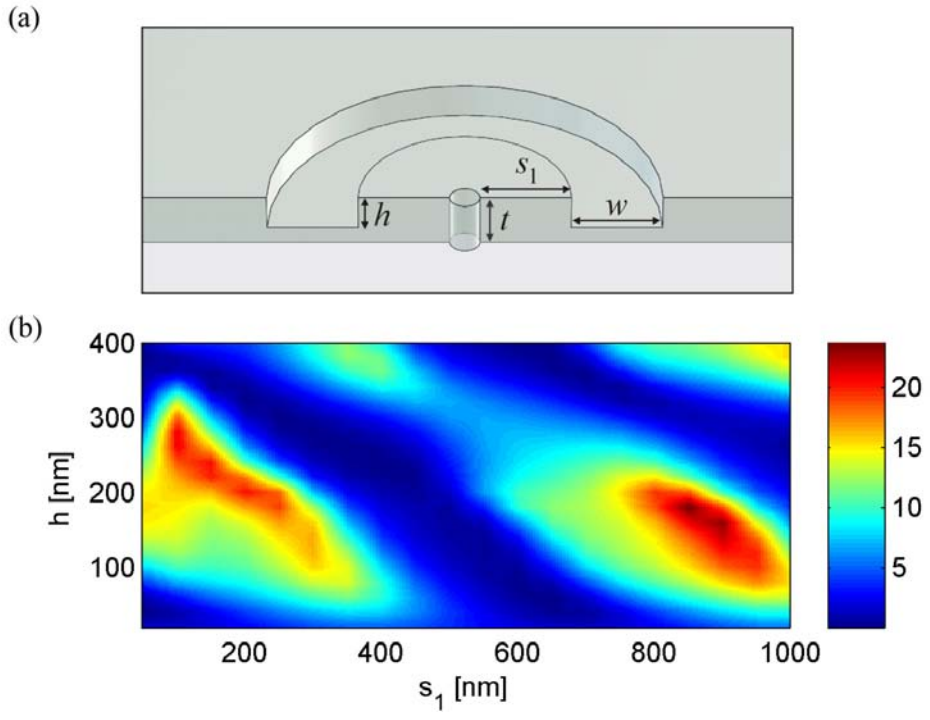

Figure 17. (a) Cross-sectional view of the modeled structure: a sub-wavelength 100 nm diameter cylindrical hole in a silver film (t = 515 nm) that is filled by a high index dielectric medium ($n_{co} = 2.8$) is surrounded by a single cylindrical groove with depth h and width w. (b) The normalized transmission efficiency (η) of a normally incident, linearly polarized plane wave through the cylindrical hole shown in (a) as a function of the groove depth (h) and the distance (s_1) between the central hole and the groove. In all cases, w = 300 nm, λ_0 = 650 nm, and $n_{Ag} = 0.055 + 4.44i$. [Paper II]

Due to the small size of the sub-wavelength apertures, transmitted light on the exit side of the metal film diffracts strongly in all directions, and a part of the light couples to surface waves propagating along the film. It has been noted that angular divergence of the beam emerging from the aperture can be tailored by forming corrugations on the exit side of the aperture film [129–131]. In addition, a focusing effect has been demonstrated with corrugations whose depths change with the distance from the aperture [132].

3.7 Aperture arrays

In 1998, Ebbesen *et al.* [11] published a paper on extraordinary optical transmission through sub-wavelength hole arrays. They noticed that an array consisting of tiny holes that do not support any propagating modes can transmit significantly more optical power at specific wavelengths than could be expected according to the classical theory of Bethe [46] (see Eq. (46)). By varying the angle of incidence, they observed that transmission maxima occur at different wavelengths to those in the case of normal incidence. The observed phenomenon is widely attributed to the surface plasmon polaritons (SPPs) excited by the periodic hole array [11, 133–138]. SPP is excited if the momentum of diffracted light matches with the SPP momentum as follows:

$$k_{\mathrm{SPP}} = k_x^{\mathrm{inc}} + k_y^{\mathrm{inc}} \pm nG_x \pm mG_y, \tag{50}$$

where k_x^{inc} and k_y^{inc} are transversal components of the incident wave vector in the array plane , $G_x = 2\pi / d_x$, $G_y = 2\pi / d_y$, and d_x and d_y are periods of the hole array in the x and y directions, respectively. k_{SPP} for an interface between a dielectric and a metallic medium is given by (48). When the hole size is relatively small in respect of the grating period, Eq. (50) in conjunction with (48) predicts incident wavelengths at which transmission maxima occur fairly accurately [136]. In general, however, the nature of SPPs change when they propagate on periodically corrugated metal films. Periodically structured films can be considered as surface polaritonic crystals [137, 139, 140] and SPPs propagating on them are widely referred to as SPP Bloch waves [136, 137, 141]. The SPP dispersion curves of metallic gratings are very different to those of planar surfaces and can exhibit, for instance, band gaps [142–145] or be extremely flat [146]. The general understanding is that light funnels through the hole arrays via SPP Bloch modes related to one or both metal interfaces [7, 139, 147]. The enhanced transmission can also occur through periodically textured metal films, even in the absence of holes or slits [139, 148, 149]. This phenomenon is less surprising after the awareness that classically opaque 60 nm thick silver film is almost transparent if prisms are placed on both sides into close vicinity of the metal film, and the film is illuminated at the SPP resonance angle [150]. The prism on the incident side couples light into SPPs and on the exit side SPPs back to the propagating light waves.

If the aperture arrays consist of holes supporting propagating modes, Fabry-Pérot resonances occur in the apertures and the film thickness thus also has strong influence on total transmittance [151, 152]. In addition, such an aperture array may not exhibit its transmission maxima when Eq. (50) is satisfied. Particularly with one-dimensional gratings consisting of sub-wavelength slits in a thick metal film, it has been observed [151, 153, 154] that under normally incident illumination, the matching of the grating period with the SPP wavelength ($\lambda_{\mathrm{SPP}} = 2\pi / k_{\mathrm{SPP}}$) results in a substantial reduction in transmission.

4. Towards higher data storage densities

Large capacity data storage markets are currently dominated by two technologies: optical and magnetic recording. Even though these recording technologies are very distinct, both are vigorously seeking compact ways to generate optical light spots with lateral dimensions of a few tens of nanometers. Magnetic recording is trying to overcome the superparamagnetic limit by heating the magnetic recording medium locally with a focused light spot [64, 155–162], whereas optical recording uses tiny light spots to directly read and write data marks residing on an optical disk [41–44, 163, 164].

4.1 Heat assisted magnetic recording

Conventional magnetic recording has demonstrated areal recording densities up to 400 Gb/in.^{2} [64]. With higher recording densities, however, the number of magnetic grains within each bit is so small that the signal-to-noise ratio is not sufficient for traditional recording heads. Thus, to further increase the recording density, the recording medium must be such that it consists of sufficiently small magnetic grains. A problem with this approach is that the magnetic coercivity of such a thermally stable medium is so high that its magnetic state is no longer switchable by the recording head [156]. Fortunately, this problem can be circumvented. The recording medium can be locally heated by a tiny light spot to reduce its coercivity momentarily and enable recording. The recorded bit is then quickly cooled back down to ambient temperature, at which its magnetic state remains stable. This approach is typically referred to as heat assisted magnetic recording (HAMR). It is estimated that HAMR enables areal densities in the range of 1–40 Tb/in.^{2} [64], the ultimate limit being 50–300 Tb/in.^{2} [158].

When the recording density is 1 Tb/in.^{2}, the bit size could be, for instance, 12.7 nm x 50.8 nm [158], with the first dimension being along the track and the latter across the track. As the heating along the track can be modulated via the

light source [158], the maximum dimension of the heating light spot should be around 50 nm. Optical transducers, such as C-apertures [64, 94, 117, 118, 155, 161, 165], bow-tie antennas [166], and planar solid immersion mirrors [157], which provide such a small light spot, have been heavily studied. The task is slightly eased by the fact that the recording head typically flies less than 20 nm above the recording medium [64]. Thus, if the optical transducer is connected to the recording head, the light emerging from the transducers, including evanescent waves, couples immediately to the recording medium without any significant lateral spreading. An interesting transducer construction is formed from a C-aperture and a solid immersion lens (SIL) [118, 165]. When a metal film containing the C-aperture is placed in close vicinity of the SIL base, the evanescent light produced in the SIL base can couple to SPPs, resulting in enhanced light coupling to the aperture. Another interesting combination may be a high index SIL with a circular aperture formed into its base. The high index filling enables light transmission through extremely small apertures, as illustrated in Section 3.3.

4.2 Optical data storage

Conventional optical disks, such as CDs and DVDs, are read and written using far field optics. The minimum full-width at half-maximum spot size of a readout beam is limited by diffraction to $\lambda_0 / (2\mathrm{NA})$ [156], where NA is the numerical aperture of the focusing lens and λ_0 is the free space wavelength, assuming that the lens is surround by air. In far field optics, NA is always smaller than one, and the minimum wavelength of available laser diodes is around 400 nm. Thus, the minimum spot size is larger than 200 nm. A smaller spot size can be attained with an optical transducer flying directly over the recording medium. For instance, marks with diameters of 60 nm have been written on a phase change medium using a tapered optical fiber [40], and marks down to 40 nm were recorded using a beaked metallic plate near-field optical probe [167]. A very different approach is based on the super-resolution near-field structure (super-RENS), which is an optically non-linear layer formed directly into the disk structure immediately above the data layer. When the non-linear layer is heated by the incident beam, it becomes transparent only at the center of the beam. Thus, the effective size of the formed dynamic aperture is much smaller than the spot size of the incident beam. In sequel, the non-linear layer is referred to as the super-resolution (SR) layer.

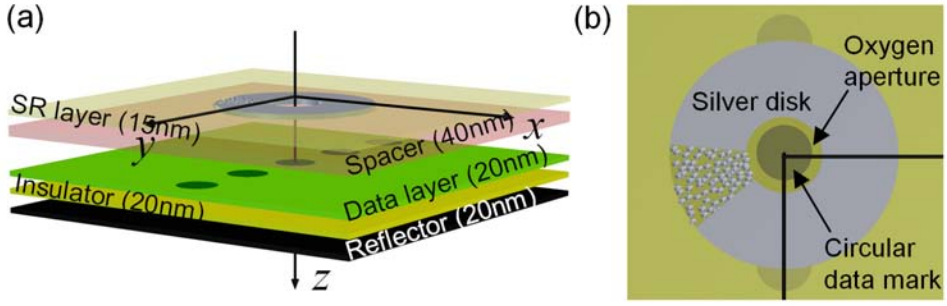

Figure 18. (a) Illustration of the modeled AgO_x SR disk structure. The cover and substrate layers above and below the layered structure are not shown. Layers are separated by air gaps to clarify the structure. The readout beam propagates along the z-axis and reflects from a mark in the data layer. (b) Top view of the AgO_x SR layer. The readout beam heats the SR layer so that it deforms locally into an aperture that contains oxygen and is surrounded by silver particles. The particles shown illustrate the formation of particles around the aperture. The particles were not present in the actual model and were replaced with a uniform silver disk having the thickness of the SR layer.

In the first super-RENS disks [168, 169], the SR layer was made of antimony (Sb), which is opaque in the crystalline form. When heated by the focused readout beam, antimony changes its phase and becomes momentarily transparent at the center of the beam [170, 171], where the intensity is the highest. It is also proposed that the Sb layer could work as a thermal lens [172, 173]. In 2000, an SR layer based on silver oxide (AgO_x) was introduced [174]. It was assumed that silver oxide decomposes into silver and oxygen in a small area heated above the threshold temperature by a focused laser beam. In the beginning, it was thought that silver particles formed a dot-shaped silver aggregate at the optical axis of the beam [174–176]. This silver dot, also called light scattering centre, could support localized surface plasmons, whose resonance is sensitive to the phase of the data mark. In the later study by Ho *et al.* [177], it was found that in addition to an aggregated silver cluster, the input beam may produce an aperture surrounded by silver particles if the energy dose delivered by the laser beam is high enough. As it was not clear how silver particles are spatially distributed in the AgOx layer, Paper V studied the readout modulations produced by the both structures in an attempt to gain some understanding of the operation principle of the AgOx SR layer.

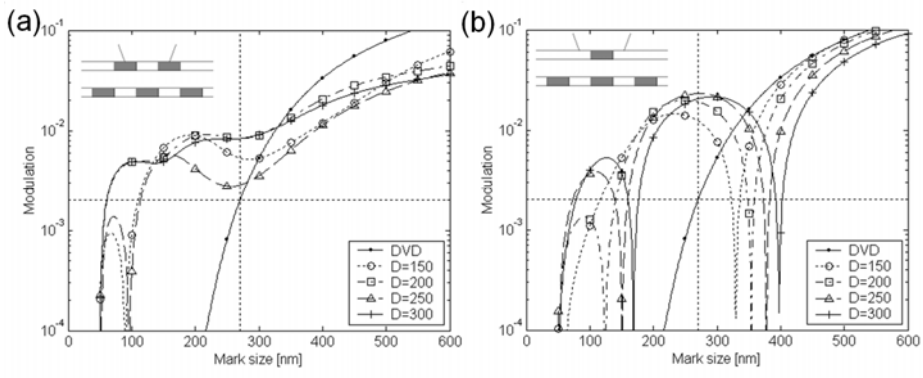

Figure 19. Readout modulation of an AgO_x SR disk without the insulator and reflector layers as a function of the circularly shaped mark size. The spacing between the marks equals with the mark size. (a) The AgO_x layer is deformed locally into an oxygen aperture, D in diameter, surrounded by a silver ring with a maximum diameter of 3D. (b) The AgO_x layer is decomposed into a cylindrical light scattering center with a diameter of D. In the both graphs, the vertical dotted line shows the smallest DVD mark size resolvable with the conventional DVD far-field optics, and the horizontal dotted line shows the corresponding modulation level. The SR, spacer, and data layer thicknesses are 15, 40, and 20 nm, respectively. [Paper V]

Paper V studies the readout modulation of AgOx super-RENS disks via the 3D FDTD method. An example of the modeled disk structure is shown in Figure 18(a). It was assumed that the readout beam heats the AgOx layer so that it deforms locally, either into an aperture that contains oxygen and is surrounded by silver particles, as illustrated in Figure 18(b), or into a light scattering center composed of silver particles. The model was simplified by replacing areas with silver particles by a uniform silver sheet. The optical performance of the studied structures was characterized via the readout modulation (M), which is calculated as: $M = (I_{\max} - I_{\min}) / (I_{\max} + I_{\min})$, where $I_{\min}$ and $I_{\max}$ are the reflected optical powers collected by the focusing lens when the incident beam reflects from the center of a mark and from the intervening space between the marks, respectively. The light intensity at the focusing lens was obtained by propagating the FDTD-calculated reflected near-field into the far-field via the angular spectrum representation [178]. The total power collected by the focusing lens was calculated by integrating the far-field intensity over the numerical aperture of the lens. Figure 19 shows examples of readout modulation results obtained with an oxygen aperture surrounded by silver and the light scattering center model. Both structures clearly enhance the modulation when the mark

size is smaller than 300 nm. With the light scattering center, however, nulls are present in the modulation curve with much larger mark sizes than with the aperture structure. The nulls are due to reversed intensity levels from the on-mark and off-mark locations. All in all, the aperture structure seemed to correlate better with the experimental results [174].

It was later found that the AgO_x layer does not function in a reversible manner [179]. When the data marks are recorded to the phase change layer, permanent defects consisting of silver particles are formed into the AgO_x layer. Surprisingly, no written marks were found from the data layer, i.e., it was completely crystalline. Thus, it was concluded that the defects, consisting of silver particles, function as data marks in the readout process.

5. Summary and conclusions

The squeezing of light into the sub-wavelength domain is a subject of utmost importance – in respect of both applications and the fundamental theory of light. Classical diffraction theories estimate that sub-wavelength apertures exhibit such weak transmission efficiencies that they are not of any use in practical applications. As a result of intense research and rapid development of computer hardware, modeling tools, and micro- and nanofabrication technologies in the last two decades, it has been found that by tuning the geometrical shape, the dielectric filling, and the surface structure as well as the polarization and wavelength of incident light, the optical transmission properties of sub-λ structures in metal films can be altered drastically. It is seen that sub-λ apertures and aperture arrays with updated outfits are certain to benefit a variety of applications. Examples include super-resolution data storage, heat assisted magnetic recording, optical microscopy, Raman spectroscopy, biosensors, optical filters, polarizers, transparent electrodes for displays and solar cells, beam shaping and near-field focusing. There is undoubtedly a large set of applications still to be discovered.

This thesis studied the transmission properties of sub-wavelength aperture structures formed into a metal film via FDTD simulations. It was found that a high refractive index dielectric filling in a sub-wavelength slit or a cylindrical hole can drastically change its transmission properties. When a cylindrical hole in a metal film is filled with a medium whose refractive index approaches to the imaginary part of the metal's refractive index, a propagating mode can be found even holes as small as 10 nm in diameter. The effect of surface corrugations on the aperture transmittance was also studied. It was found that surface corrugations can couple light impinging outside the aperture to surface waves that propagate towards the central aperture. Depending on the phase difference between the waveguide modes excited by the directly incident light and the surface waves,

destructive or constructive interference occurs within the aperture, resulting in enhanced or suppressed transmission. An aperture with a light trapping cavity was invented as a new kind of aperture structure. It was demonstrated that the light trapping cavity can enhance the transmission of a normally incident plane wave through a cylindrical hole in a metal film by a factor of 40. The coupling of SPPs into a slit in a metal film was explored via the scattered field technique. The introduced SF technique enables FDTD modeling of light scattering from dispersive scatterers in a dispersive stratified medium. Finally, it was demonstrated that data storage densities of conventional optical disks can be increased by a dynamical aperture structure formed into a non-linear mask layer located 40 nm above the data layer.

References

[1] Ditlbacher, H., Krenn, J. R., Schider, G., Leitner, A. and Aussenegg, F. R. Two-dimensional optics with surface plasmon polaritons. Applied Physics Letters 2002. Vol. 81, pp. 1762–1764.

[2] Wang, B. and Wang, G. P. Surface plasmon polariton propagation in nanoscale metal gap waveguides. Optics Letters 2004. Vol. 29, pp. 1992–1994.

[3] Tanaka, K. and Tanaka, M. Simulations of nanometric optical circuits based on surface plasmon polariton gap waveguide. Applied Physics Letters 2003. Vol. 82, pp. 1158–1160.

[4] Tanaka, K., Tanaka, M. and Sugiyama, T. Simulation of practical nanometric optical circuits based on surface plasmon polariton gap waveguides. Optics Express 2005. Vol. 13, pp. 256–266.

[5] Barnes, W. L., Dereux, A. and Ebbesen, T.W. Surface plasmon subwavelength optics. Nature 2003. Vol. 424, pp. 824–830.

[6] Barnes, W. L. Surface plasmon-polariton length scales: a route to sub-wavelength optics. Journal of Optics A: Pure and Applied Optics 2006. Vol. 8, pp. 87–93.

[7] Genet, C. and Ebbesen, T. W. Light in tiny holes. Nature 2007. Vol. 445, pp. 39–46.

[8] Ono, T., Esashi, M., Yamada, M., Sugawara, Y., Takahara, J. and Hane, K. Integrated and Functional Probes. In: Nano-Optics. Berlin: Springer-Verlag, 2002. Pp. 111–135.

[9] Raether, H. Surface Plasmons on Smooth and Rough Surfaces and on Gratings. Berlin: Springer-Verlag, 1998.

[10] Lewis, A., Isaacson, M., Harootunian, A. and Muray, A. Development of a 500 Å spatial resolution light microscope: I. light is efficiently transmitted through 1/16 diameter apertures. Ultramicroscopy 1984. Vol. 13, pp. 227–231.

[11] Ebbesen, T. W., Lezec, H. J., Ghaemi, H. F., Thio, T. and Wolff, P. A. Extraordinary optical transmission through sub-wavelength hole arrays. Nature 1998. Vol. 391, pp. 667–669.

[12] Aussenegg, F. R., Hohenau, A., Ditlbacher, H., Lamprecht, B., Krenn, J. R. and Leitner, A. Electron beam lithography, a helpful tool for nanooptics. Microelectronic Engineering 2006. Vol. 83, pp. 1464–1467.

[13] Tseng, A. A. Recent developments in nanofabrication using focused ion beams. Small 2005. Vol. 1, pp. 924–939.

[14] Suutala, A., Olkkonen, J., Cox, D. C., Lappalainen, J. and Jantunen, H. Inverted method for fabricating a nano-aperture device with subwavelength structures. Journal of Vacuum Science and Technology B 2009. Vol. 27, pp. 2457–2461.

[15] Gale, M. T., Gimkiewicz, C., Obi, S., Schnieper, M., Sochtig, E., Thiele, H. and Westenhofer, S. Replication technology for optical microsystems. Optics and Lasers in Engineering 2005. Vol. 43, pp. 373–386.

[16] Se, H. A., Jin-Sung, K. and Guo, L. J. Bilayer metal wire-grid polarizer fabricated by roll-to-roll nanoimprint lithography on flexible plastic substrate. Journal of Vacuum Science and Technology B 2007. Vol. 25, pp. 2388–2391.

[17] Skinner, J. L., Hunter, L. L., Talin, A. A., Provine, J. and Horsley, D. A. Large-area subwavelength aperture arrays fabricated using nanoimprint lithography. IEEE Transactions on Nanotechnology 2008. Vol. 7, pp. 527–531.

[18] Shi, H., Wang, C., Du, C., Luo, X., Dong, X. and Gao, H. Beam manipulating by metallic nano-slits with variant widths. Optics Express 2005. Vol. 13, pp. 6815–6820.

[19] Sun, Z. and Kim, H. K. Refractive transmission of light and beam shaping with metallic nano-optic lenses. Applied Physics Letters 2004. Vol. 85, pp. 642–644.

[20] Lee, H.-S., Yoon, Y.-T., Lee, S.-S., Kim, S.-H., and Lee, K.-D. Color filter based on a subwavelength patterned metal grating. Optics Express 2007. Vol. 15, pp. 15457–15463.

[21] Hu, X., Zhan, L. and Xia, Y. Color filters based on enhanced optical transmission of subwavelength-structured metallic film for multicolor organic light-emitting diode display. Applied Optics 2008. Vol. 47, pp. 4275–4279.

[22] Brolo, A. G., Gordon, R., Leathem, B. and Kavanagh, K. L. Surface plasmon sensor based on the enhanced light transmission through arrays of nanoholes in gold films. Langmuir 2004. Vol. 20, pp. 4813–4815.

[23] Stewart, M. E., Anderton, C. R., Thompson, L. B., Maria, J., Gray, S. K., Rogers, J. A. and Nuzzo, R. G. Nanostructured plasmonic sensors. Chemical reviews 2008. Vol. 108, pp. 494–521.

[24] Eftekhari, F., Escobedo, C., Ferreira, J., Duan, X., Girotto, E. M., Brolo, A. G., Gordon, R. and Sinton, D. Nanoholes as nanochannels: Flow-through plasmonic sensing. Analytical Chemistry 2009. Vol. 81, pp. 4308–4311.

[25] Liu, Y. and Blair, S. Fluorescence enhancement from an array of subwavelength metal apertures. Optics Letters 2003. Vol. 28, pp. 507–509.

[26] Liu, Y., Bishop, J., Williams, L., Blair, S. and Herron, J. Biosensing based upon molecular confinement in metallic nanocavity arrays. Nanotechnology 2004. Vol. 15, pp. 1368–1374.

[27] Garrett, S. H., Smith, L. H. and Barnes, W. L. Fluorescence in the presence of metallic hole arrays. Journal of Modern Optics 2005. Vol. 52, pp. 1105–1122.

[28] Hwang, E., Smolyaninov, I. I. and Davis, C. C. Surface plasmon polariton enhanced fluorescence from quantum dots on nanostructured metal surfaces. Nano Letters 2010. Vol. 10, pp. 813–820.

[29] Brolo, A. G., Arctander, E., Gordon, R., Leathem, B. and Kavanagh, K. L. Nanohole-enhanced raman scattering. Nano Letters 2004. Vol. 4, pp. 2015–2018.

[30] Reilly III, T. H., Corbman, J. D. and Rowlen, K. L. Vapor deposition method for sensitivity studies on engineered surface-enhanced raman scattering-active substrates. Analytical Chemistry 2007. Vol. 79, pp. 5078–5081.

[31] Anema, J. R., Brolo, A. G., Marthandam, P. and Gordon, R. Enhanced Raman scattering from nanoholes in a copper film. Journal of Physical Chemistry C 2008. Vol. 112, pp. 17051–17055.

[32] Schnabel, B., Kley, E.-B. and Wyrowski, F. Study on polarizing visible light by subwavelength-period metal-stripe gratings. Optical Engineering 1999. Vol. 38, pp. 220–226.

[33] Xu, M., Urbach, H. P., de Boer, D. K. G. and Cornelissen, H. J. Wire-grid diffraction gratings used as polarizing beam splitter for visible light and applied in liquid crystal on silicon. Optics Express 2005. Vol. 13, pp. 2303–2320.

[34] Wang, J. J., Chen, L., Liu, X., Sciortino, P., Liu, F., Walters, F. and Deng, X. 30-nm-wide aluminum nanowire grid for ultrahigh contrast and transmittance polarizers made by UV-nanoimprint lithography. Applied Physics Letters 2006. Vol. 89, 141105, 3 pp.

[35] Pang, Y. and Gordon, R. Metal nano-grid reflective wave plate. Optics Express 2009. Vol. 17, pp. 2871–2879.

[36] Kawata, S., Ohtsu, M. and Irie, M. Nano-Optics. Berlin: Springer-Verlag, 2002.

[37] de Fornel, F. Evanescent Waves From Newtonian Optics to Atomic Optics. Berlin: Springer-Verlag, 2001.

[38] Kawata, S. Near-Field Optics and Surface Plasmon Polaritons. Berlin: Springer-Verlag, 2001.

[39] Veerman, J. A., Otter, A. M., Kuipers, L. and Van Hulst, N. F. High definition aperture probes for near-field optical microscopy fabricated by focused ion beam milling. Applied Physics Letters 1998. Vol. 72, pp. 3115–3117.

[40] Betzig, E., Trautman, J. K., Wolfe, R., Gyorgy, E. M., Finn, P. L., Kryder, M. H. and Chang, C. H. Near-field magneto-optics and high density data storage. Applied Physics Letters 1992. Vol. 61, pp. 142–144.

[41] Mansuripur, M. and Sincerbox, G. Principles and techniques of optical data storage. Proceedings of the IEEE 1997. Vol. 85, pp. 1780–1796.

[42] Terris, B. D., Mamin, H. J., Rugar, D., Studenmund, W. R. and Kino, G. S. Near-field optical data storage using a solid immersion lens. Applied Physics Letters 1994. Vol. 65, pp. 388–90.

[43] Terris, B. D., Mamin, H. J. and Rugar, D. Near-field optical data storage. Applied Physics Letters 1996. Vol. 68, 141, 3 pp.

[44] Yoshikawa, H., Andoh, Y., Yamamoto, M., Fukuzawa, K., Tamamura, T. and Ohkubo, T. 7.5-MHz data-transfer rate with a planar aperture mounted upon a near-field optical slider. Optics Letters 2000. Vol. 25, pp. 67–69.

[45] Luo, X. and Ishihara, T. Subwavelength photolithography based on surface-plasmon polariton resonance. Optics Express 2004. Vol. 12, pp. 3055–3065.

[46] Bethe, H. A. Theory of diffraction by small holes. Physical Review 1944. Vol. 66, pp. 163–182.

[47] Yee, K. S. Numerical solution of initial boundary value problems involving Maxwell's equations in isotropic media. IEEE Transactions on Antennas and Propagation 1966. Vol. 14, pp. 302–307.

[48] Zhang, K. and Dejie, L. Electromagnetic Theory for Microwaves and Optoelectronics. Berlin: Springer-Verlag, 1998.

[49] Tai, C. T. Dyadic Green Functions in Electromagnetic Theory. Second Edition. New York: IEEE Press, 1993.

[50] Kong, J. A. Electromagnetic Wave Theory. Cambridge, Massachusetts, USA: EMW Publishing, 2000.

[51] Constantine, A. B. Advanced Engineering Electromagnetics. New York: John Wiley & Sons, 1989.

[52] Zakharian, A. R., Mansuripur, M. and Moloney, J. V. Transmission of light through small elliptical apertures. Optics Express 2004. Vol. 12, pp. 2631–2648.

[53] Hanson, G. W. and Yakovlev, A. B. Operator theory for electromagnetism: an introduction. New York: Springer-Verlag, 2001.

[54] Stone, J. M. Radiation and Optics: An Introduction to the Classical Theory. New York: McGraw-Hill Book Company, Inc., 1963.

[55] Mansuripur, M. Radiation pressure and the linear momentum of the electromagnetic field. Optics Express 2004. Vol. 12, pp. 5375–5401.

[56] Taflove, A. and Hagness, S. C. Computational Electrodynamics: The Finite-Difference Time-Domain Method. Second Edition. Boston: Artech House, Inc., 2000.

[57] Taflove, A. and Brodwin, M. E. Numerical solution of steady-state electromagnetic scattering problems using the time-dependent Maxwell's equations. IEEE Transactions on Microwave Theory and Techniques 1975. Vol. 23, pp. 623–30.

[58] Sullivan, D. M. Electromagnetic simulation using the FDTD method. New York: IEEE Press, 2000.

[59] Kunz, K. S. and Luebbers, R. J. The Finite Difference Time Domain Method for Electromagnetics. Boca Raton, Florida: CRC Press, 1993.

[60] Sadiku, M. N. O. Numerical Techniques in Electromagnetics. Second Edition. Boca Raton, Florida: CRC Press, 2000.

[61] Okoniewski, M., Mrozowski, M. and Stuchly, M. A. Simple treatment of multi-term dispersion in FDTD. IEEE Microwave and Guided Wave Letters 1997. Vol. 7, pp. 121–123.

[62] Kelley, D. F. and Luebbers, R. J. Piecewise linear recursive convolution for dispersive media using FDTD. IEEE Transactions on Antennas and Propagation 1996. Vol. 44, pp. 792–797.

[63] Johnson, P. B. and Christy, R. W. Optical constants of the noble metals. Physical Review B 1972. Vol. 6, pp. 4370–4379.

[64] Challener, W. A. and Itagi, A. V. Near-Field Optics for Heat-Assisted Magnetic Recording (Experiment, Theory, and Modeling). In: Modern Aspects of Electrochemistry No. 44. Springer New York, 2009. Pp. 53–111.

[65] Gedney, S. D. An anisotropic perfectly matched layer-absorbing medium for the truncation of FDTD lattices. IEEE Transactions on Antennas and Propagation 1996. Vol. 44, pp. 1630–1639.

[66] Berenger, J. P. A perfectly matched layer for the absorption of electromagnetic waves. Journal of Computational Physics 1994. Vol. 114, pp. 185–200.

[67] Gedney, S. D. Anisotropic PML absorbing media for the FDTD simulation of fields in lossy and dispersive media. Electromagnetics 1996. Vol. 16, pp. 399–415.

[68] Ashcroft, N. W. and Mermin, N. D. Solid State Physics. New York: Holt-Saunders, 1976.

[69] Schneider, J. B. and Abdijalilov, K. Analytic field propagation TFSF boundary for FDTD problems involving planar interfaces: PECs, TE, and TM. IEEE Transactions on Antennas and Propagation 2006. Vol. 54, pp. 2531–2542.

[70] Abdijalilov, K. and Schneider, J. B. Analytic field propagation TFSF boundary for FDTD problems involving planar Interfaces: Lossy material and evanescent fields. IEEE Antennas and Wireless Propagation Letters 2006. Vol. 5, pp. 454–458.

[71] Winton, S. C., Kosmas, P. and Rappaport, C. M. FDTD simulation of TE and TM plane waves at nonzero incidence in arbitrary Layered media. IEEE Transactions on Antennas and Propagation 2005. Vol. 53, pp. 1721–1728.

[72] Jiang, Y.-N, Ge, D.-B. and Ding, S.-J. Analysis of TF-SF boundary for 2D-FDTD with plane p-wave propagation in layered dispersive and lossy media. Progress in Electromagnetics Research 2008. Vol. 83, pp. 157–172.

[73] Richards, B. and Wolf, E. Electromagnetic Diffraction in Optical Systems. II. Structure of the Image Field in an Aplanatic System. Proceedings of the Royal Society of London. Series A, Mathematical and Physical Sciences 1959. Vol. 253, pp. 358–379.

[74] Volakis, J. L., Davidson, D. B., Guiffaut, C. and Mahdjoubi, K. A parallel FDTD algorithm using the MPI library. IEEE Antennas and Propagation Magazine 2001. Vol. 43, pp. 94–103.

[75] Prather, D. W. and Shi, S. Formulation and application of the finite-difference time-domain method for the analysis of axially symmetric diffractive optical elements. Journal of the Optical Society of America A 1999. Vol. 16, pp. 1131–1142.

[76] Baida, F. I., Van Labeke, D. and Pagani, Y. Body-of-revolution FDTD simulations of improved tip performance for scanning near-field optical microscopes. Optics Communications 2003. Vol. 225, pp. 241–252.

[77] Taflove, A. Advances in Computational Electrodynamics. Norwood, MA: Artech House, Inc., 1998.

[78] Kirchhoff, G. R. Zur Theorie der Lichtstrahlen. Ann. Phys. 1883, Vol. 18, pp. 663–695.

[79] Sommerfeld, A. Zur mathematischen Theorie der Beugungsercheinungen. Nachr. Kgl. Wiss. Göttingen 1894. Vol. 4, pp. 338–342.

[80] Lord Rayleigh. On the passage of waves through apertures in plane screens, and allied problems. Philosophical Magazine Series 5 1897, Vol. 43, pp. 259–272.

[81] Levine, H. and Schwinger, J. On the theory of diffraction by an aperture in an infinite plane screen. I. Physical Review 1948. Vol. 74, pp. 958–974.

[82] Levine, H. and Schwinger, J. On the theory of diffraction by an aperture in an infinite plane screen. II. Physical Review 1949. Vol. 75, pp. 1423–1432.

[83] Bouwkamp, C. J. Theoretical and numerical treatment of diffraction through a circular aperture. IEEE Transactions on Antennas and Propagation 1970. Vol. 18, pp. 152–176.

[84] English, R. E., Jr. and George, N. Diffraction from a small square aperture: approximate aperture fields. Journal of the Optical Society of America A 1988. Vol. 5, pp. 192–199.

[85] Roberts, A. Electromagnetic theory of diffraction by a circular aperture in a thick, perfectly conducting screen. Journal of the Optical Society of America A 1987. Vol. 4, pp. 1970–1983.

[86] Roberts, A. Near-zone fields behind circular apertures in thick, perfectly conducting screens. Journal of Applied Physics 1989. Vol. 65, pp. 2896–2899.

[87] Guha, S. and Gillen, G. D. Description of light propagation through a circular aperture using nonparaxial vector diffraction theory. Optics Express 2005. Vol. 13, pp. 1424–1447.

[88] Bouwkamp, C. J. Diffraction theory. Reports on Progress in Physics 1954. Vol. 17, pp. 35–100.

[89] Wannemacher, R. Plasmon-supported transmission of light through nanometric holes in metallic thin films. Optics Communications 2001. Vol. 195, pp. 107–118.

[90] Hafner, C. The Generalized Multipole Technique for Computational Electromagnetics. Boston: Artech House, 1990.

[91] Jin, J. The Finite Element Method in Electromagnetics. Second Edition. New York: John Wiley & Sons, Inc., 2002.

[92] Hibbins, A. P., Sambles, J. R. and Lawrence, C. R. Gratingless enhanced microwave transmission through a subwavelength aperture in a thick metal plate. Applied Physics Letters 2002. Vol. 81, pp. 4661–4663.

[93] Lockau, D., Zschiedrich, L. and Burger, S. Accurate simulation of light transmission through subwavelength apertures in metal films. Journal of Optics A: Pure and Applied Optics 2009. Vol. 11, 114013, 6 pp.

[94] Sendur, K. Perpendicular oriented single-pole nano-optical transducer. Optics Express 2010. Vol. 18, pp. 4920–4930.

[95] Tanaka, K. and Tanaka, M. Analysis and numerical computation of diffraction of an optical field by a subwavelength-size aperture in a thick metallic screen by use of a volume integral equation. Applied Optics 2004, Vol. 43, pp. 1734–1746.

[96] Vallius, T., Turunen, J., Mansuripur, M. and Honkanen, S. Transmission through single subwavelength apertures in thin metal films and effects of surface plasmons. Journal of the Optical Society of America A 2004. Vol. 21, pp. 456–463.

[97] Burke, J. J., Stegeman, G. I. and Tamir, T. Surface-polariton-like waves guided by thin, lossy metal films. Physical Review B (Condensed Matter) 1986. Vol. 33, pp. 5186–5201.

[98] Otto, A. Excitation of nonradiative surface plasma waves in silver by the method of frustrated total reflection. Zeitschrift fur Physik A (Atoms and Nuclei) 1968. Vol. 216, pp. 398–410.

[99] Kretschmann, E. and Raether, H. Radiative Decay of Non-Radiative Surface Plasmons Excited by Light. Zeitschrift fur Physik 1968. Vol. 239, pp. 2135–2136.

[100] Takakura, Y. Optical resonance in a narrow slit in a thick metallic screen. Physical Review Letters 2001. Vol. 86, pp. 5601–5603.

[101] Bravo-Abad, J., Martin-Moreno, L. and Garcia-Vidal, F. J. Transmission properties of a single metallic slit: from the subwavelength regime to the geometrical-optics limit. Physical Review E 2004. Vol. 69, 26601, 6 pp.

[102] Xie, Y., Zakharian, A. R., Moloney, J. V. and Mansuripur, M. Transmission of light through slit apertures in metallic films. Optics Express 2004. Vol. 12, pp. 6106–6121.

[103] Lindberg, J., Linfors, K., Setala, T., Kaivola, M. and Friberg, A. T. Spectral analysis of resonant transmission of light through a single sub-wavelength slit. Optics Express 2004. Vol. 12, pp. 623–632.

[104] Garcia-Vidal, F. J., Lezec, H. J., Ebbesen, T. W. and Martin-Moreno, L. Multiple paths to enhance optical transmission through a single subwavelength slit. Physical Review Letters 2003. Vol. 90, 213901, 4 pp.

[105] Huang, X. R., Peng, R. W., Wang, Z., Gao, F. and Jiang, S. S. Charge-oscillation-induced light transmission through subwavelength slits and holes. Physical Review A 2007. Vol. 76, 035802, 4 pp.

[106] Okamoto, K. Fundamentals of Optical Waveguides. San Diego, California: Academic Press, 2000.

[107] Scheuten, H. F., Kuzmin, N., Dubois, G., Visser, T. D., Gbur, G., Alkemade, P. F. A., Blok, H., T Hooft, G. W., Lenstra, D. and Eliel, E. R. Plasmon-assisted two-slit transmission: Young's experiment revisited. Physical Review Letters 2005. Vol. 94, 053901, 4 pp.

[108] Catrysse, P. B., Shin, H. and Fan, S. Propagating modes in subwavelength cylindrical holes. Journal of Vacuum Science and Technology B 2005. Vol. 23, pp. 2675–2678.

[109] Webb, K. J. and Li, J. Analysis of transmission through small apertures in conducting films. Physical Review B 2006. Vol. 73, 033401, 4 pp.

[110] Prade, B. and Vinet, J. Y. Guided optical waves in fibers with negative dielectric constant. Journal of Lightwave Technology 1994. Vol. 12, pp. 6–18.

[111] Stratonnikov, A. A., Bogatov, A. P., Drakin, A. E. and Kamenets, F. F. A semianalytical method of mode determination for a multilayer planar optical waveguide. Journal of Optics A: Pure and Applied Optics 2002. Vol. 4, pp. 535–539.

[112] Lagarias, J. C., Reeds, J. A., Wright, M. H. and Wright, P. E. Convergence properties of the Nelder-Mead simplex method in low dimensions. SIAM Journal on Optimization 1998. Vol. 9, pp. 112–147.

[113] Shin, H., Catrysse, P. B. and Fan, S. Effect of the plasmonic dispersion relation on the transmission properties of subwavelength cylindrical holes. Physical Review B 2005. Vol. 72, 085436, 7 pp.

[114] Shi, X., Hesselink, L. and Thornton, R. L. Ultrahigh light transmission through a C-shaped nanoaperture. Optics Letters 2003. Vol. 28, pp. 1320–1322.

[115] Itagi, A. V., Stancil, D. D., Bain, J. A. and Schlesinger, T. E. Ridge waveguide as a near-field optical source. Applied Physics Letters 2003. Vol. 83, pp. 4474–4476.

[116] Matteo, J. A., Fromm, D. P., Yuen, Y., Schuck, P. J., Moerner, W. E. and Hesselink, L. Spectral analysis of strongly enhanced visible light transmission through single C-shaped nanoapertures. Applied Physics Letters 2004. Vol. 85, pp. 648–650.

[117] Sendur, K., Challener, W. and Peng, C. Ridge waveguide as a near field aperture for high density data storage. Journal of Applied Physics 2004. Vol. 96, pp. 2743–2752.

[118] Sendur, K., Peng, C. and Challener, W. Near-field radiation from a ridge waveguide transducer in the vicinity of a solid immersion lens. Physical Review Letters 2005. Vol. 94, 043901, 4 pp.

[119] Peng, C., Jin, E. X., Clinton, T. W. and Seigler, M. A. Cutoff wavelength of ridge waveguide near field transducer for disk data storage. Optics Express 2008. Vol. 16, pp. 16043–16051.

[120] Thomas, D. A. and Hughes, H. P. Enhanced optical transmission through a subwavelength 1D aperture. Solid State Communications 2004. Vol. 129, pp. 519–524.

[121] Akarca-Biyikli, S. S., Bulu, I. and Ozbay, E. Resonant excitation of surface plasmons in one-dimensional metallic grating structures at microwave frequencies. Journal of Optics A: Pure and Applied Optics 2005. Vol. 7, pp. 159–164.

[122] Chen, L., Robinson, J. T. and Lipson, M. Role of radiation and surface plasmon polaritons in the optical interactions between a nano-slit and a nano-groove on a metal surface. Optics Express 2006. Vol. 14, pp. 12629–12636.

[123] Kalkum, F., Gay, G., Alloschery, O., Weiner, J., Lezec, H. J., Xie, Y. and Mansuripur, M. Surface-wave interferometry on single subwavelength slit-groove structures fabricated on gold films. Optics Express 2007. Vol. 15, pp. 2613–2621.

[124] Ung, B. and Sheng, Y. Optical surface waves over metallo-dielectric nanostructures: Sommerfeld integrals revisited. Optics Express 2008. Vol. 16, pp. 9073–9086.

[125] Thio, T., Pellerin, K. M., Linke, R. A., Lezec, H. J. and Ebbesen, T. W. Enhanced light transmission through a single subwavelength aperture. Optics Letters 2001. Vol. 26, pp. 1972–1974.

[126] Thio, T., Lezec, H. J., Ebbesen, T. W., Pellerin, K. M., Lewen, G. D., Nahata, A. and Linke, R. A. Giant optical transmission of sub-wavelength apertures: Physics and applications. Nanotechnology 2002. Vol. 13, pp. 429–432.

[127] Degiron, A. and Ebbesen, T. W. Analysis of the transmission process through single apertures surrounded by periodic corrugations. Optics Express 2004. Vol. 12, pp. 3694–3700.

[128] Lezec, H. J. and Thio, T. Diffracted evanescent wave model for enhanced and suppressed optical transmission through subwavelength hole arrays. Optics Express 2004. Vol. 12, pp. 3629–3651.

[129] Lezec, H. J., Degiron, A., Devaux, E., Linke, R. A., Martin-Moreno, L., Garcia-Vidal, F. J. and Ebbesen, T. W. Beaming light from a subwavelength aperture. Science 2002. Vol. 297, pp. 820–822.

[130] Garcia-Vidal, F. J., Martin-Moreno, L., Lezec, H. J. and Ebbesen, T. W. Focusing light with a single subwavelength aperture flanked by surface corrugations. Applied Physics Letters 2003. Vol. 83, pp. 4500–4502.

[131] Martin-Moreno, L., Garcia-Vidal, F. J., Lezec, H. J., Degiron, A. and Ebbesen, T. W. Theory of highly directional emission from a single subwavelength aperture surrounded by surface corrugations. Physical Review Letters 2003. Vol. 90, 167401, 4 pp.

[132] Wang, J. and Zhou, W. An annular plasmonic lens under illumination of circularly polarized light. Plasmonics 2009. Vol. 4, pp. 231–235.

[133] Ghaemi, H. F., Thio, T., Grupp, D. E., Ebbesen, T. W. and Lezec, H. J. Surface plasmons enhance optical transmission through subwavelength holes. Physical Review B 1998. Vol. 58, pp. 6779–6782.

[134] Kim, T. J., Thio, T., Ebbesen, T. W., Grupp, D. E. and Lezec, H. J. Control of optical transmission through metals perforated with subwavelength hole arrays. Optics Letters 1999. Vol. 24, pp. 256–258.

[135] Martin-Moreno, L., Garcia-Vidal, F. J., Lezec, H. J., Pellerin, K. M., Thio, T., Pendry, J. B. and Ebbesen, T. W. Theory of extraordinary optical transmission through subwavelength hole arrays. Physical Review Letters 2001. Vol. 86, pp. 1114–1117.

[136] Salomon, L., Grillot, F., Zayats, A. V. and de Fornel, F. Near-field distribution of optical transmission of periodic subwavelength holes in a metal film. Physical Review Letters 2001. Vol. 86, pp. 1110–1113.

[137] Zayats, A. V., Salomon, L. and De Fornel, F. How light gets through periodically nanostructured metal films: a role of surface polaritonic crystals. Journal of microscopy 2003. Vol. 210, pp. 344–349.

[138] Degiron, A. and Ebbesen, T. W. The role of localized surface plasmon modes in the enhanced transmission of periodic subwavelength apertures. Journal of Optics A: Pure and Applied Optics 2005. Vol. 7, pp. 90–96.

[139] Darmanyan, S. A., Neviere, M. and Zayats, A. V. Enhanced optical transmission via tunnel coupling in surface polaritonic crystals. In: Nonlinear Waves: Classical and Quantum Aspects. Netherlands: Kluwer Academic Publishers, 2004. Pp. 313–326.

[140] Zayats, A. V., Smolyaninov, I. I. and Maradudin, A. A. Nano-optics of surface plasmon polaritons. Physics Reports 2005. Vol. 408, pp. 131–314.

[141] Chang, S.-H., Gray, S. K. and Schatz, G. C. Surface plasmon generation and light transmission by isolated nanoholes and arrays of nanoholes in thin metal films. Optics Express 2005. Vol. 18, pp. 3150–3165.

[142] Barnes, W. L., Preist, T. W., Kitson, S. C. and Sambles, J. R. Physical origin of photonic energy gaps in the propagation of surface plasmons on gratings. Physical Review B 1996. Vol. 54, pp. 6227–6244.

[143] Kitson, S. C., Barnes, W. L. and Sambles, J. R. Full photonic band gap for surface modes in the visible. Physical Review Letters 1996. Vol. 77, pp. 2670–2673.

[144] Garcia-Vidal, F., Sanchez-Dehesa, J., Dechelette, A., Bustarret, E., Lopez-Rios, T., Fournier, T. and Pannetier, B. Localized surface plasmons in lamellar metallic gratings. Journal of Lightwave Technology 1999. Vol. 17, pp. 2191–2195.

[145] Collin, S., Pardo, F., Teissier, R. and Pelouard, J.-L. Strong discontinuities in the complex photonic band structure of transmission metallic gratings. Physical Review B 2001. Vol. 63, 033107, 4 pp.

[146] Tan, W.-C., Preist, T. W., Sambles, J. R. and Wanstall, N. P. Flat surface-plasmon-polariton bands and resonant optical absorption on short-pitch metal gratings. Physical Review B 1999. Vol. 59, pp. 12661–12666.

[147] Liu, H. and Lalanne, P. Microscopic theory of the extraordinary optical transmission. Nature 2008. Vol. 452, pp. 728–731.

[148] Schroter, U. and Heitmann, D. Surface-plasmon-enhanced transmission through metallic gratings. Physical Review B 1998. Vol. 58, pp. 15419–15421.

[149] Avrutsky, I., Zhao, Y. and Kochergin, V. Surface-plasmon-assisted resonant tunneling of light through a periodically corrugated thin metal film. Optics Letters 2000. Vol. 25, pp. 595–597.

[150] Dragila, R., Luther-Davies, B. and Vukovic, S. High transparency of classically opaque metallic films. Physical Review Letters 1985. Vol. 55, pp. 1117–1120.

[151] Xie, Y., Zakharian, A. R., Moloney, J. V. and Mansuripur, M. Transmission of light through a periodic array of slits in a thick metallic film. Optics Express 2005. Vol. 13, pp. 4485–4491.

[152] Baida, F. I. and Van Labeke, D. Light transmission by subwavelength annular aperture arrays in metallic films. Optics Communications 2002. Vol. 209, pp. 17–22.

[153] Cao, Q. and Lalanne, P. Negative role of surface plasmons in the transmission of metallic gratings with very narrow slits. Physical Review Letters 2002. Vol. 88, 057403, 4 pp.

[154] Xie, Y., Zakharian, A. R., Moloney, J. V. and Mansuripur, M. Transmission of light through periodic arrays of sub-wavelength slits in metallic hosts. Optics Express 2006. Vol. 14, pp. 6400–6413.

[155] Challener, W. A., McDaniel, T. W., Mihalcea, C. D., Mountfield, K. R., Pelhos, K. and Sendur, I. K. Light delivery techniques for heat-assisted magnetic recording. Japanese Journal of Applied Physics 2003. Vol. 42, pp. 981–988.

[156] McDaniel, T. W., Challener, W. A. and Sendur, K. Issues in heat-assisted perpendicular recording. IEEE Transactions on Magnetics 2003. Vol. 39, pp. 1972–1979.

[157] Challener, W. A., Mihalcea, C., Peng, C. and Pelhos, K. Miniature planar solid immersion mirror with focused spot less than a quarter wavelength. Optics Express 2005. Vol. 13, pp. 7189–7197.

[158] McDaniel, T. W. Ultimate limits to thermally assisted magnetic recording. Journal of Physics Condensed Matter 2005. Vol. 17, pp. 315–332.

[159] Rausch, T., Mihalcea, C., Pelhos, K., Karns, D., Mountfield, K., Kubota, Y. A., Wu, X., Wu, G., Challener, W. A., Peng, C., Li, L., Hsia, Y.-T. and Gage, E. C. Near field heat assisted magnetic recording with a planar solid immersion lens. Japanese Journal of Applied Physics 2006. Vol. 45, pp. 1314–1320.

[160] Rottmayer, R. E., Batra, S., Buechel, D., Challener, W. A., Hohlfeld, J., Kubota, Y., Li, L., Lu, B., Mihalcea, C., Mountfield, K., Pelhos, K., Peng, C., Rausch, T., Seigler, M. A., Weller, D. and Yang, X. Heat-assisted magnetic recording. IEEE Transactions on Magnetics 2006. Vol. 42, pp. 2417–2421.

[161] Ikkawi, R., Amos, N., Lavrenov, A., Krichevsky, A., Teweldebrhan, D. B., Ghosh, S., Balandin, A. A., Litvinov, D. and Khizroev, S. Near-field optical transducer for heat-assisted magnetic recording for beyond-10-Tbit/in^2 densities. Journal of Nanoelectronics and Optoelectronics 2008. Vol. 3, pp. 44–54.

[162] Seigler, M. A., Challener, W. A., Gage, E., Gokemeijer, N., Ju, G., Lu, B., Pelhos, K., Peng, C., Rottmayer, R. E., Yang, X., Zhou, H. and Rausch, T. Integrated heat assisted magnetic recording head: Design and recording demonstration. IEEE Transactions on Magnetics 2008. Vol. 44, pp. 119–124.

[163] Milster, T. D., Jo, J. S., Hirota, K., Shimura, K. and Zhang, Y. The nature of the coupling field in optical data storage using solid immersion lenses. Japanese Journal of Applied Physics 1999. Vol. 38, pp. 1793–1794.

[164] Yatsui, T., Kourogi, M., Tsutsui, K., Ohtsu, M. and Takahashi, J. High-density-speed optical near-field recording-reading with a pyramidal silicon probe on a contact slider. Optics Letters 2000. Vol. 25, pp. 1279–1281.

[165] Sendur, K., Peng, C. and Challener, W. Condenser-transducer configuration for improving radiation efficiency of near-field optical transducers. Materials Research Society Symposium Proceedings 2005. Vol. 834, pp. 197–206.

[166] Sendur, K. and Challener, W. Near-field radiation of bow-tie antennas and apertures at optical frequencies. Journal of microscopy 2003. Vol. 210, pp. 279–283.

[167] Matsumoto, T., Anzai, Y., Shintani, T., Nakamura, K. and Nishida, T. Writing 40 nm marks by using a beaked metallic plate near-field optical probe. Optics Letters 2006. Vol. 31, pp. 259–261.

[168] Tominaga, J., Nakano, A. T. and Atoda, N. An approach for recording and readout beyond the diffraction limit with an Sb thin film. Applied Physics Letters 1998. Vol. 73, pp. 2078–2080.

[169] Nakano, T., Sato, A., Fuji, H., Tominaga, J. and Atoda, N. Transmitted signal detection of optical disks with a superresolution near-field structure. Applied Physics Letters 1999. Vol. 75, pp. 151–153.

[170] Fukaya, T., Tominaga, J., Nakano, T. and Atoda, N. Optical switching property of a light-induced pinhole in antimony thin film. Applied Physics Letters 1999. Vol. 75, pp. 3114–3116.

[171] Din, P. T., Chi, W. Y., Wei, C. L., Fu, H. H., Huang, H. J., Chen, M., Tza, F. T., Chin, H. L. and Chwei, J. Y. Dynamic aperture of near-field super resolution structures. Japanese Journal of Applied Physics 2000. Vol. 39, pp. 982–983.

[172] Wei, J. and Gan, F. Thermal lens model of Sb thin film in super-resolution near-field structure. Applied Physics Letters 2003. Vol. 82, pp. 2607–2609.

[173] Wei, J., Zhou, F., Wang, Y., Gan, F., Wu, Y. and Gu, D. Optical near-field simulation of Sb thin film thermal lens and its application in optical recording. Journal of Applied Physics 2005. Vol. 97, 073102, 5 pp.

[174] Fuji, H., Tominaga, J., Men, L., Nakano, T., Katayama, H. and Atoda, N. A near-field recording and readout technology using a metallic probe in an optical disk. Japanese Journal of Applied Physics 2000. Vol. 39, pp. 980–981.

[175] Tominaga, J., Kim, J., Fuji, H., Buchel, D., Kikukawa, T., Men, L., Fukuda, H., Sato, A., Nakano, T., Tachibana, A., Yamakawa, Y., Kumagai, M., Fukaya, T. and Atoda, N. Super-resolution near-field structure and signal enhancement by surface plasmons. Japanese Journal of Applied Physics 2001. Vol. 40, pp. 1831–1834.

[176] Nakano, T., Yamakawa, Y., Tominaga, J. and Atoda, N. Near-field optical simulation of super-resolution near-field structure disks. Japanese Journal of Applied Physics 2001. Vol. 40, pp. 1531–1535.

[177] Ho, F. H., Chang, H. H., Lin, Y. H., Chen, B., Wang, S. and Tsai, D. P. Functional structures of AgOx thin film for near-field recording. Japanese Journal of Applied Physics 2003. Vol. 42, pp. 1000–1004.

[178] Goodman, J. W. Introduction to Fourier Optics. Second Edition. Singapore: McGraw-Hill, 1996.

[179] Kikukawa, T., Tachibana, A., Fuji, H. and Tominaga, J. Recording and readout mechanisms of super-resolution near-field structure disc with silver-oxide layer. Japanese Journal of Applied Physics 2003. Vol. 32, pp. 1038–1039.

PAPER I

Light transmission through a high index dielectric-filled sub-wavelength hole in a metal film

In: Optics Express 2005.
Vol. 13, No. 18, pp. 6980–6989.

Light transmission through a high index dielectric-filled sub-wavelength hole in a metal film

Juuso Olkkonen and Kari Kataja

VTT Electronics, Kaitovayla 1, P.O. Box 1100, FIN-90571 Oulu, Finland
Juuso.Olkkonen@vtt.fi

Dennis G. Howe

University of Arizona, Optical Sciences Center, Tucson, AZ 85721-0094, USA
dghowe@optics.arizona.edu

Abstract: We investigate transmission of a normally incident, linearly polarized plane wave through a circular sub-wavelength hole in a metal film filled by a high index dielectric medium. We demonstrate for the first time that the transmission efficiency of such holes exhibits a Fabry-Pérot-like behaviour versus thickness of the metal film, similar to that exhibited by sub-wavelength slits in metal films illuminated by TM-polarized plane waves. We show that by reducing the imaginary part of the propagation constant of the hybrid HE_{11} mode and by fortifying the Fabry-Pérot resonance, the high index dielectric filling can greatly enhance light transmission through a circular sub-wavelength hole.

OCIS codes: 050.1940 (Diffraction); 050.1220 (Apertures).

References and links

1. H. A. Bethe, "Theory of Diffraction by Small Holes," Phys. Rev. **66**, 163-182 (1944).
2. A. Taflove and S. C. Hagness, *Computational Electrodynamics: The Finite Difference Time Domain Method* (Second Edition, Artech House, Boston, 2000).
3. A. R. Zakharian, M. Mansuripur, and J. V. Moloney, "Transmission of light through small elliptical apertures," Opt. Express **12,** 2631-2648 (2004), http://www.opticsexpress.org/abstract.cfm?URI=OPEX-12-12-2631.
4. C. Hafner, *The Generalized Multipole Technique for Computational Electromagnetics* (Artech House, Boston, 1990).
5. R. Wannemacher, "Plasmon supported transmission of light through nanometric hole in metallic thin films," Optics Comm. **195**, 107-118 (2001).
6. J. Jin, *The Finite Element Method in Electromagnetics* (John Wiley & Sons, New York, 2002).
7. A. P. Hippins, J. R. Sambles, and C. R. Lawrence, "Gratingless enhanced microwave transmission through a subwavelength aperture in a thick metal plate," Appl. Phys. Lett. **81**, 4661-4663 (2002).
8. F. J. Garcia de Abajo, "Light transmission through a single cylindrical hole in a metallic film," Opt. Express **10,** 1475-1484 (2002), http://www.opticsexpress.org/abstract.cfm?URI=OPEX-10-25-1475.
9. T. Thio, K. M. Pellerin, and R. A. Linke, "Enhanced light transmission through a single subwavelength aperture," Optics Lett. **26**, 1972-1974 (2001).
10. A. Degiron and T. W. Ebbesen, "Analysis of the transmission process through single apertures surrounded by periodic corrugations," Opt. Express **12,** 3694-3700 (2004), http://www.opticsexpress.org/abstract.cfm?URI=OPEX-12-16-3694.
11. P. B. Johnson and R. W. Christy, "Optical Constants of the Noble Metals," Phys. Rev. B **6**, 4370-4379 (1972).
12. M. Okoniewski, M. Mrozowski, and M. A. Stuchly, "Simple Treatment of Multi-Term Dispersion in FDTD," IEEE Microwave Guided Wave Lett. **7**, 121-123 (1997).

#7948 - $15.00 USD
Received 27 June 2005; revised 29 July 2005; accepted 25 August 2005

13. Y. Takakura, "Optical Resonance in a Narrow Slit in a Thick Metallic Screen," Phys. Rev. Lett. **86**, 5601 – 5603 (2001).
14. K. Okamoto, *Fundamentals of Optical Waveguides* (Academic Press, San Diego, 2000).
15. E. D. Palik, *Handbook of Optical Constants of Solids* (Academic Press, New York, 1985).

1. Introduction

Modern optical technologies such as near-field scanning optical microscopy, optical lithography, heat-assisted magnetic recording and optical data storage demand efficient near-field light sources that provide light confinement well beyond the fundamental diffraction limit. In theory, the fundamental diffraction limit can be exceeded – in a brute force fashion − by spatially limiting the extent of an incident wavefront by imposing a very small transmitting aperture in the path of an incident light beam. In practice, however, this approach suffers from the extremely small light transmission efficiency through the aperture. According to the Bethe's law [1], the transmission coefficient of a sub-wavelength circular hole, which is defined as a ratio of the transmitted power through the hole to the incident power falling into the entrance pupil of the hole, in an infinitely thin perfectly conduction film is proportional to $(R/\lambda_0)^4$, where R is the aperture radius and λ_0 is the free space wavelength. Due to the strong assumptions of Bethe's law, it only superficially describes the transmission properties of a sub-wavelength hole. Analysis of practical physical realizations of small apertures requires rigorous electromagnetic modelling tools such as the finite difference time domain (FDTD) method [2,3], multiple multi-pole technique [4,5] or the finite element method [6,7], which can take into account the finite conductivity as well as the finite thickness of the metal film.

The transmission properties of sub-wavelength apertures have recently been studied by several authors [3,5,8]. For example, Wannemacher [5] has studied the fundamental characteristics of a single circular hole in thin metal films, as well as the role played by surface plasmon polaritons in the transmission process, while Zakharian *et al.* [3] have been developing an intuitive description of the behavior of electromagnetic fields in elliptical apertures. García de Abajo [8] has investigated light transmission through simple circular holes in perfectly conducting thin films and holes containing additional structure such as sphere or a high index dielectric filling, which seems to improve the transmission efficiency at specific wavelengths. Enhanced transmission through cylindrical holes in metal films surrounded by periodic surface corrugations has also gained lots of interest [9,10] in recent years. These transmission enhancements are attributed to the influence of surface plasmon polaritons, which are excited by the surface corrugations [9,10].

In this paper, we explore the characteristic properties of single sub-wavelength holes in metal films filled by a high index dielectric medium. We begin our analysis by analytically investigating the propagation constant (β) of guided modes that are supported by infinitely long cylindrical holes in a silver medium. Then, we study the dependency of β on the refractive index of the hole. Next, the body-of-revolution finite difference time domain (BOR-FDTD) method is employed to analyze the light transmission through sub-wavelength holes in a metallic (conductive) medium, when such holes are filled by a high index dielectric medium. The light transmission of these holes is compared to the transmission of similar non-filled holes in the identical medium. We find that the high index dielectric filling improves the transmission efficiency by over two orders of magnitude and that the sub-wavelength cylindrical holes exhibit a Fabry-Pérot-like interference behaviour, similar to the transmission exhibited by two-dimensional metallic slits [13] under TM polarized illumination.

2. Numerical simulation model

The modeled geometry is schematically depicted in Fig. 1. A linearly polarized plane wave having free space wavelength of 488nm normally impinges on a cylindrical hole of radius r in laterally infinite silver film ($n_{Ag} = 0.05 + 3.02j$) of thickness t. The refractive index of silver was interpolated from the experimental data presented by Johnson *et al.* [11]. The symbols n_c,

#7948 - $15.00 USD Received 27 June 2005; revised 29 July 2005; accepted 25 August 2005

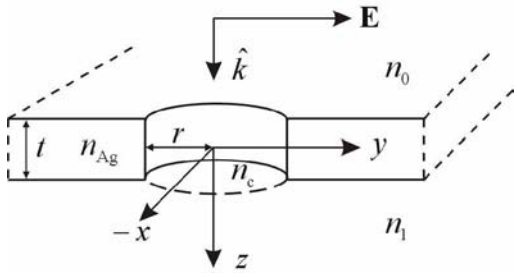

Fig. 1. Illustration of the modeled system. A cylindrical hole of radius r in a laterally infinite silver film of thickness t is illuminated by a normally incident, linearly polarized plane wave. The refractive indices of the hole, silver film, incident medium and the exit medium are denoted by n_c, n_{Ag}, n_0, and n_1, respectively.

n_0 and n_1 denote the refractive indexes of the hole, incident medium and the exit medium, respectively. In this study, we consider only free standing structures, i.e., $n_0 = n_1 = 1.0$.

The light interaction with the metallic hole is modeled by the BOR-FDTD method [2], which assumes that the physical structure to be modeled is cylindrically symmetric. The BOR-FDTD method represents the electric and magnetic field components in cylindrical coordinates (ρ, ϕ, z), where ρ, ϕ, and z have their conventional meanings. Due to fact that, in the cylindrical coordinates, the electric and magnetic field components are periodic in ϕ, we can represent them as complex Fourier series:

$$\mathbf{E}(\rho,\phi,z) = \sum_{m=0}^{\infty} \mathbf{E}_m(\rho,z)\exp(jm\phi), \tag{1}$$

$$\mathbf{H}(\rho,\phi,z) = \sum_{m=0}^{\infty} \mathbf{H}_m(\rho,z)\exp(jm\phi), \tag{2}$$

The complex amplitudes of $\mathbf{E}_m(\rho,z)$ and $\mathbf{H}_m(\rho,z)$ are are solved in a two-dimensional mesh, which is a significant advantage compared to the three-dimensional FDTD method. As an additional advantage, the BOR-FDTD method resolves exactly the cylindrical shape of the structure. In the series expansions (1) and (2), the mode number m goes from zero to infinity. In practice, the incident field defines the number of modes that must be solved. For example, problems in which the incident field is a linearly polarized plane wave, or a Gaussian beam, or a hybrid HE_{1n} mode of an optical fiber, require only the solution of the mode $m = 1$. On the other hand, a radially polarized Bessel beam or the TM_{01} mode of an optical fiber requires only the solution of the mode $m = 0$. The computation domain is terminated using uniaxial perfectly matched layer (UPML) absorbing boundary condition [2], and materials in which the real part of the refractive index is smaller than the imaginary part, as is the case with noble metals at optical frequencies, are modeled via the Lorentz dispersion model based on the auxiliary differential equation [12].

In this study, we model only the interaction of a normally incident, linearly polarized plane wave with a sub-wavelength hole in a metal film that has infinite extent in lateral directions. The laterally infinite metal film is accomplished by terminating the metal film directly by UPML. The incident plane wave is then excited by the TF/SF technique [2], which is modified to enable modelling of the problem as follows: Since the background structure in which the sub-wavelength hole resides is invariant in the x and y directions, propagation of normally incident plane waves through the background structure can be modelled using a one-dimensional FDTD simulation. This one-dimensional simulation, which is run simultaneously with the actual BOR-FDTD simulation, is then used as a look-up table that defines the incident field for the TF/SF technique. The use of look-up tables with the TF/SF technique is described in detail in Ref. [2].

To obtain accurate results with the BOR-FDTD method, the two-dimensional BOR-FDTD mesh has to be adequately sampled. In practice, a mesh with at least 30 mesh points

#7948 - $15.00 USD Received 27 June 2005; revised 29 July 2005; accepted 25 August 2005

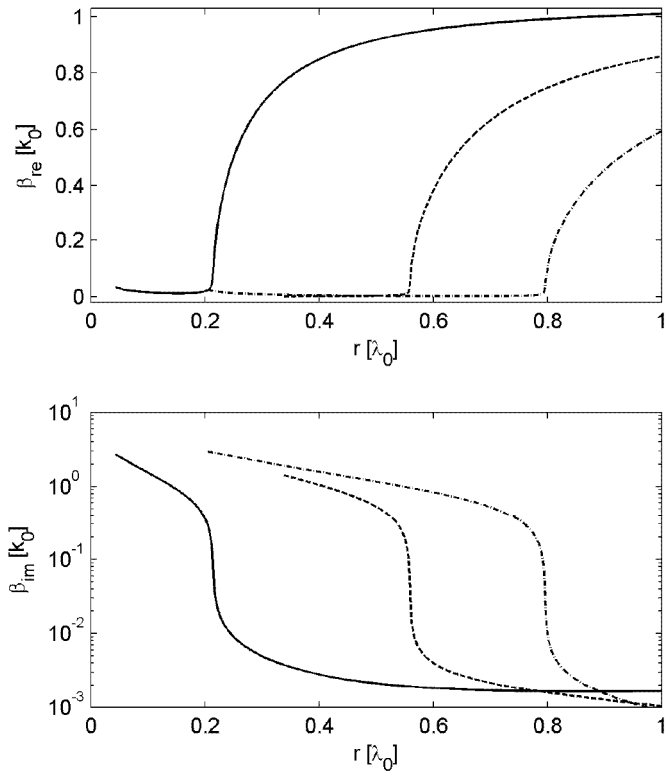

Fig. 2. Complex propagation constant ($\beta = \beta_{re} + j\beta_{im}$) of guided HE_{1n} modes (n = 1: solid line, n = 2: dashed line, n = 3: dotted-dashed line) as a function of the hole radius (r) for an infinitely long air hole in a silver medium. λ_0 = 488nm, $k_0 = 2\pi/\lambda_0$.

per wavelength is required to keep numerical dispersion errors under control [2]. In this study, we use a uniform mesh with $\Delta\rho = \Delta z = r/20$, where r is the radius of the cylindrical hole (see Fig. 1), and $\Delta\rho$ and Δz are the mesh space increments in the ρ and z directions, respectively. With such a sampling, we obtain accurate results for film thicknesses starting from $10\Delta z$ to tens of micrometers.

3. Results

When a normally incident plane wave interacts with a cylindrical hole in a metal film, it can excite only hybrid HE_{1n} ($n \geq 1$) waveguide modes, in which $E_z \neq 0$ and $H_z \neq 0$. This is due to the fact that only the HE_{1n} modes have the same angular dependency (in the azimuthal angle θ) as the linearly polarized plane wave propagating in the z direction. The complex propagation constants (β) of the HE_{1n} modes can be solved in the complex β domain using standard theories of dielectric optical fibers [14] without the weakly guiding assumption.

First, we shall consider the complex propagation constant of the HE_{1n} modes of an infinitely long air-filled hole in a silver medium as a function of the hole radius (r) at the wavelength of 488nm. The numerically obtained results are shown in Fig. 2. It is observed that when $r \leq \lambda_0$, the silver waveguide supports only the HE_{11}, HE_{12} and HE_{13} modes with the effective cut-off radii of $0.21\lambda_0$, $0.56\lambda_0$ and $0.8\lambda_0$, respectively. Second, we shall describe the dependency of the propagation wave vector β on the refractive index of the hole (n_c). In Fig.

#7948 - $15.00 USD Received 27 June 2005; revised 29 July 2005; accepted 25 August 2005

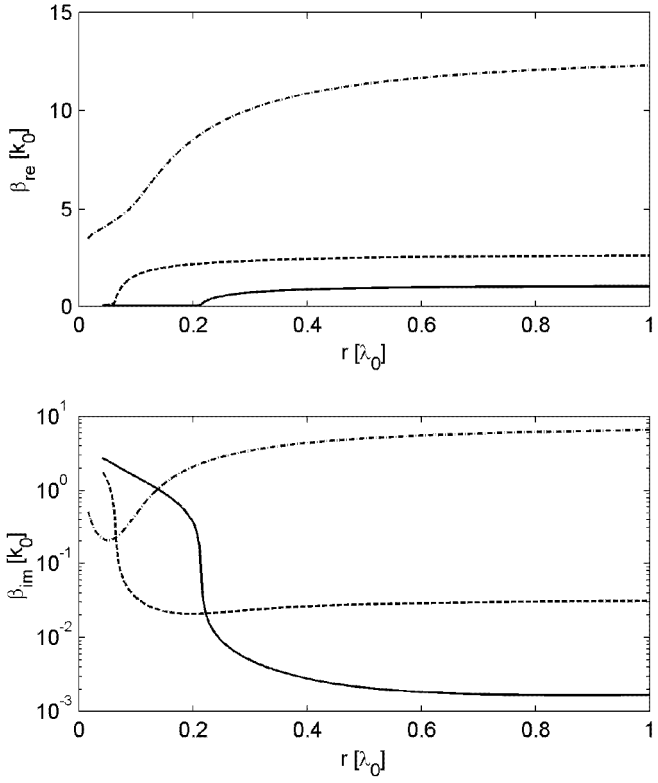

Fig 3. Complex propagation constant ($\beta = \beta_{re} + j\beta_{im}$) of guided HE_{11} modes as a function of the hole radius (r) for an infinitely long dielectric-filled (n_c = 1.0: solid line, n_c = 2.0: dashed line, n_c = 3.0: dashed-dotted line) hole in a silver medium. λ_0 = 488nm, $k_0 = 2\pi/\lambda_0$.

3, we show β of the HE_{11} mode as a function the hole's radius for three different refractive indices of the medium within the hole: n_c = 1.0, 2.0, and 3.0. We observe that by filling the hole by a high index dielectric medium, the cut-off radii of the HE_{11} mode can be significantly reduced. When n_c = 3.0, the imaginary part of β has rather interesting behaviour: It has a local minimum around $0.05\lambda_0$ after which β is an increasing function of hole radius. Now, one might think that there is no light transmission through a metal-clad circular waveguides for which, e.g, n_c = 3.0 and $r = \lambda_0$ due to the large value of the imaginary part of the waveguide's β. However, this is not the case. Light propagation can occur via higher order HE_{1n} modes, which are not shown in Fig. 3. The just mentioned peculiar behaviour of the HE_{11} mode, when n_c = 3.0, is probably due to fact that the absolute values of the real parts of the dielectric constants of silver and the hole are converging to each other, i.e., $|\mathrm{Re}\{n_c^2\}| \rightarrow |\mathrm{Re}\{n_{Ag}^2\}|$.

For the rest of this study, we shall restrict ourselves to two distinct hole radii: r = 25nm and r = 50nm. Figure 4 shows β for the HE_{11} mode as a function of n_c for the selected hole radii. We stress that these radii do not support any other HE_{1n} modes. We find that the imaginary part of β starts to decrease, while the real part exhibits a simultaneous increase, when n_c becomes larger than 2.2 in the case of r = 25nm and larger than 1.6 with r = 50nm. The imaginary part of β gains its minimum value when $n_c \approx 2.5$ (with r = 25 nm), or when $n_c \approx 2.0$ (with r = 50nm). From the view point of light transmission through a sub-wavelength

#7948 - $15.00 USD Received 27 June 2005; revised 29 July 2005; accepted 25 August 2005

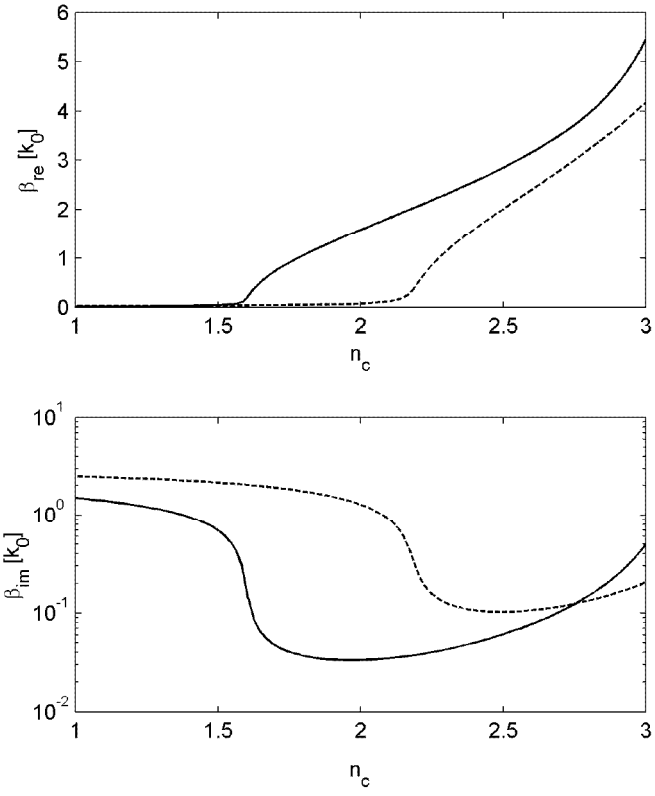

Fig. 4. Complex propagation constant ($\beta = \beta_{re} + j\beta_{im}$) of guided HE_{11} mode of a dielectric hole in an infinitely thick silver medium as a function of the refractive index of the hole (n_c) for two different hole radii: r = 50nm (solid line) and r = 25nm (dashed line).

hole, we would expect the maximum transmission to occur when the imaginary part of the wave vector of the HE_{11} mode is minimized. To verify this expectation, we next utilize the BOR-FDTD method to predict how the transmission efficiency of a sub-wavelength hole in a finitely thick silver medium depends on the refractive index of the hole.

Figures 5 and 6 show the transmission efficiency (η) of a dielectric-filled hole in a metal film, versus thickness of the film, with different refractive indexes of the hole (n_c) when the hole radius r = 25nm and r = 50nm, respectively. The transmission efficiency is defined herein as a ratio of the transmitted power behind the aperture (hole) and the incident power at the entrance of the aperture. The incident and the transmitted power are computed from the z component of the incident and the transmitted time-averaged Poynting vectors, respectively, with the difference that the incident power is integrated over the aperture entrance while the transmitted power is integrated over the geometrical exit of the aperture. We observe that when r = 25nm, the high index dielectric filling enhances the transmission efficiency over two orders of magnitude. In the case of r = 50nm, the enhancement is in order of 30. It is also found, as expected, that the transmission efficiency is maximized when the imaginary part of β of the HE_{11} mode exhibits its minimum value. Further, when the refractive indexes of the dielectric filling provide high transmission efficiency, the transmission efficiency exhibit Fabry-Pérot-like behaviour (versus film thickness), similar to the case of two-dimensional metallic slits [13] under TM polarized illumination. That is, the transmission maxima and

#7948 - $15.00 USD Received 27 June 2005; revised 29 July 2005; accepted 25 August 2005

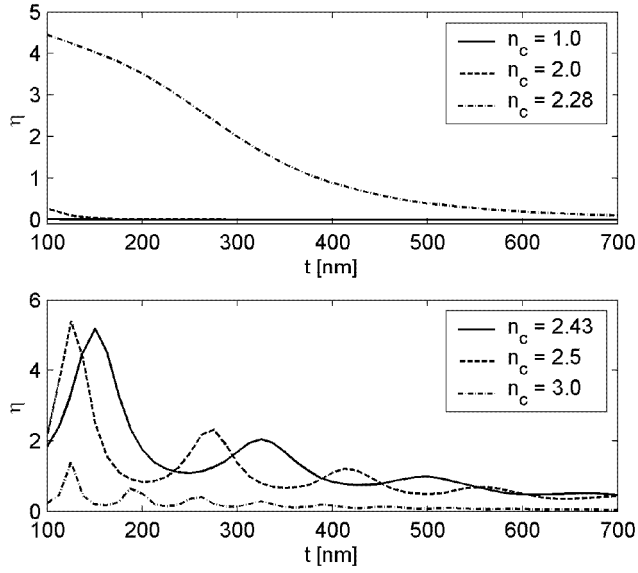

Fig. 5. Transmission efficiency (η) of a dielectric hole in a silver film versus thickness t of the film. The silver film is illuminated by a normally incident, linearly polarized plane wave. The medium within the hole has refractive index n_c and the hole's radius r = 25nm.

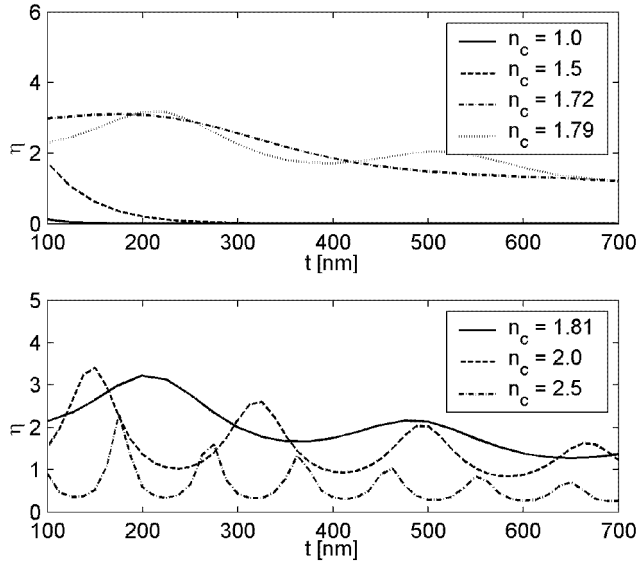

Fig. 6. Same as Fig. 5 but with r = 50nm.

minima appear periodically *versus* film thickness t, with a thickness period of π/β_{re}, where β_{re} is the real part of the propagation constant of the guided HE_{11} mode.

We have also investigated cases in which the incident and the exit media are identical to that dielectric medium which fill the hole, i.e., $n_0 = n_1 = n_c$ (see Fig. 1). We observed that the

#7948 - $15.00 USD Received 27 June 2005; revised 29 July 2005; accepted 25 August 2005

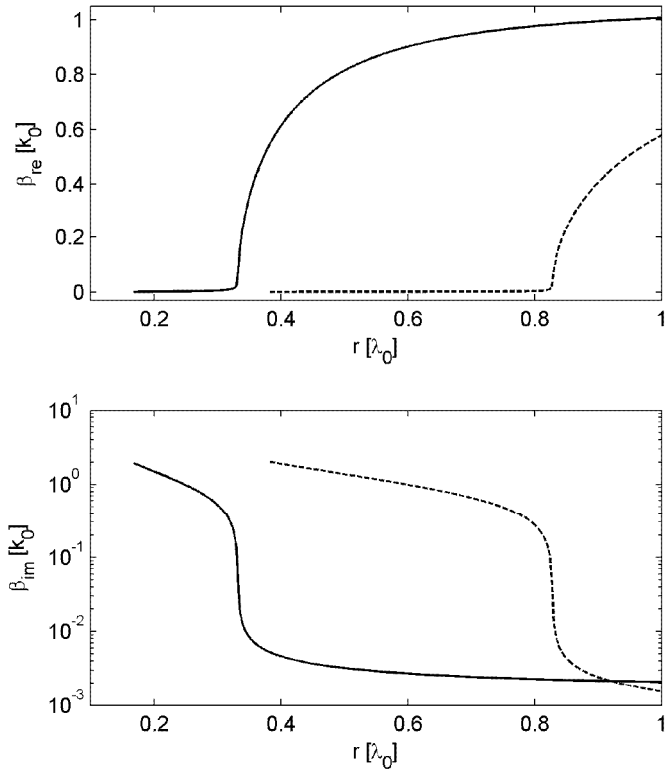

Fig. 7. Complex propagation constant ($\beta = \beta_{re} + j\beta_{im}$) of guided TM_{0n} modes (n = 1: solid line, n = 2: dashed line) as a function of the hole radius (r) for an infinitely long air-filled hole in a silver medium. λ_0 = 488nm, $k_0 = 2\pi/\lambda_0$.

transmission efficiency reduces significantly and also the η *versus* thickness curve is less modulated. This implies that the reflecting entrance and exit interfaces of the dielectric-filled hole form a Fabry-Pérot resonator, which additionally boosts light transmission through the hole. The fact that light propagates several round-trips in the resonator magnifies the importance of the small imaginary part of the propagation constant.

Finally, we shall consider characteristic properties of the TM_{0n} modes. When a circular aperture is illuminated by a radially polarized beam, for example by a Bessel beam, that is focused on the central point of the aperture, the incident field can excite the TM_{0n} ($n \geq 1$) mode of a cylindrical metallic waveguide. Figure 7 shows the complex propagation constant of the TM_{01} and TM_{02} modes as a function of hole radius for an air-filled hole in an infinitely thick silver medium at the wavelength of 488nm. We note that when $r \leq \lambda_0$, the hole does not support any other TM_{0n} modes. It is seen that the effective cutoff radius is $0.33\lambda_0$ for the TM_{01} mode and $0.83\lambda_0$ for the TM_{02} mode, which are significantly larger than the cutoff radii of the corresponding HE_{1n} modes. The physical explanation for this may be as follows: Under a radially polarized illumination, the surface charges generated by the incident field are in the same phase over the entire contour of the aperture edge, whereas under a linearly polarized illumination, the surface charges are in opposite phases at opposite sides of the aperture. Since the electric field can span directly only from a positive charge to a negative charge, it may explain why the HE_{1n} modes exhibit smaller cutoff radii than the TM_{0n} modes. This also

#7948 - $15.00 USD Received 27 June 2005; revised 29 July 2005; accepted 25 August 2005

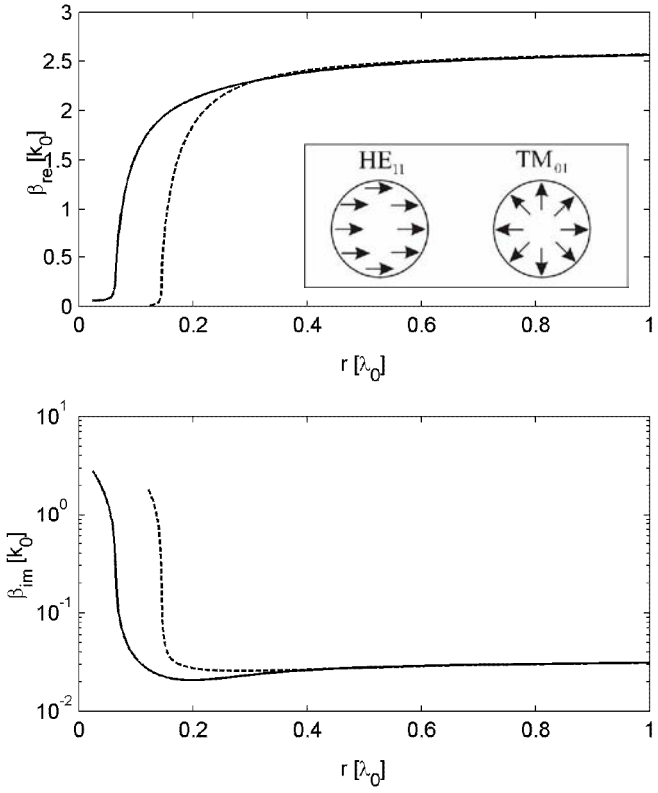

Fig. 8. Comparison between the complex propagation constants ($\beta = \beta_{re} + j\beta_{im}$) of guided HE_{11} (solid line) and TM_{01} (dashed line) modes as a function of the hole radius (r) for a dielectric-filled hole ($n_c = 2$) in an silver medium. The inset illustrates the electric field distributions of HE_{11} and TM_{01} modes.

indicates that the TM_{01} mode can never have a zero cutoff radius. Figure 8 shows a comparison between the propagation constants of the TM_{01} and HE_{11} modes when the refractive index of the hole is 2.0. Also in this case, the HE_{11} mode exhibits a smaller cutoff radius than the TM_{01} mode.

4. Summary and conclusion

In this paper, we have shown that the propagation characteristics of sub-wavelength holes in metal films illuminated by a normally incident, linearly polarized plane wave can be predicted by investigating the complex propagation constants of the hybrid HE_{11} mode. We observed that light transmission through sub-wavelength holes can be remarkably enhanced by filling the hole with a high index dielectric medium. The high-index dielectric filling enables the formation of a guided HE_{11} mode which has a relatively small β_{im}. Further, it creates a Fabry-Pérot-like resonator which provides additional improvement of light transmission through the hole. The fact that light propagates several round-trips in the resonator magnifies the importance of the small imaginary part of the propagation constant.

This study provides results only for one incident wavelength ($\lambda_0 = 488$nm), but the idea of high index dielectric filling is also valid at longer wavelengths. For example, crystalline silicon, which has the refractive index of 3.8+0.016j@650nm [15], could be used as a filler

#7948 - $15.00 USD Received 27 June 2005; revised 29 July 2005; accepted 25 August 2005

for cylindrical 40nm diameter holes in a Ag medium. A structure, which has even higher transmission efficiency, can be constructed by combining the idea of a high index dielectric filling with circular surface corrugations that surrounds the central hole. This will be considered in detail in our forthcoming paper.

#7948 - $15.00 USD Received 27 June 2005; revised 29 July 2005; accepted 25 August 2005

PAPER II

Light transmission through a high index dielectric hole in a metal film surrounded by surface corrugations

In: Optics Express 2006.
Vol. 14, No. 24, pp. 11506–11511.

Light transmission through a high index dielectric hole in a metal film surrounded by surface corrugations

Juuso Olkkonen and Kari Kataja

VTT Technical Research Centre of Finland, Kaitovayla 1, P.O. Box 1100, FIN-90571 Oulu, Finland

Juuso.Olkkonen@vtt.fi

Dennis G. Howe

University of Arizona, Optical Sciences Center, Tucson, AZ 85721-0094, USA

Abstract: We analyze transmission of a normally incident plane wave through a 100nm diameter hole in a silver film that is filled with a high index dielectric and is surrounded by 300nm wide surface grooves. Specifically, we study the dependency of the transmission efficiency on the number of grooves, groove depth, and the horizontal distance between the groove and the central hole. We observe that the investigated structure exhibits over five orders of magnitude larger transmission efficiency versus a single hole without the dielectric filling.

OCIS codes: (050.1220) Apertures; (050.1940) Diffraction

References and links

1. D. E. Grupp, H. J. Lezec, T. Thio, and T. W. Ebbesen, "Beyond the Bethe Limit: Tunable Enhanced Light Transmission Through a Single Sub-Wavelength Aperture," Adv. Mater. **11**, 860–862 (1999).
2. T. Thio, K. M. Pellerin, R. A. Linke, H. J. Lezec, and T. W. Ebbesen, "Enhanced light transmission through a single subwavelength aperture," Opt. Lett. **26**, 1972–4 (2001).
3. T. Thio, H. J. Lezec, T. W. Ebbesen, K. M. Pellerin, G. D. Lewen, A. Nahata A, and R. A. Linke, "Giant optical transmission of sub-wavelength apertures: Physics and applications," Nanotechnology **13**, 429-432 (2002).
4. A. Degiron A and T. W. Ebbesen, "Analysis of the transmission process through single apertures surrounded by periodic corrugations," Opt. Express **12**, 3694-3700 (2004).
5. H. J. Lezec, and T. Thio, "Diffracted evanescent wave model for enhanced and suppressed optical transmission through subwavelength hole arrays," Opt. Express **12**, 3629-3651 (2004).
6. H. F. Ghaemi, T. Thio, D. E. Grupp, T. W. Ebbesen, and H. J. Lezec, "Surface plasmons enhance optical transmission through subwavelength holes," Phys. Rev. B **58**, 6779-82 (1998).
7. A. R. Zakharian, M. Mansuripur, J. V. Moloney, "Transmission of light through small elliptical apertures," Opt. Express **12**, 2631-2648 (2004).
8. J. Olkkonen, K. Kataja, and D. Howe, "Light transmission through a high index dielectric-filled sub-wavelength hole in a metal film," Opt. Express **13**, 6980-6989 (2005).
9. P. B. Johnson and R. W. Christy, "Optical Constants of the Noble Metals," Phys. Rev. B **6**, 4370-4379 (1972).
10. K. Okamoto, Fundamentals of Optical Waveguides (Academic Press, San Diego, 2000).
11. J. Takahara, and T. Kobayashi, "Nano-optical waveguides breaking through diffraction limit of light," in *Optomechatronic Micro/Nano Components, Devices, and Systems*, Y. Katagiri, eds., Proc. SPIE **5604**, 158-172 (2004).
12. A. Taflove and S. C. Hagness, Computational Electrodynamics: The Finite Difference Time Domain Method (Second Edition, Artech House, Boston, 2000).
13. Y. Takakura, "Optical resonance in a narrow slit in a thick metallic screen," Phys. Rev. Lett. **86**, 5601-5603 (2001).
14. Y. Xie, A. Zakharian, J. Moloney, and M. Mansuripur, "Transmission of light through slit apertures in metallic films," Opt. Express **12**, 6106-6121 (2004).

#75564 - $15.00 USD Received 28 September 2006; revised 1 November 2006; accepted 1 November 2006

1. Introduction

The exploitation of sub-wavelength apertures in opaque films for light confinement into the sub-wavelength domain has been limited due to the negligible transmission efficiency of very small apertures. It has been recently noted [1-5], however, that cylindrical surface corrugations around a single, central, sub-wavelength-sized hole in a metal film can greatly enhance the otherwise weak transmission through the hole. This enhanced transmission is widely attributed to the influence of surface plasmon polaritons (SPPs) excited by the surface corrugations [1,2,3,4,6]. This effect can be explained also in terms of the diffracted evanescent wave model, proposed by Lezec et al. [5], in which the surface waves excited by the surface corrugations interfere with the incident plane wave that directly impinges on the aperture. According to this latter model, the phase difference between the incident plane wave and the surface waves determines the transmission maxima and minima.

Zakharian et al. [7] have developed an intuitive description governing light transmission through elliptical apertures in planar metal films. They concluded that achieving large transmission efficiency requires an aperture structure that can excite strong oscillator(s) on the upper surface of the metal film, which would then induce strong oscillations on the lower film surface in the neighborhood of the aperture. They also noted that the ability of a hole to support a guided mode, that can be excited by the incident polarization, appears to be critical for achieving large transmission, especially for thicker films. The latter observation agrees with results of our previous paper [8], where we reported that that by filling a sub-wavelength, cylindrical hole with a high index dielectric medium, the transmission efficiency of the hole can be increased over two orders of magnitude. We observed that the high index dielectric filling: (1) enables formation of the hybrid HE_{11} waveguide mode exhibiting a complex propagation constant, the imaginary part of which is relatively small; (2) transforms the hole into a Fabry-Pérot resonator, additionally boosting the light transmission through the sub-wavelength hole. To our best knowledge, this paper investigates for the first time a novel structure that combines high index dielectric aperture filling and concentric periodic surface corrugations around the aperture.

This paper is organized as follows. First, we analytically study the propagation constant (β) of guided modes that are supported by an infinitely long cylindrical, dielectric-filled hole in a silver medium. Then we study transmission properties of a sub-wavelength aperture, 50nm in radius, in a thick metal film versus the thickness of the metal film and the refractive index of the aperture. Finally, the influence of surface grooves on transmission efficiency is investigated in detail.

2. Light transmission through a single cylindrical aperture in a planar silver film

Throughout this paper, we consider a cylindrical sub-wavelength aperture, 50nm in radius, in a silver film ($n_{Ag} = 0.055 + 4.44i$ [9]) that is illuminated by a normally incident, linearly polarized plane wave having free space wavelength (λ_0) of 650nm. First, we shall consider a cylindrical aperture that has infinite length along its axis (propagation direction of the incident wave). Such an aperture, which can be considered as a cylindrical waveguide having a silver cladding, can be characterized by examining the complex propagation constant ($\beta = \beta_{re} + \beta_{re}i$) of the hybrid HE_{11} waveguide mode [9]. Figure 1 shows β of the HE_{11} mode for the aforementioned cylindrical waveguide as a function of the refractive index of the waveguide core (n_c). Interestingly, the imaginary part of β starts to strongly decrease, while the real part exhibits a simultaneous increase, when $n_c > 2.2$. The imaginary part attains its minimum when $n_c = 2.77$, after which it starts to slowly increase. These results are obtained via standard waveguide theories with no weak guiding assumption [10,11].

Figure 2 shows the transmission efficiency (η) of a normally incident plane wave through a

#75564 - $15.00 USD Received 28 September 2006; revised 1 November 2006; accepted 1 November 2006

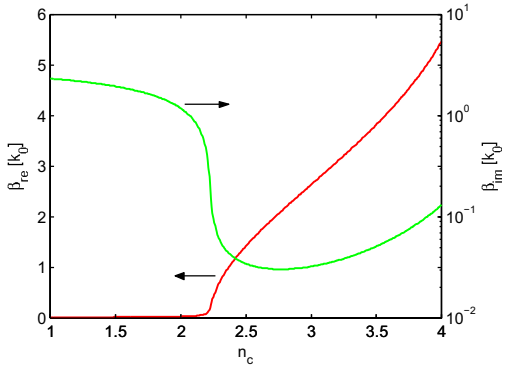

Fig. 1. Complex propagation constant ($\beta = \beta_{\mathrm{re}} + \beta_{\mathrm{im}} i$) of the HE_{11} mode as a function of the refractive index of the waveguide core (n_C) for an infinitely long cylindrical waveguide having a silver cladding and a core radius of 50nm. $k_0 = 2\pi/\lambda_0$, λ_0 = 650nm, and n_{Ag} = 0.055 + 4.44i.

50nm radius cylindrical hole in a free standing silver film as a function of the Ag-film thickness (t) for three different refractive indexes (n_C) of the hole: n_C = 1.0 (solid line), n_C = 2.4 (dashed line), n_C = 2.8 (dashed-dotted line). We consider only completely opaque silver films, i.e., t $\geq$ 100nm. The transmission efficiency is computed throughout this paper as a ratio of the total power emanating from the geometrical exit (lower film surface) aperture of the hole and the incident power falling into the geometrical entrance (upper film surface) aperture of the hole. The results are obtained via the BOR-FDTD method [12], in which the Yee cell size is chosen to be 2.5nm both in the radial and in the longitudinal z direction. The computation domain is terminated by uniaxial perfectly matched layers (UPML) [12], which provide highly absorbing boundary conditions. We observe that by filling the hole by a high index medium, η can be enhanced over a factor of 500. It is also seen that η exhibits a clear Fabry-Pérot kind of

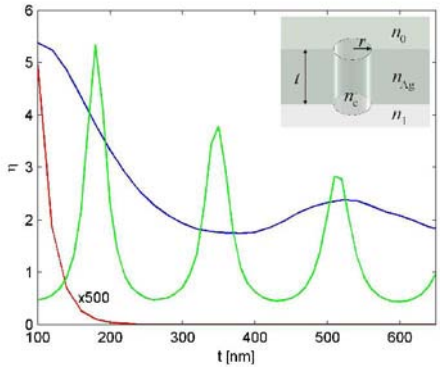

Fig. 2. Transmission efficiency (η) of a normally incident linearly polarized plane wave through a sub-wavelength (r = 50nm), cylindrical dielectric hole in a silver film as a function of the film thickness (t) for different refractive indexes of the hole: n_C = 1.0 (red line), n_C = 2.4 (blue), n_C = 2.8 (green). The refractive indexes of the incident and the exit medium are denoted by n_0 and n_1, respectively. n_0 = n_1 = 1.0, n_{Ag} = 0.055 + 4.44i, λ_0 = 650nm. The solid line is magnified by a factor of 500.

#75564 - $15.00 USD Received 28 September 2006; revised 1 November 2006; accepted 1 November 2006

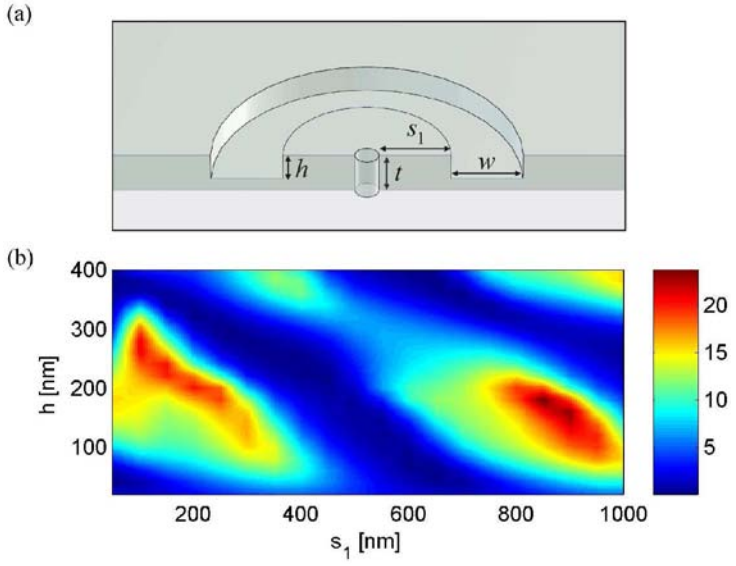

Fig. 3. (a) Cross-section of the modeled structure: A sub-wavelength hole (r = 50nm) in a silver film (t = 515nm) that is filled by a high index dielectric medium (n_C = 2.8) is surrounded by a single groove having depth h and width w. (b) Transmission efficiency (η) of a normally incident, linearly polarized plane wave through the sub-wavelength hole shown in (a) as a function of the groove depth (h) and the distance (s_1) between the central hole and the groove. In all cases, w = 300nm, λ_0 = 650nm, and $n_{Ag} = 0.055 + 4.44i$.

behavior; transmission maxima and minima appear periodically with thickness period of π/β_{re}. A similar behavior has been observed also for single slits in metal films [13,14].

3. Light transmission through a single aperture in a corrugated silver film

We are now in a position to explore transmission properties of a single, high index, sub-wavelength (n_C = 2.8, r = 50nm) hole in a thick silver film surrounded by concentric circular grooves. First, we study the influence of a single circular surface groove on transmission efficiency as a function of the groove depth (h) and distance from the central hole (s_1), see Fig. 3(a). To investigate relatively deep grooves with no light leakage through them, we consider a 515nm thick silver film. This thickness also provides resonant transmission trough the aperture according the results of Fig. 2. The groove width (w) is a fixed parameter, having value of 300nm, which is a common value used in recent experiments [4, 5]. Figure 3(b) shows the transmission efficiency (η) for a central hole that is surrounded by a single circular groove as a function of s_1 and h. Figure 3(b) is obtained by linearly interpolating the results of simulations in which s_1 is varied from 50 to 1000nm in 50nm steps and h is varied from 20 to 400nm in 20nm steps. Clearly, transmission efficiency depends periodically both on s_1 and h. The periodic dependency on s_1 is due to the phase difference (at the entrance of the central hole) between the incident plane wave and the surface wave excited by the concentric circular groove. This result is in accordance with the predictions of the diffracted evanescent wave model [5]. The periodic dependency on h is due to interference occurring within the groove. The maximum transmission efficiency also increases as a function of s_1. This is due to fact that the length of the groove's circular contour, which excites surface waves, increases linearly with

#75564 - $15.00 USD Received 28 September 2006; revised 1 November 2006; accepted 1 November 2006

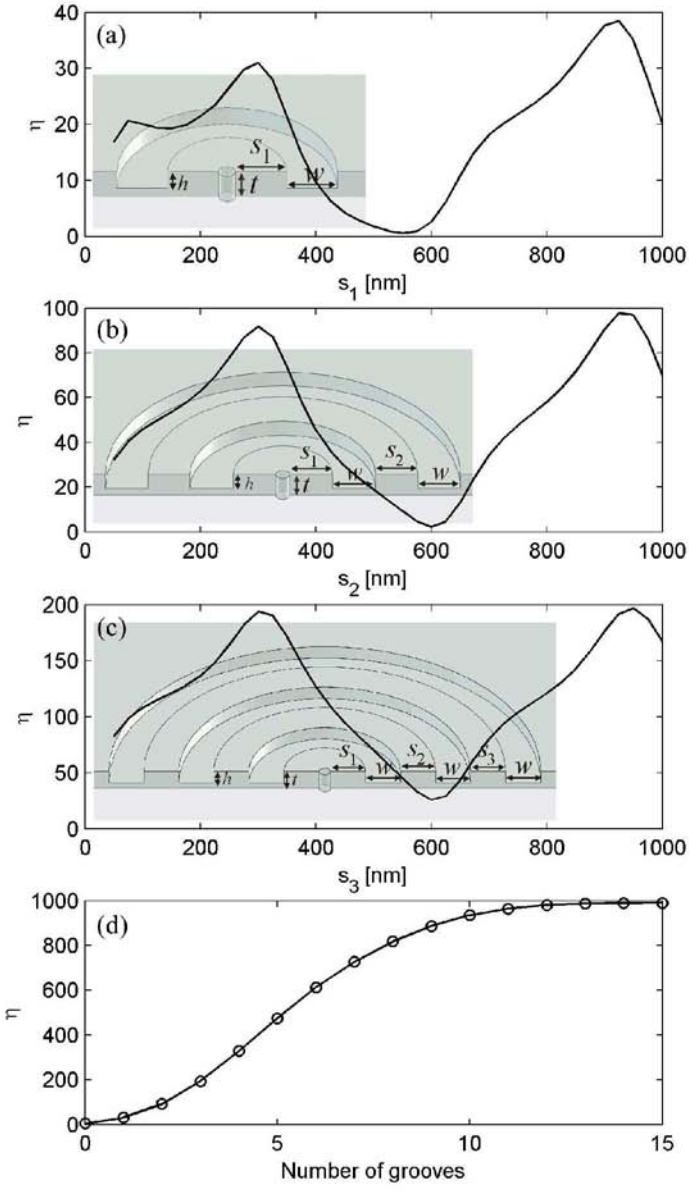

Fig. 4. Transmission efficiency (η) of a normally incident, linearly polarized plane wave through a sub-wavelength hole (r = 50nm, n_c = 2.8) in a free standing silver film (t = 180nm) when the central hole is surrounded by (a) a single groove, (b) two grooves (s_1 = 300nm), and (c) three grooves ($s_1 = s_2$ = 300nm). (d) Transmission efficiency as a function of the number of grooves when the radial distance (s_n) between the adjacent grooves is 300nm. In all cases, w = 300nm, h = 120nm, λ_0 = 650nm, and $n_{Ag} = 0.055+4.44i$.

#75564 - $15.00 USD Received 28 September 2006; revised 1 November 2006; accepted 1 November 2006

s_1. However, when the groove is far enough from the central hole, the transmission efficiency starts to decrease due to attenuation of the surface waves.

Figures 4(a)-(c) show results for the cases where the central hole is surrounded first by a single groove and then by two and three grooves. The metal film is now 180nm thick and groove is 120nm deep and 300nm wide. When s_1 = 550nm in Fig. 4(a), light transmission through the central hole is almost zero. This is due to the fact that approximately equal power, with opposite phases, couples from the incident plane wave and the surface wave into the central hole, resulting in nearly zero transmission. In Figure 4(b), the distance between the first groove and the central hole (s_1) is set to 300nm, which is the location of the first maximum in Fig. 4(a). It is seen that the transmission efficiency exhibits increased maxima and that the locations of the maxima and minima depend on the distance between the first and the second groove (s_2). This occurs due to the same physical phenomena observed in the single groove case. The first maximum appears in Fig. 4(b) at s_2 = 300nm, which is used as a distance between the first and the second groove in Fig. 4(c). Figure 4(d) shows how the transmission efficiency depends on the number of grooves (n) when the radial distance between the adjacent grooves is 300nm. The transmission efficiency increases until n = 13 when η is about five orders of magnitude higher than η of a single aperture without the dielectric filling.

4. Summary and conclusion

This paper investigated for the first time transmission of a normally incident, linearly polarized plane wave through a high index dielectric-filled hole surrounded by surface corrugations. The dependency of transmission efficiency on a single 300nm wide groove was studied versus the groove depth and its distance from the central hole. It was observed that the phase difference between the incident plane wave and the surface waves determines the occurrence of transmission maxima and minima. A similar behavior was also observed with several grooves. When the central hole is surrounded by 13 grooves, the transmission efficiency is increased by five orders of magnitude compared to a single aperture without the dielectric filling.

#75564 - $15.00 USD Received 28 September 2006; revised 1 November 2006; accepted 1 November 2006

PAPER III

Light trapping cavity enhanced light transmission through a single sub-wavelength aperture in a metal film

In: Optics Express 2009.
Vol. 17, No. 26, pp. 23992–24001.

Light trapping cavity enhanced light transmission through a single sub-wavelength aperture in a metal film

Juuso Olkkonen*

VTT Technical Research Centre of Finland,Tietotie 3, P.O. Box 1000, 02044 VTT, Finland
**juuso.olkkonen@vtt.fi*

Abstract: We demonstrate that optical transmission of a normally incident, monochromatic plane wave through a single sub-wavelength aperture in an opaque metal film can be substantially enhanced by a thin, semitransparent metal film placed parallel to the opaque metal film in front of the aperture. When the semi-transparent and the opaque metal film are separated by a proper distance, a light trapping cavity is formed and the sub-wavelength aperture exhibits a transmission maximum. An enhancement factor of ~40 is demonstrated for a cylindrical 100 nm diameter hole in a silver film.

OCIS codes: (050.1220) Apertures; (240.0240) Optics at surfaces.

References and links

1. T. W. Ebbesen, H. J. Lezec, H. F. Ghaemi, T. Thio, and P. A. Wolff, "Extraordinary optical transmission through sub-wavelength hole arrays," Nature **391**(6668), 667–669 (1998).
2. D. E. Grupp, H. J. Lezec, T. Thio, and T. W. Ebbesen, "Beyond the Bethe Limit: Tunable Enhanced Light Transmission Through a Single Sub-Wavelength Aperture," Adv. Mater. **11**(10), 860–862 (1999).
3. T. Thio, K. M. Pellerin, R. A. Linke, H. J. Lezec, and T. W. Ebbesen, "Enhanced light transmission through a single subwavelength aperture," Opt. Lett. **26**(24), 1972–1974 (2001).
4. T. Thio, H. J. Lezec, T. W. Ebbesen, K. M. Pellerin, G. D. Lewen, A. Nahata, and R. A. Linke, "Giant optical transmission of sub-wavelength apertures: Physics and applications," Nanotechnology **13**(3), 429–432 (2002).
5. F. J. García-Vidal, H. J. Lezec, T. W. Ebbesen, and L. Martín-Moreno, "Multiple paths to enhance optical transmission through a single subwavelength slit," Phys. Rev. Lett. **90**(21), 213901–1 (2003).
6. D. A. Thomas, and H. P. Hughes, "Enhanced optical transmission through a subwavelength 1D aperture," Solid State Commun. **129**(8), 519–524 (2004).
7. H. F. Ghaemi, T. Thio, D. E. Grupp, T. W. Ebbesen, and H. J. Lezec, "Surface plasmons enhance optical transmission through subwavelength holes," Phys. Rev. B Condens. Matter **58**(11), 6779–6782 (1998).
8. H. J. Lezec, and T. Thio, "Diffracted evanescent wave model for enhanced and suppressed optical transmission through subwavelength hole arrays," Opt. Express **12**(16), 3629–3651 (2004), http://www.opticsinfobase.org/oe/abstract.cfm?URI=oe-12-16-3629.
9. F. Wu, D. Han, X. Li, X. Liu, and J. Zi, "Enhanced transmission mediated by guided resonances in metallic gratings coated with dielectric layers," Opt. Express **16**(9), 6619–6624 (2008), http://www.opticsinfobase.org/oe/abstract.cfm?URI=oe-16-9-6619.
10. J. A. Kong, ***Electromagnetic Wave Theory*** (EMW Publishing, 2000).
11. K. S. Yee, "Numerical solution of initial boundary value problems involving Maxwell's equations in isotropic media," IEEE Trans. Antenn. Propag. **14**(3), 302–307 (1966).
12. A. Taflove, and S. C. Hagness, ***Computational Electrodynamics: The Finite-Difference Time-Domain Method*** (Second Edition, Artech House, INC., 2000).
13. S. D. Gedney, "An anisotropic perfectly matched layer-absorbing medium for the truncation of FDTD lattices," IEEE Trans. Antenn. Propag. **44**(12), 1630–1639 (1996).
14. M. Okoniewski, M. Mrozowski, and M. A. Stuchly, "Simple treatment of multi-term dispersion in FDTD," IEEE Microw. Guid. Wave Lett. **7**(5), 121–123 (1997).
15. P. B. Johnson, and R. W. Christy, "Optical constants of the noble metals," Phys. Rev., B, Solid State **6**(12), 4370–4379 (1972).
16. J. Olkkonen, K. Kataja, and D. Howe, "Light transmission through a high index dielectric-filled sub-wavelength hole in a metal film," Opt. Express **13**(18), 6980–6989 (2005), http://www.opticsinfobase.org/oe/abstract.cfm?URI=oe-13-18-6980.

#118380 - $15.00 USD Received 9 Oct 2009; revised 25 Nov 2009; accepted 2 Dec 2009; published 16 Dec 2009

1. Introduction

Optical light transmission through sub-wavelength slits and apertures in metal films has gained great interest since the discovery of extraordinary light transmission through arrays of sub-wavelength holes by Ebbesen ***et al.*** [1]. Later, it was observed that enhanced transmission can also occur in single apertures [2–4] and slits [5,6] that are surrounded by periodic surface corrugations. García-Vidal ***et al.*** [5] associated the transmission enhancement in corrugated structures to groove cavity mode excitation, in-phase groove reemission, and slit waveguide mode. Also surface plasmon polaritons (SPPs) excited by the surface corrugations are seen to have a significant role in the transmission process [2–4,7]. Lezec ***et al.*** [8] have introduced the so called diffracted evanescent wave model, which explains the enhanced transmission as being due to interference between the normally incident plane wave and diffracted surface waves generated by the periodic surface corrugations. F. Wu ***et al.*** [9] have studied a metallic grating structure that is coated symmetrically with a dielectric layer on both sides. Besides cavity resonances in slits and SPPs, they have found that guided resonances in the dielectric layers provide another mechanism for enhanced transmission.

In this paper, we introduce a completely new way to enhance transmission of a normally incident, monochromatic plane wave through a sub-wavelength aperture in a metal film. It is based on the Fabry-Pérot resonance between two parallel metal films from which the first is semi-transparent and the second opaque. By properly selecting the thickness of the semitransparent film and the gap between the films, light gets trapped to the space between the metal films and the electric field is substantially increased in the gap region. That is, the structure works as a light trapping cavity. We demonstrate that a sub-wavelength aperture formed into the opaque metal film of the light trapping structure exhibits much higher transmittance than the same aperture in a bare opaque metal film. This new transmission enhancement mechanism works also with the transverse electric (TE) polarized light, in contrary to the surface wave -based mechanisms.

The paper is organized as follows. Section 2 introduces the numerical modeling methods used in the study. The optimal structure for the light trapping cavity is found in Section 3. In Section 4, we study light transmission through an ordinary sub-wavelength slit in a metal film. The effect of the light trapping cavity on light transmission through a slit is studied in Section 5 and through a cylindrical aperture in Section 6. The summary and conclusions are presented in Section 7.

2. Numerical models

Optical structures studied in this work are illustrated in Fig. 1. Enhanced optical transmission of a monochromatic, normally incident plane wave through a sub-wavelength slit or a cylindrical hole in an opaque silver film is obtained by placing a semi-transparent silver film in front of the opaque metal film. The opaque metal film and the semitransparent metal film form a light trapping cavity. The operation principle of the structure is described more precisely in the next section. The free space wavelength of incident light (λ_0) was assumed to be 650 nm throughout the entire study. To obtain efficient transmission of the TE polarized light, the sub-wavelength slit was filled by a high index dielectric medium. For details, see Sect. 4. In the TM case, the dielectric filling was not observed to provide any transmission enhancement and thus an empty slit was used under TM polarized illumination. The cylindrical hole shown in Fig. 1(b) was always filled with a high index dielectric medium.

#118380 - $15.00 USD Received 9 Oct 2009; revised 25 Nov 2009; accepted 2 Dec 2009; published 16 Dec 2009

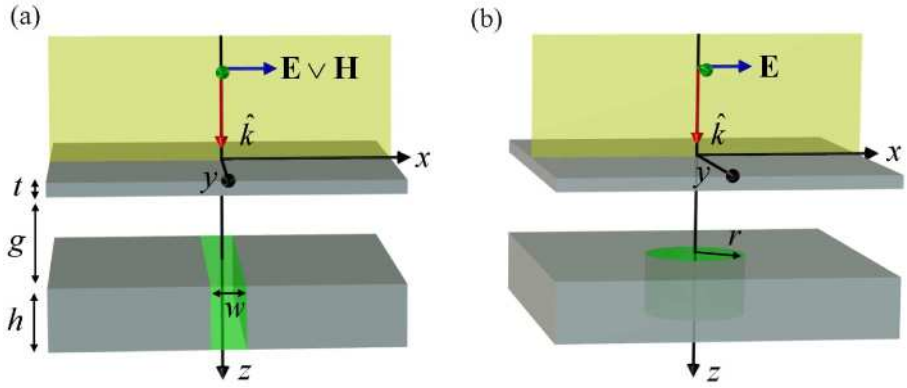

Fig. 1. Illustration of the modeled structures. (a) A sub-wavelength slit in an opaque metal film is illuminated by a normally incident TE or TM polarized plane wave through a semitransparent metal film. The thickness of the semitransparent metal film (***t***) and the gap between the opaque and the semitransparent film (***g***) are selected so that the films form a light trapping cavity. When the incident light is TE polarized (electric field perpendicular to the plane of incidence), the slit is filled with a high index dielectric medium. In the TM case, the slit is always empty. The both metal films in the ***x***- and ***y***-directions extend to infinity. The yellow plane illustrates the plane of incidence. (b) The same as (a) but now the slit is replaced by a sub-wavelength cylindrical hole filled with a high index dielectric medium.

The thickness of the semitransparent metal film and the distance from the opaque metal film in the absence of the aperture structure was optimized using the analytical multi-layer calculation method [10]. Light transmission through the slit structure was modeled by the two-dimensional finite difference time domain (FDTD) method [11,12]. The Yee cell size was 2.5 nm both in the transverse and the longitudinal direction. The computation domain was terminated by the perfectly matched layer (PML) absorbing boundary condition [13]. The simulations results presented for the cylindrical hole were obtained with the body of revolution finite difference time domain (BOR-FDTD) method [12]. The Yee cell size both in the ***z*** and in the radial direction was 2.5 nm.

The optical response of silver was included into the FDTD models via the Lorentz model that was implemented using the auxiliary differential equation [14]. Parameters of the Lorentz model were optimized so that refractive index of silver matches with the experimental data presented by Johnson ***et al***. [15]. The used Lorentz model for silver produced refractive index of 0.054 + 4.41***i*** at the free space wavelength of 650 nm.

3. Light trapping multilayer cavity

Using a semitransparent and an opaque metal film, which are parallel to each other and separated by a proper distance, it is possible to form a multilayer structure that absorbs nearly all incident monochromatic light at a particular angle of incidence. Such a structure is illustrated in Fig. 2(d), in which ***t***, ***g***, and ***h*** denote the thickness of the semitransparent silver film, the gap between the silver films, and the thickness of the opaque silver film, respectively. Figure 2(a) shows the reflectance of a normally incident plane having free space wavelength (λ_0) of 650 nm from the free standing structure ($\boldsymbol{n}_0$ = 1.0) as a function of ***t*** and ***g*** for a fixed value ***h*** = 200 nm. (At visible frequencies, a silver film is practically opaque when its thickness is greater than 100 nm.) It is seen, especially from Fig. 2(b), that nearly all light is trapped into the structure when ***t*** = 40 nm and ***g*** = 277.5 nm. When ***t*** = 40 nm and ***h*** = 200 nm, the light trapping occurs always when ***g*** = 277.5 nm + $\boldsymbol{m}\cdot\lambda_0/2$, where ***m*** is a positive integer. This periodicity is clearly observable in Fig. 2(a). Due to the opaque silver film, light transmission through the structure is always zero for all values of ***g*** and ***t***.

#118380 - $15.00 USD Received 9 Oct 2009; revised 25 Nov 2009; accepted 2 Dec 2009; published 16 Dec 2009

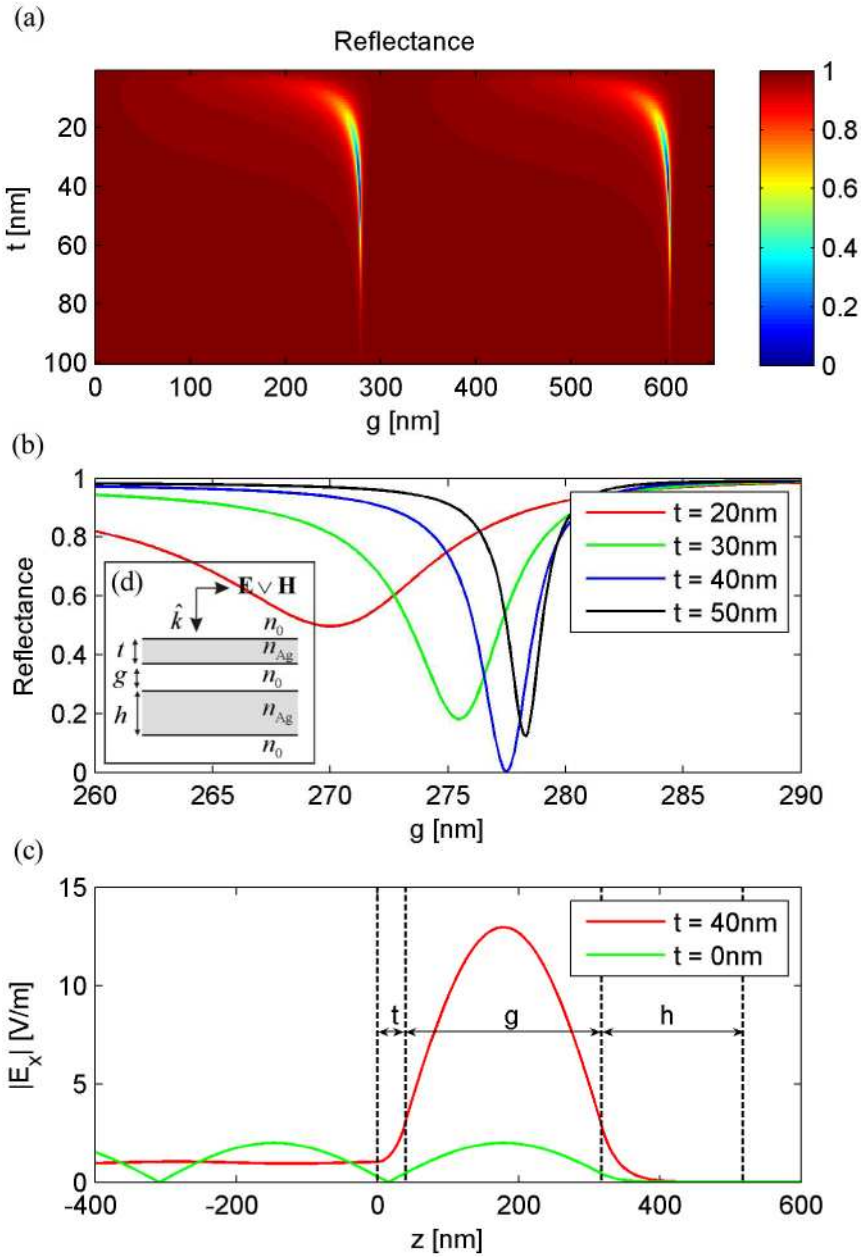

Fig. 2. (a) Reflectance of a normally incident plane wave (E_x, $E_z \equiv 0$, H_y) having wavelength of 650 nm from the multilayer structure shown in the inset (d) as a function of ***t*** and ***g***. The uppermost silver film is semitransparent (***t*** = 0-100 nm) while the second is opaque (***h*** = 200 nm), i.e., the transmittance through the entire structure is zero for all values of ***g*** and ***t***. $\boldsymbol{n}_0$ = 1.0. (b) Cross profiles of the reflectance map shown in (a) for ***t*** = 20, 30, 40, and 50 nm. (c) Electric field amplitude in the multilayer structure shown in (d) (***g*** = 277.5 nm, ***h*** = 200 nm) without (***t*** = 0 nm) and with the semitransparent metal film (***t*** = 40 nm).

Figure 2(c) shows the electric field amplitude in the light trapping structure in two cases: (a) ***t*** = 40 nm, (b) ***t*** = 0 nm, i.e., in the presence and absence of the 40 nm thick semitransparent silver film. In the first case, light is trapped into the structure and the electric field amplitude is substantially enhanced in the gap between the metal films, whereas in the second case, practically all the incident light is reflected from the opaque metal film. We note

#118380 - $15.00 USD Received 9 Oct 2009; revised 25 Nov 2009; accepted 2 Dec 2009; published 16 Dec 2009

that in both cases the shape of the electric field amplitude is exactly the same in the gap region and inside the opaque metal film. At resonance, the electric field amplitude is enhanced in these regions by a factor of 6.5 but not altered in shape.

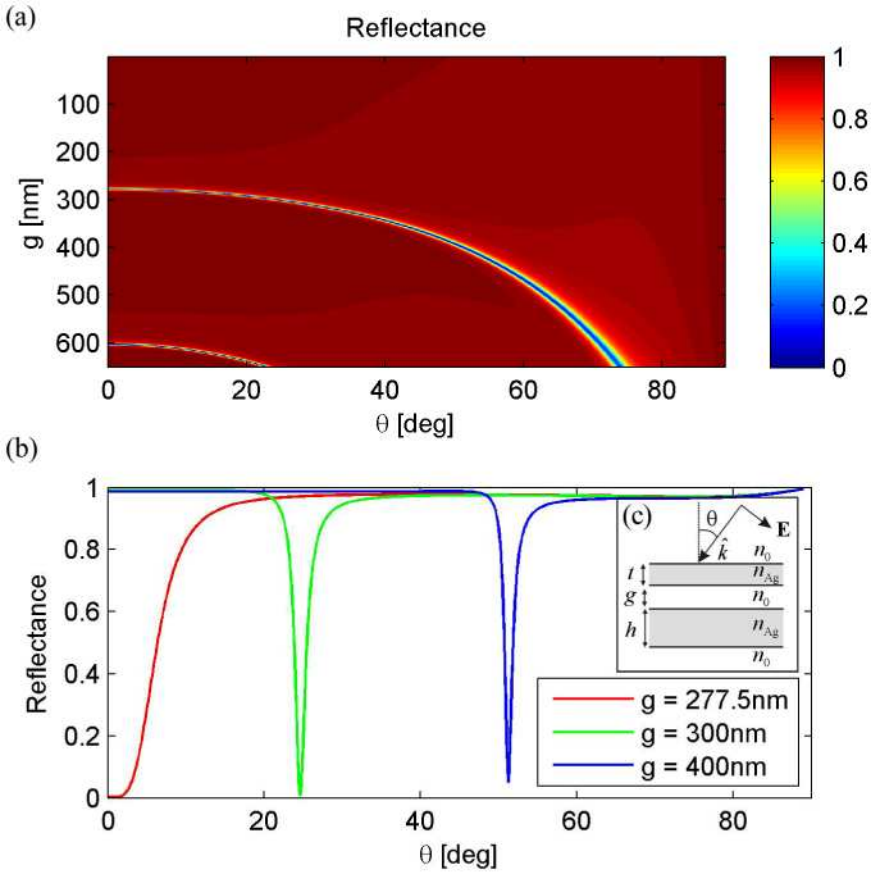

Fig. 3. (a) Reflectance of an obliquely incident, TM polarized plane wave having free space wavelength of 650 nm from the multilayer structure (***t*** = 40 nm, ***h*** = 200 nm, $\boldsymbol{n}_0$ = 1) shown in the inset (c) as a function of the incident angle (θ) and the thickness of the air gap (***g***). (b) Cross profiles of the reflectance map shown in (a) for ***g*** = 277.5, 300, and 400 nm.

As illustrated in Fig. 2, the reflectance of the light trapping structure is very sensitive to the gap thickness (g) between the metal films. Due to this fact, it might be thought that the presented structure is not very practical. The situation, however, can be eased, for example, by assuming that the angle of incidence of the illuminating plane wave is an adjustable parameter. Figure 3 shows the reflectance of the resonance structure (t = 40 nm, h = 200 nm) as a function of the gap and the angle of incidence. It is seen that when the gap is equal or larger than 277.5 nm, we can find an incident angle that satisfies the resonance condition.

4. Light transmission through a slit in a silver film

Before describing light transmission through a sub-wavelength slit in a light trapping multilayer cavity, we shall discuss the basic transmission properties of metallic sub-wavelength slits. We will utilize these results when interpreting results in the forthcoming sections.

#118380 - $15.00 USD Received 9 Oct 2009; revised 25 Nov 2009; accepted 2 Dec 2009; published 16 Dec 2009

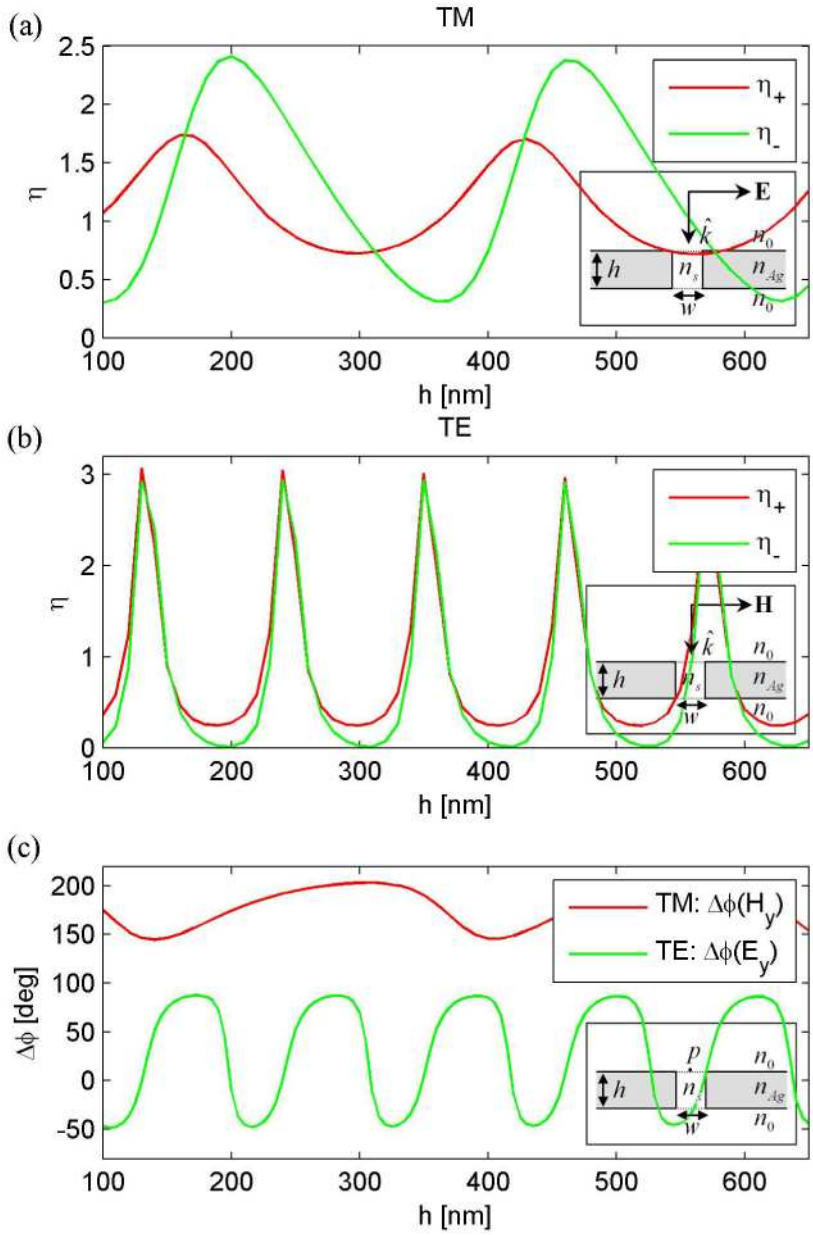

Fig. 4. (a) Normalized transmission (η +) and back-scattering (η-) efficiency as a function of the silver film thickness (h) for a 100 nm wide (w) slit under normally incident TM polarized plane wave illumination (ns = 1.0, n0 = 1.0, λ0 = 650 nm). (b) The same as (a) but now the slit is illuminated by a TE polarized plane wave and the slit is filled by a dielectric medium having refractive index (ns) of 3.8. (c) The dependency of the phase difference between the illuminating plane wave and the scattered field on the slit length in the middle of the slit entrance (point p shown in the inset). In the TM case, the phase difference is calculated from the magnetic field and from the electric field in the TE case.

When light transmission through a slit in a metal film is considered, the slit can be thought as a scatterer that resides in a stratified background structure. The scattered field due to the slit can be obtained by subtracting the field, which would be present if the metal film contained no slit, from the total field of the slit structure. Note that in the region below the metal film, the scattered field is the same as the total field since no incident field penetrate

#118380 - $15.00 USD Received 9 Oct 2009; revised 25 Nov 2009; accepted 2 Dec 2009; published 16 Dec 2009

through the opaque metal film. The scattered field emanates from the slit to the forward (**+ *z***) and backward (**-*z***) directions. Traditionally, the light transmission through the slit is characterized by the normalized transmission efficiency (η_+) that is the ratio of the transmitted power in the geometrical exit of the slit and the incident power at the slit entrance. In this paper, we also examine a parameter that is referred to as the normalized back-scattering efficiency (η_-). This parameter is defined as the ratio of the scattered and incident power at the geometrical entrance of the slit. Figure 4(a) shows the normalized transmission (η_+) and back-scattering (η_-) efficiency as a function of the silver film thickness (***h***) for a 100 nm wide slit under TM polarized plane wave illumination. It is observable from Fig. 4(a) that the normalized transmission efficiency exhibits a clear Fabry-Pérot-like behavior, i.e., η_+ varies periodically with the slit length (***h***). At resonance (e.g. ***h*** = 165 nm), the η_+- and η_--curve cross, i.e., the slit radiates equally much power into + ***z***- and –***z***-directions.

When the slit width (***w***) is smaller than $\lambda_0/2$, only the TM polarized light propagates through the slit. However, the transmittance of the TE polarized light can be substantially enhanced by filling the slit by a high index dielectric medium. The high index filling has two functions in the transmission process: (1) it enables the formation of a guided TE_{01} mode having the propagation constant with a relatively small imaginary part; (2) it forms a Fabry-Pérot-like resonance structure due to reflecting entrance and exit interfaces of the slit. Figure 4(b) shows the η_+ and η_- as a function of the silver film thickness for a 100 nm wide slit under TE polarized illumination. The slit is filled with a medium having refractive index of 3.8. It is seen that efficient light transmission through the 100 nm wide slit is achieved. We note that under TM polarized illumination, the high index filling was not observed to increase the transmission efficiency of a 100 nm wide slit in a silver film.

Figure 4(c) shows how the phase difference between the backward scattered light and illuminating plane wave depends on the slit length in the middle of the slit entrance (point ***p*** in the inset of Fig. 4(c)). Since the TM polarized light contains only one magnetic field component (***H*****$_y$**), and the TE polarized light only one electric field component (***E*****$_y$**), these components were used to determinate the phase difference. The phase difference in the TM case is between 145 and 203 degrees, and between –47 and 87 degrees in the TE case.

5. Light trapping cavity enhanced light transmission through a sub-wavelength slit

The investigated structure is shown in the inset of Fig. 5(a). A normally incident plane wave (λ_0 = 650 nm) illuminates a 100 nm wide slit in silver film through a 40 nm thick semitransparent silver film. Figure 5(a) shows the normalized transmission efficiency of the slit when the gap (***g***) between the metal films is of the form: ***g*** = 277.5 nm + ***m***·325 nm, where ***m*** = 0,1,…,10. The red solid line in Fig. 5(a) shows the dependency of η on ***g*** under TM polarized illumination when ***g*** is varied from 10 to 600 nm in 10 nm steps. According to the results of the previous section, the slit length is chosen to be 165 nm under TM polarized illumination, and 130 nm under TE polarized illumination to obtain optimal transmission efficiency. In the TE case, the slit is filled by a medium having refractive index (***n***$_s$) of 3.8.

As shown in Fig. 5(a), the normalized transmission efficiency increases as a function of the gap between the metal films. This is due to the fact that the slit radiates both backward and forward, as illustrated in the previous section. The backward radiated light gets reflected from the semitransparent metal film back towards the slit and partially couples into it. In the sequel, this coupling process is referred to as the back-coupling effect and the light emanated by the slit and reflected back towards the slit from the semitransparent metal film is referred to as the back-coupled light. According to the analysis of the previous section, in the TM case the phase difference between ***H*****$_y$** component of back-scattered light and illuminating plane wave is between 145 and 203 degrees in the slit entrance. When the ***H*****$_y$** component of the backward radiated light propagates to the semitransparent metal film, reflects from it, and propagates back to the slit entrance, its phase changes in the cases of the resonance gap thickness by the factor of $2\boldsymbol{g}\boldsymbol{k_0} + \Delta\phi_{R,\boldsymbol{Hy}} = 334.4$ deg, where ***g*** = 277.5 nm, $\boldsymbol{k}_0 = 2\pi/\lambda_0$, and $\Delta\phi_{R,\boldsymbol{Hy}} = 27$ deg is the phase change experienced by the magnetic field, when a normally incident plane wave reflects from a 40 nm thick silver film. (In reality, the wave emanated by

#118380 - $15.00 USD Received 9 Oct 2009; revised 25 Nov 2009; accepted 2 Dec 2009; published 16 Dec 2009

the slit resembles more a cylindrical wave than a plane wave, but here a plane wave is used to approximate the situation. In the TE case, $\Delta\phi_{R,\boldsymbol{Ey}} = 153$ deg.) Thus, the phase difference of the $\boldsymbol{H_y}$ component of the illuminating plane wave and the back-coupled light is between 119.4 and 177.4 degrees depending on the slit length. Accordingly, the back-coupled light excites a slit wave guide mode that exhibits approximately the same phase difference with the mode excited by the illuminating plane wave than the back-coupled light with the illuminating plane wave. Due to the phase difference, these waveguide modes interfere destructively, which means that the back-coupled light decreases the transmission efficiency. As the gap between the metal films increases, the back-coupling effect gets weaker (due to the strong divergence of the field emanated by the slit), and more light gets through the slit. In the earlier section, we found that due to the multilayer resonance, the electric field is enhanced by a factor of 6.5 on the surface of the metal film. This means that transmission enhancement of $6.5^2 = 42.25$ could be obtained without the back-coupling effect.

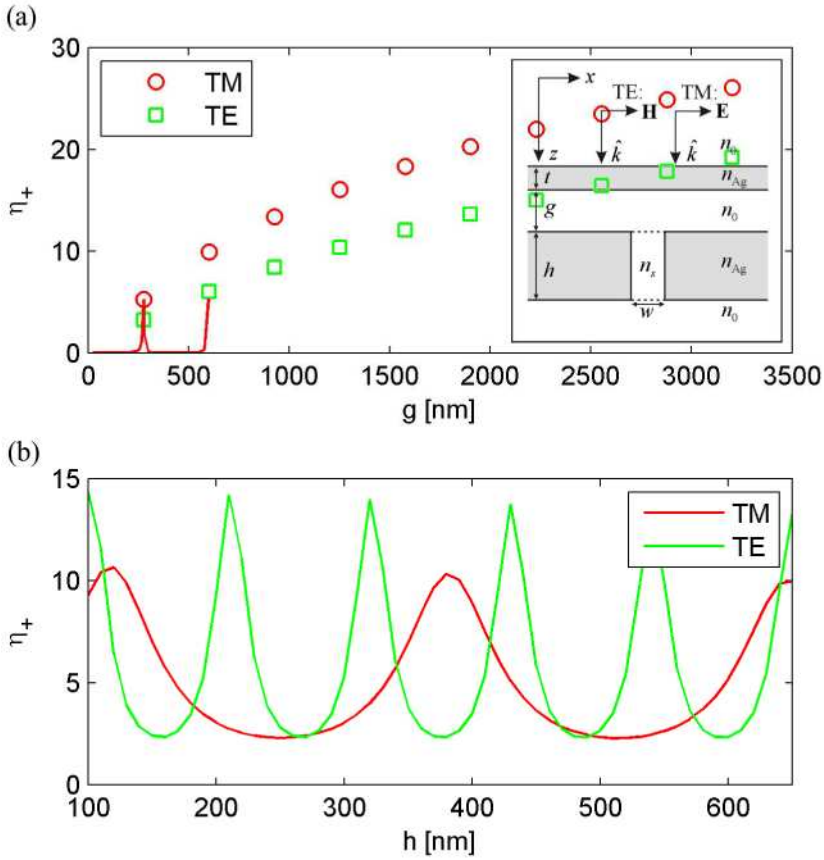

Fig. 5. (a) Transmission efficiency of the 100 nm wide slit with a light trapping cavity as a function of the distance between the semitransparent metal film ($\boldsymbol{t}$ = 40 nm) and the opaque metal film ($\boldsymbol{g}$ = 277.5 nm + $\boldsymbol{m}\cdot\lambda_0/2$, $\boldsymbol{m}$ = 1, 2,…, 10). TM polarization: n_s = 1.0, $\boldsymbol{h}$ = 165 nm. TE polarization: n_s = 3.8, h = 130 nm. The red solid line depicts the transmission efficiency in the TM case when the $\boldsymbol{g}$ is varied from 10 to 600 nm in 10 nm steps. (b) Transmission efficiency as a function of the opaque metal film thickness with the fixed gap thickness of 277.5 nm. Other parameters are the same as in (a). $\boldsymbol{n}_0$ = 1.0, and λ_0 = 650 nm.

#118380 - $15.00 USD Received 9 Oct 2009; revised 25 Nov 2009; accepted 2 Dec 2009; published 16 Dec 2009

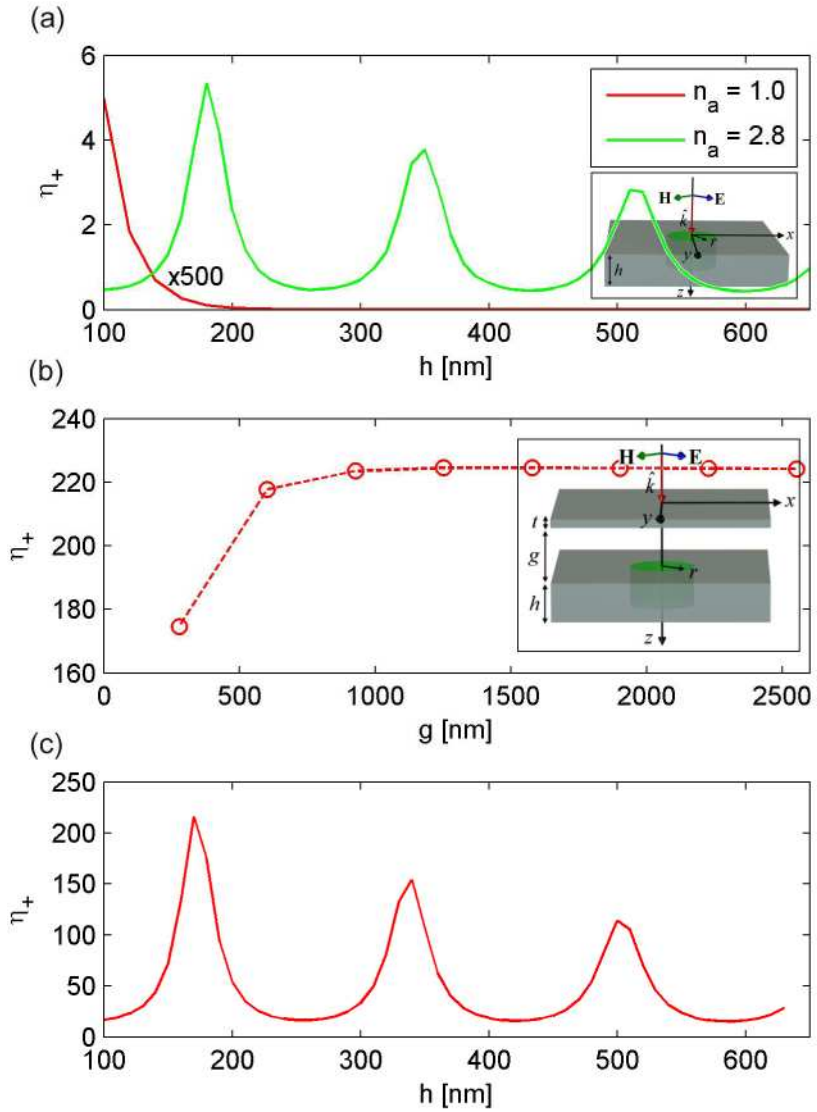

Fig. 6. (a) Transmission efficiency of a normally incident plane wave (λ_0 = 650 nm) through a cylindrical hole in a free standing silver film as a function the film thickness (***h***). The hole radius (***r***) is 50 nm and it is filled with a dielectric medium having the refractive index of n_a. The red line is magnified by a factor of 500. (b) Transmission efficiency of a cylindrical hole (***r*** = 50 nm, n_a = 2.8, ***h*** = 180 nm) with a light trapping cavity as a function of the distance between the semitransparent metal film (***t*** = 40 nm) and the opaque metal film (***g*** = 277.5 nm + $m \cdot \lambda_0/2$, ***m*** = 1, 2,…, 8). (c) Transmission efficiency as a function of the opaque metal film thickness with the fixed gap thickness of 277.5 nm. Other parameters are the same as in (b).

Figure 5(b) shows the normalized transmission efficiency as a function of the slit length (***h***) when the gap between the 40 nm thick semitransparent silver film and the opaque film is fixed to 277.5 nm. By comparing these results to the results of Figs. 4(a) and 4(b), it is observable that transmission peaks are now shifted to the slit lengths that are in close proximity of minimums of the normalized back-scattering efficiency (η_-) curves shown in Figs. 4(a) and (b). The back-coupling effect depends also on the phase of the back-coupled light, and thus the transmission peaks are not observed at the minimums of η_- -curves. The η_{+TE} curve in Fig. 5(b) exhibits a transmission maximum when ***h*** = 210 nm. In the absence of the semitransparent metal film, the normalized transmission efficiency of the slit (Fig. 4(a)) is

#118380 - $15.00 USD Received 9 Oct 2009; revised 25 Nov 2009; accepted 2 Dec 2009; published 16 Dec 2009

about 0.36. Assuming that there is no back-coupling effect, the multilayer resonance enhances the transmission by 42.25, which means that the transmission efficiency of the multilayer resonance slit could be about 15, which is in agreement with the results of Fig. 5(b).

6. Light trapping cavity enhanced light transmission through a cylindrical aperture

Light transmission through a cylindrical aperture reduces significantly when the aperture diameter gets smaller than $\lambda_0/2$. We have earlier shown [16] that light transmission through sub-wavelength apertures can be greatly enhanced by filling the aperture by a high index dielectric medium. This effect is also illustrated in Fig. 6(a) that shows the normalized transmission efficiency for a cylindrical aperture, 100 nm in diameter, in a silver film with and without the high refractive index (2.8) dielectric filling.

Transmission of a normally incident plane wave can be further boosted by using the light trapping cavity presented in the previous section. Figure 6(b) shows the transmission efficiency for the similar structure than Fig. 5(a), but now the slit is replaced by a high index (2.8) filled cylindrical hole having the diameter of 100 nm. To support the Fabry-Pérot resonance inside the cylindrical hole, the silver film thickness was chosen to be 180 nm according the results of Fig. 6(a). It is seen that the normalized transmission efficiency (η_+) curve depends much less on the gap thickness than in the slit case presented in Fig. 5(a). This is due to the fact that optical power of the back-scattered light spreads in 2D as inverse proportionally to the distance (~$\boldsymbol{1/d}$) from the aperture, whereas in 3D the relation is quadratic (~$\boldsymbol{1/d^2}$).

Figure 6(c) shows the normalized transmission efficiency as a function of the thickness of the opaque film (***h***) with the fixed gap thickness of 277.5 nm. The maximum transmission efficiency is obtained with ***h*** = 170 nm, i.e., the optimum thickness is shifted by ~10 nm from that of the aperture in a bare metal film.

7. Conclusions

In this paper, we have presented a new technique to enhance transmission of a normally incident, monochromatic plane wave through a sub-wavelength aperture in a metal film. The technique is based on the light trapping cavity formed in front of the aperture. The presented idea was verified by FDTD simulations for both sub-wavelength slits and cylindrical apertures. The transmission enhancement factor of ~40 was demonstrated for cylindrical hole filled with a high index dielectric medium. The presented idea may be applicable to periodic slit and hole arrays if the spacing between the holes is large enough to support formation of the light trapping cavity. It may also find applications in biosensors since the transmission efficiency is highly sensitive to refractive index changes occurring in the slit and in the gap region between the metal films.

#118380 - $15.00 USD Received 9 Oct 2009; revised 25 Nov 2009; accepted 2 Dec 2009; published 16 Dec 2009

PAPER IV

FDTD scattered field formulation for scatterers in stratified dispersive media

In: Optics Express 2010.
Vol. 18, No. 5, pp. 4380–4389.

FDTD scattered field formulation for scatterers in stratified dispersive media

Juuso Olkkonen*

VTT Technical Research Centre of Finland, Tietotie 3, P. O. Box 1000, 02044 VTT, Finland
**juuso.olkkonen@vtt.fi*

Abstract: We introduce a simple scattered field (SF) technique that enables finite difference time domain (FDTD) modeling of light scattering from dispersive objects residing in stratified dispersive media. The introduced SF technique is verified against the total field scattered field (TFSF) technique. As an application example, we study surface plasmon polariton enhanced light transmission through a 100nm wide slit in a silver film.

OCIS codes: (050.1755) Computational electromagnetic methods; (050.1220) Apertures; (240.6680) Surface plasmons.

References and links

1. K. S. Yee, "Numerical solution of initial boundary value problems involving Maxwell's equations in isotropic media," IEEE Trans. Antenn. Propag. **14**(3), 302–307 (1966).
2. A. Taflove, and S. C. Hagness, ***Computational Electrodynamics: The Finite-Difference Time-Domain Method*** (Second Edition, Artech House, INC., 2000).
3. K. S. Kunz, and R. J. Luebbers, ***The Finite Difference Time Domain Method for Electromagnetics*** (CRC Press, London, 1993).
4. S. Winton, P. Kosmas, and C. M. Rappaport, "FDTD simulation of TE and TM plane waves at nonzero incidence in arbitrary layered medium," IEEE Trans. Antenn. Propag. **53**(5), 1721–1728 (2005).
5. Y.-N. Jiang, D.-B. Ge, and S. J. Ding, "Analysis of TF-SF boundary for 2D-FDTD with plane p-wave propagation in layered dispersive and lossy media," Prog. In Electromagnetic Res **PIER 83**, 157–172 (2008).
6. J. B. Schneider, and K. Abdijalilov, "Analytic field propagation TFSF boundary for FDTD problems involving planar interfaces: PECs, TE, and TM," IEEE Trans. Antenn. Propag. **54(**9), 2531–2542 (2006).
7. K. Abdijalilov, and J. B. Schneider, "Analytic field propagation TFSF boundary for FDTD problems involving planar interfaces: lossy material and evanescent fields," IEEE Antennas Wirel. Propag. Lett. **5**(1), 454–458 (2006).
8. K. Demarest, R. Plump, and Z. Huan, "FDTD modeling of scatterers in stratified medium," IEEE Trans. Antenn. Propag. **43**(10), 1164–1168 (1995).
9. S.-C. Kong, J. J. Simpson, and V. Backman, "ADE-FDTD scattered field formulation for dispersive materials," IEEE Microwave Wireless Comp. Letters **18**(1), 4–6 (2008).
10. M. Okoniewski, M. Mrozowski, and M. A. Stuchly, "Simple treatment of multi-term dispersion in FDTD," IEEE Microwave Guided Wave Lett. **7**(5), 121–123 (1997).
11. D. F. Kelley, and R. J. Luebbers, "Piecewise linear recursive convolution for dispersive media using FDTD," IEEE Trans. Antenn. Propag. **44**(6), 792–797 (1996).
12. M. G. Moharam, D. A. Pommet, E. B. Grann, and T. K. Gaylord, "Stable implementation of the rigorous coupled-wave analysis for surface relief gratings: enhanced transmittance matrix approach," J. Opt. Soc. Am. A **12**, 1077–1086 (1995).
13. C.-T. Tai, ***Dyadic green functions in electromagnetic theory*** (Second Edition, IEEE Press, 1993).
14. S. D. Gedney, "An anisotropic perfectly matched layer-absorbing medium for the truncation of FDTD lattices," IEEE Trans. Antenn. Propag. **44**(12), 1630–1639 (1996).
15. P. B. Johnson, and R. W. Christy, "Optical constants of the noble metals," Phys. Rev., B, Solid State **6**(12), 4370–4379 (1972).

1. Introduction

The finite difference time domain (FDTD) method [1] is widely used as a numerical tool to solve electromagnetic scattering problems, where a spatially finite scatterer is illuminated by a plane wave. Plane waves are typically excited in FDTD either by the total field scattered field (TFSF) [2] or by the scattered field (SF) technique [3]. In the absence of a scatterer, both of these techniques produce a field that is called the incident field. When a scatterer interacts with the incident field, a scattered field is formed. The sum of the incident and the scattered field is referred to as the total field. The TFSF technique divides the computation domain into

#122264 - $15.00 USD Received 4 Jan 2010; revised 11 Feb 2010; accepted 12 Feb 2010; published 17 Feb 2010

the total field and the scattered field region separated by an interface that generates the incident field and guides it through the total field region. In the SF technique, Maxwell's equations are reformulated in such a manner that only the scattered fields are calculated by the FDTD method. Since the incident field is initially known, the total field is obtained as a sum of the incident and the scattered field.

Excitation of the incident field in FDTD is straightforward when scatterers reside in a homogenous background medium. The situation, however, is more complicated when the scatterers are located in a stratified background structure. This is mainly due to the fact that modeling propagation of the incident field in a uniform medium is much simpler than in stratified media. An exception is a case where a normally incident plane wave illuminates stratified media since an auxiliary one-dimensional FDTD simulation can be used as a real-time look-up table for the TFSF technique [2]. To handle obliquely incident plane waves in the TFSF technique, Winton et al. [4] have presented an approach based on multiple one-dimensional FDTD grids. The approach was further developed by Jian et. al. [5]. Schneider and Abdijalilov [6,7] have calculated incident fields for TFSF boundary analytically, including the numerical dispersion effects to obtain a non-leaking boundary. Demarest et al. [8] have introduced the SF technique for oblique plane waves in non-dispersive stratified media.

To our knowledge, this is the first time when the SF technique is presented for dispersive scatterers in dispersive stratified media. A SF formulation for dispersive materials was presented by Kong et al. [9], but in their formulation it is assumed that the incident field propagates in a uniform medium. In addition, their SF formulations depend on the used dispersive medium (Lorentz/Debye/Drude). In this paper, we present a simple approach that is nearly independent of the used dispersive medium.

This paper is organized as follows. In the next section, we introduce the scattered field technique in the frequency domain and then transform the obtained equations to the time domain. Section 3 considers in detail how the source term of the SF technique is calculated in practice. In section 4, we introduce the SF technique for scatterers in perfect electric conductor layers. The SF technique is then verified against the TFSF technique in Section 5. Surface plasmon polariton enhance light transmission through a slit is studied in Section 6 via the introduced SF technique. Finally, the summary and conclusions are presented in Section 7.

2. Scattered field technique

This section introduces the SF technique for dispersive scatterers in a dispersive stratified background structure. The SF technique is based on the fact that due to linearity of Maxwell's equations, the total electric and the magnetic field can be expressed as a sum of the incident field and the scattered field. That is,

$$\mathbf{E} = \mathbf{E}_{\text{inc}} + \mathbf{E}_{\text{sca}}, \tag{1}$$

$$\mathbf{H} = \mathbf{H}_{\text{inc}} + \mathbf{H}_{\text{sca}}. \tag{2}$$

We start from the frequency domain Maxwell's equations for a linear, non-magnetic ($\mu = \mu_0$) medium:

$$\nabla \times \mathbf{E}(\omega) = -\boldsymbol{j}\omega\mu_0 \mathbf{H}(\omega), \tag{3}$$

$$\nabla \times \mathbf{H}(\omega) = \boldsymbol{j}\omega\varepsilon(\omega)\mathbf{E}(\omega), \tag{4}$$

where μ_0 is the permeability of free space, and $\varepsilon(\omega) = \varepsilon_{\text{re}}(\omega) + \boldsymbol{j}\varepsilon_{\text{im}}(\omega)$ is the complex dielectric permittivity. We assume that the incident fields obey the following equations:

$$\nabla \times \mathbf{E}_{\text{inc}}(\omega) = -\boldsymbol{j}\omega\mu_0 \mathbf{H}_{\text{inc}}(\omega), \tag{5}$$

$$\nabla \times \mathbf{H}_{\text{inc}}(\omega) = \boldsymbol{j}\omega\varepsilon_{\text{inc}}(\omega)\mathbf{E}_{\text{inc}}(\omega), \tag{6}$$

#122264 - $15.00 USD Received 4 Jan 2010; revised 11 Feb 2010; accepted 12 Feb 2010; published 17 Feb 2010

where $\varepsilon_{inc}(\omega)$ is the local complex dielectric permittivity of the structure for which the incident field is known. Substituting Eqs. (1) and (2) into Eqs. (3) and (4), using Eqs. (5) and (6), and then rearranging terms, we have

$$\nabla \times \mathbf{E}_{sca}(\omega) = -\boldsymbol{j}\omega\mu_0 \mathbf{H}_{sca}(\omega) + \underbrace{\left(-\boldsymbol{j}\omega\mu_0 \mathbf{H}_{inc}(\omega) - \nabla \times \mathbf{E}_{inc}(\omega)\right)}_{=0}, \tag{7}$$

$$\nabla \times \mathbf{H}_{sca}(\omega) = \boldsymbol{j}\omega\varepsilon(\omega)\mathbf{E}_{sca}(\omega) + \mathbf{S}(\omega), \tag{8}$$

where

$$\mathbf{S}(\omega) = \boldsymbol{j}\omega\left[\varepsilon(\omega) - \varepsilon_{inc}(\omega)\right]\mathbf{E}_{inc}(\omega). \tag{9}$$

Maxwell's equations are now reformulated to such a form that only the scattered field components are required to be solved with the assumption that the incident field is initially known. Note that the source term $\mathbf{S}(\omega)$, which is the only quantity that depends on the incident field, is non-zero only in regions where $\varepsilon(\omega)$ differs from $\varepsilon_{inc}(\omega)$.

The frequency domain Eqs. (7)-(9) must be transformed to the time domain before they can be used in the FDTD method. Using the inverse Fourier transform, we obtain

$$\nabla \times \mathbf{E}_{sca}(\boldsymbol{t}) = -\mu_0 \frac{\partial}{\partial \boldsymbol{t}} \mathbf{H}_{sca}(\boldsymbol{t}), \tag{10}$$

$$\nabla \times \mathbf{H}_{sca}(\boldsymbol{t}) = \boldsymbol{F}^{-1}\left\{\boldsymbol{j}\omega\varepsilon(\omega)\mathbf{E}_{sca}(\omega)\right\} + \mathbf{S}(\boldsymbol{t}), \tag{11}$$

where

$$\mathbf{S}(\boldsymbol{t}) = \boldsymbol{F}^{-1}\left\{\mathbf{S}(\omega)\right\}. \tag{12}$$

Traditional total field FDTD kernels designed for dispersive materials can be used to solve discretized versions of Eqs. (10) and (11) with the difference that only the scattered field components are solved instead of the total field components. The term $\boldsymbol{F^{-1}\{j}\omega\varepsilon(\omega)\mathbf{E}_{sca}(\omega)\boldsymbol{\}}$ is typically incorporated into a FDTD model via the auxiliary differential equation (ADE) [10] or the recursive convolution method [11]. The SF technique presented herein is compatible with the both approaches. A total field FDTD implementation can be easily converted to calculate only scattered fields. The only required change is that the $\nabla \times \mathbf{H}(\boldsymbol{t})$ term is replaced in the total electric field update equation by $\nabla \times \mathbf{H}_{sca}(\boldsymbol{t}) - \boldsymbol{S}(\boldsymbol{t})$.

3. Calculation of the source term

To calculate the source term (12), first the interaction of the illuminating plane wave with the stratified background structure has to be solved in the frequency domain. Throughout this paper, we assume that the illuminating plane wave pulse exhibits the following time dependency in the coordinate origin:

$$\boldsymbol{f}(\boldsymbol{t}) = \exp\left[-(\boldsymbol{t} - \boldsymbol{t}_0)^2 / \tau^2\right] \sin(2\pi \boldsymbol{f}_0 (\boldsymbol{t} - \boldsymbol{t}_0)), \tag{13}$$

where $\boldsymbol{f}_0$ is the central frequency of the pulse, $\boldsymbol{t}_0$ is the time domain displacement of the pulse peak from the origin, and τ defines the $1/\boldsymbol{e}$ half width of the pulse in the time domain. First, $\boldsymbol{f}(\boldsymbol{t})$ is evaluated at the time instants $\boldsymbol{t}_k = \boldsymbol{k}\Delta\boldsymbol{t}$, $\boldsymbol{k} = 0,1,2,...,\ \boldsymbol{N}_{max}$, $\boldsymbol{N}_{max} = \boldsymbol{t}_{max}/\Delta\boldsymbol{t}$, in the time interval $[0, \boldsymbol{t}_{max}]$. Since the pulse $\boldsymbol{f(t)}$ is infinitely long in the time domain, it has to be truncated so that only values larger than γ are included into the discrete representation. In many cases, sufficient initial choices are $\gamma = 10^{-9}$, $\boldsymbol{t}_0 = [-\ln(\gamma)]^{1/2}\tau$ and $\boldsymbol{t}_{max} = 2\boldsymbol{t}_0$. Now, the frequency spectrum of $\boldsymbol{f}(\boldsymbol{t}_k)$ can be calculated via the discrete Fourier transform. The obtained complex frequency spectrum $\boldsymbol{A_0}(\omega_i)$ defines the amplitude and the initial phase for each monochromatic plane wave having angular frequency ω_i. Next, the interaction of the monochromatic plane waves with the background structure is solved via the transmittance matrix approach [12].

#122264 - $15.00 USD Received 4 Jan 2010; revised 11 Feb 2010; accepted 12 Feb 2010; published 17 Feb 2010

After the incident fields $\mathbf{E}_{inc}(\omega_i)$ are solved, the frequency domain source terms $\mathbf{S}(\omega_i)$ are calculated according to Eq. (9). Finally, the time domain source term $\mathbf{S}(t)$ is obtained from the frequency domain terms via the inverse Fourier transform.

When the time domain source term is calculated via the inverse Fourier transform, it is important to verify that spectral sampling resolution, given by $\Delta f = 1/t_{max}$, is adequate. This can be accomplished by calculating the time domain incident electric field $\mathbf{E}_{inc}(t)$ in each layer and checking that the field amplitude has decayed to a negligible value at $t = t_{max}$. This guarantees that we have properly sampled the source term in the frequency domain and we obtain an accurate transformation from the frequency to the time domain in Eq. (12). Here, we have assumed that in Eq. (9) $\varepsilon(\omega)$ and $\varepsilon_{inc}(\omega)$ are Fourier transformable functions, as is the case with Lorentz, Debye and Drude permittivity distributions.

Probably the most efficient way to evaluate the source term (12) is the fast Fourier transform (FFT). A problem with FFT is that it calculates the source for all time steps t_k, $k = 0,1,\ldots,N_{max}$, at once and thus the computer memory may run out with scatterers consisting of numerous Yee cells. A more viable approach is the discrete Fourier transform that allows the calculation of the source term (12) for each time step at a time. That is,

$$\mathbf{S}(t_k) = \mathrm{Re}\left\{ \sum_{i=0}^{N_{max}} \mathbf{S}(\omega_i) \exp[\, j\omega_i t_k \,] \right\}. \tag{14}$$

One way to speed-up the calculation of Eq. (14) is to include only frequencies ω_i at which the amplitude of the illuminating field $|A_0(\omega_i)|$ is non-negligible.

4. Source term for scatterers in a perfect electric conductor layer

Perfect electric conductor (PEC) is a medium, the electric conductivity of which approaches infinity. Spatially finite PEC scatterers are easily treated in the scattered field technique by applying $\mathbf{E}_{scat} = -\mathbf{E}_{inc}$ inside the scatterer [3]. If the stratified background structure of the incident field contains a PEC layer and the PEC layer includes scattering objects extending on its front surface or through the entire PEC layer, a more complicated approach is required to plant the incident field. The source term (12) is not directly evaluable since $\varepsilon_{inc}(\omega)$ is not defined for PEC. Thus, we replace the $j\omega\varepsilon_{inc}(\omega)\mathbf{E}_{inc}(\omega)$ term in Eq. (9) by $\nabla \times \mathbf{H}_{inc}(\omega)$ according to Eq. (6), and we obtain

$$\mathbf{S}(t) = F^{-1}\left\{ j\omega\varepsilon(\omega)\mathbf{E}_{inc}(\omega) - \nabla \times \mathbf{H}_{inc}(\omega) \right\}. \tag{15}$$

Inside a PEC layer, $\mathbf{E}_{inc} = \mathbf{0}$ and $\mathbf{H}_{inc} = \mathbf{0}$, which means that also the source term is zero. However, at the surface of the PEC layer fields are non-zero. The boundary conditions [13] state that at the surface of the PEC layer: $\hat{\boldsymbol{n}} \times \mathbf{E}_{inc} = \mathbf{0}$, $\hat{\boldsymbol{n}} \times \mathbf{H}_{inc} = \mathbf{J}_s$, and $\hat{\boldsymbol{n}} \cdot \mathbf{H}_{inc} = 0$, where $\mathbf{J}_s$ is the surface current density and $\hat{\boldsymbol{n}}$ is a unit vector normal to the PEC surface. Since $\mathbf{E}_{inc} \neq \mathbf{0}$ and $\mathbf{H}_{inc} \neq \mathbf{0}$ only on the surface of the PEC layer, the source term is added only to the electric field components that reside on this particular surface. Because tangential components of $\mathbf{H}_{inc}$ are not continuous across the interface, the $\nabla \times \mathbf{H}_{inc}(\omega)$ term cannot be evaluated analytically, but we can find a numerical approximation as illustrated next.

Let us consider a PEC interface $z = z_0$ in the xy-plane with a unit surface normal $\hat{\boldsymbol{n}} = (0,0,-1)$. At the interface, $E_{x,inc} = 0$, $E_{y,inc} = 0$ and $H_{z,inc} = 0$ due to the boundary conditions. Using the central finite difference approximation, $\nabla \times \mathbf{H}_{inc}(\omega)$ term can be expressed at the interface $z = z_0$ as

#122264 - $15.00 USD Received 4 Jan 2010; revised 11 Feb 2010; accepted 12 Feb 2010; published 17 Feb 2010

$$\left(\nabla\times\mathbf{H}_{\mathrm{inc}}(\omega)\right)_{\boldsymbol{x}}\Big|_{\boldsymbol{z}=\boldsymbol{z}_0}=\left(\underbrace{\frac{\partial \boldsymbol{H}_{\boldsymbol{z},\mathrm{inc}}}{\partial \boldsymbol{y}}}_{=0}-\frac{\partial \boldsymbol{H}_{\boldsymbol{y},\mathrm{inc}}}{\partial \boldsymbol{z}}\right)\Bigg|_{\boldsymbol{z}=\boldsymbol{z}_0} \tag{16.1}$$

$$\approx-\frac{\overbrace{\boldsymbol{H}_{\boldsymbol{y},\mathrm{inc}}(\boldsymbol{z}_0+\Delta\boldsymbol{z}/2)}^{=0}-\boldsymbol{H}_{\boldsymbol{y},\mathrm{inc}}(\boldsymbol{z}_0-\Delta\boldsymbol{z}/2)}{\Delta\boldsymbol{z}}=\frac{\boldsymbol{H}_{\boldsymbol{y},\mathrm{inc}}(\boldsymbol{z}_0-\Delta\boldsymbol{z}/2)}{\Delta\boldsymbol{z}},$$

$$\left(\nabla\times\mathbf{H}_{\mathrm{inc}}(\omega)\right)_{\boldsymbol{y}}\Big|_{\boldsymbol{z}=\boldsymbol{z}_0}=\left(\frac{\partial \boldsymbol{H}_{\boldsymbol{x},\mathrm{inc}}}{\partial \boldsymbol{z}}-\underbrace{\frac{\partial \boldsymbol{H}_{\boldsymbol{z},\mathrm{inc}}}{\partial \boldsymbol{x}}}_{=0}\right)\Bigg|_{\boldsymbol{z}=\boldsymbol{z}_0} \tag{16.2}$$

$$\approx\frac{\overbrace{\boldsymbol{H}_{\boldsymbol{x},\mathrm{inc}}(\boldsymbol{z}_0+\Delta\boldsymbol{z}/2)}^{=0}-\boldsymbol{H}_{\boldsymbol{x},\mathrm{inc}}(\boldsymbol{z}_0-\Delta\boldsymbol{z}/2)}{\Delta\boldsymbol{z}}=-\frac{\boldsymbol{H}_{\boldsymbol{x},\mathrm{inc}}(\boldsymbol{z}_0-\Delta\boldsymbol{z}/2)}{\Delta\boldsymbol{z}},$$

$$\left(\nabla\times\mathbf{H}_{\mathrm{inc}}(\omega)\right)_{\boldsymbol{z}}\Big|_{\boldsymbol{z}=\boldsymbol{z}_0}=\left(\frac{\partial \boldsymbol{H}_{\boldsymbol{y},\mathrm{inc}}}{\partial \boldsymbol{x}}-\frac{\partial \boldsymbol{H}_{\boldsymbol{x},\mathrm{inc}}}{\partial \boldsymbol{y}}\right)\Bigg|_{\boldsymbol{z}=\boldsymbol{z}_0}, \tag{16.3}$$

where the magnetic field components in the plane $\boldsymbol{z}=\boldsymbol{z}_0+\Delta\boldsymbol{z}/2$ are zero since they are located inside the PEC layer. Equation (16.3) can be evaluated analytically. In a typical staggered uniform Yee grid, the electric field components are located in the following coordinate points: $\boldsymbol{E}_{\boldsymbol{x}}$: $(\boldsymbol{i}\Delta\boldsymbol{x}, (\boldsymbol{j}+1/2)\Delta\boldsymbol{y}, (\boldsymbol{k}+1/2)\Delta\boldsymbol{z})$, $\boldsymbol{E}_{\boldsymbol{y}}$: $((\boldsymbol{i}+\boldsymbol{1/2})\Delta\boldsymbol{x}, \boldsymbol{j}\Delta\boldsymbol{y}, (\boldsymbol{k}+1/2)\Delta\boldsymbol{z})$, $\boldsymbol{E}_{\boldsymbol{z}}$: $((\boldsymbol{i}+\boldsymbol{1/2})\Delta\boldsymbol{x}, (\boldsymbol{j}+1/2)\Delta\boldsymbol{y}, \boldsymbol{k}\Delta\boldsymbol{z})$, where $\boldsymbol{i}$, $\boldsymbol{j}$, and $\boldsymbol{k}$ are integers and $\Delta\boldsymbol{x}$, $\Delta\boldsymbol{y}$, and $\Delta\boldsymbol{z}$ define the dimensions of the Yee cell. If we choose that the PEC interface is located at $\boldsymbol{z}=(\boldsymbol{k}_0+1/2)\Delta z$, then only $\boldsymbol{E}_{\boldsymbol{x}}$ and $\boldsymbol{E}_{\boldsymbol{y}}$ components reside on this surface, which means that Eq. (16.3) is not needed at all. Since tangential components of the incident electric field are zero on the PEC interface, $\boldsymbol{x}$ and $\boldsymbol{y}$ component of the source terms reduces to the form

$$\boldsymbol{S}_{\boldsymbol{x}}(\boldsymbol{i},\boldsymbol{j}+1/2,\boldsymbol{k}_0+1/2)=\frac{\boldsymbol{H}_{\boldsymbol{y},\mathrm{inc}}(\boldsymbol{i},\boldsymbol{j}+1/2,\boldsymbol{k}_0)}{\Delta\boldsymbol{z}}, \tag{17.1}$$

$$\boldsymbol{S}_{\boldsymbol{y}}(\boldsymbol{i}+1/2,\boldsymbol{j},\boldsymbol{k}_0+1/2)=-\frac{\boldsymbol{H}_{\boldsymbol{x},\mathrm{inc}}(\boldsymbol{i}+1/2,\boldsymbol{j},\boldsymbol{k}_0)}{\Delta\boldsymbol{z}}. \tag{17.2}$$

Since these equations do not contain any frequency dependent multipliers, the time domain representation is obtained by replacing the frequency domain quantities by the corresponding time domain quantities.

5. Validation of the scattered field technique

In this section, we verify the validity of the SF technique against the TFSF technique using the two dimensional FDTD method. The FDTD mesh was terminated with the anisotropic perfectly matched absorbing boundaries [14]. Dispersive materials were included into the FDTD model via the auxiliary differential equation [10] and modeled as a single pole Lorentz medium having relative dielectric permittivity of the form:

$$\varepsilon_{\boldsymbol{r}}(\omega)=\varepsilon_\infty+\frac{(\varepsilon_{\boldsymbol{s}}-\varepsilon_\infty)\omega_0^2}{\omega_0^2+2\boldsymbol{j}\omega\delta_0-\omega^2}, \tag{18}$$

where ε_s is the static permittivity, ε_∞ is the relative permittivity at infinite frequencies, ω_0 is the pole location, and δ_0 is the damping factor. In this work, we consider only two dispersive materials, namely silver and gold. Lorentz parameters for these noble metals were found

#122264 - $15.00 USD Received 4 Jan 2010; revised 11 Feb 2010; accepted 12 Feb 2010; published 17 Feb 2010

fitting Eq. (18) to the experimental data [15]. For silver, we found the following values provide a good fit: ε_s = 4.7982x10^7, ε_∞ = 4.2167, δ_0 = 1.4046x10^{13} Hz, and ω_0 = 2.0254x10^{12} Hz, and for gold: ε_s = 2.0397x10^8, ε_∞ = 22.3162, δ_0 = 4.4183x10^{13} Hz, and ω_0 = 1.2150x10^{12} Hz.

The SF and TFSF technique are compared by using each to simulate the transmission of a normally incident, TM polarized plane wave pulse through a 100 nm wide slit in a 200 nm thick silver film. The time domain data was transformed to the frequency domain to obtain wavelength dependent transmission efficiency curves. To ensure that the SF technique works properly with dispersive scatterers, the simulations are also performed for the case in which a 80 nm diameter gold cylinder is located in the middle of the slit entrance. In both cases, the slit structure is illuminated by a normally incident plane wave pulse (τ = 1.1325 fs, $\boldsymbol{f}_0$ = $\boldsymbol{c}_0$/640nm, $\boldsymbol{c}_0$ = speed of light in vacuum) propagating in the $\boldsymbol{z}$ direction. The TFSF technique was used to model the problem as follows: Since the background structure, where the slit resides, is invariant in the $\boldsymbol{x}$ and the $\boldsymbol{y}$ directions, propagation of a normally incident plane wave pulse through the background structure can be modeled using a one-dimensional FDTD simulation. This one-dimensional simulation, which is run simultaneously with the actual two-dimensional FDTD simulation, is then used as a look-up table to obtain the incident field for the TFSF technique. The use of look-up tables with the TFSF technique is described in detail in Ref [2].

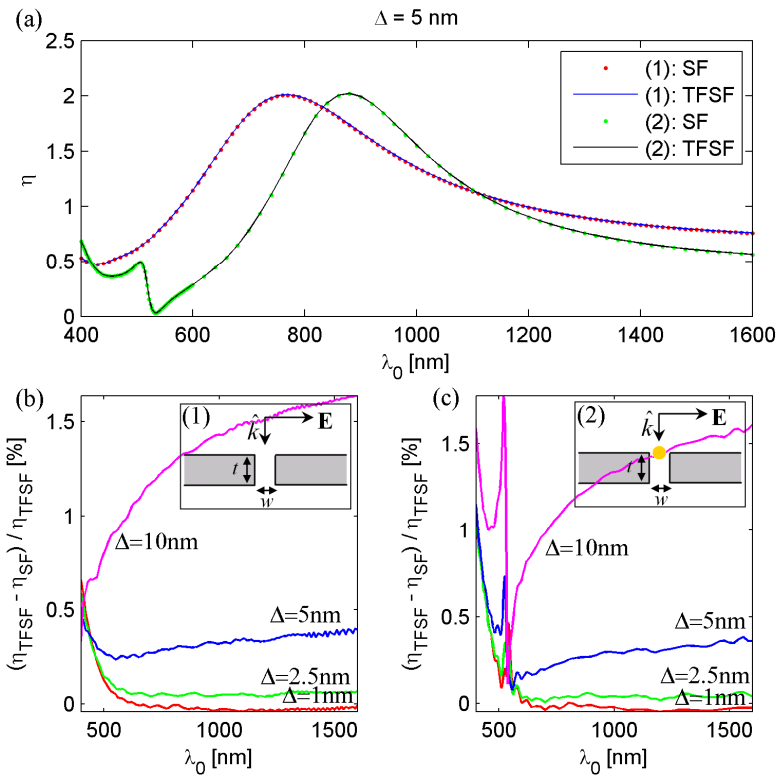

Fig. 1. (a) Normalized transmission efficiency of a normally incident plane having free space wavelength of λ_0 through a 100 nm wide ($\boldsymbol{w}$) slit in a 200 nm thick ($\boldsymbol{t}$) silver film as calculated by the SF and the TFSF technique. In the case (1), the slit is empty, whereas in the case (2), the slit contains a 80 nm diameter gold cylinder in the slit entrance as illustrated in the inset (2). These results were obtained with a square Yee cell size (Δ) of 5 nm. (b) Relative percentage error between the SF and the TFSF techniques as function of the λ_0 in the case (1) for square Yee cell sizes of 10, 5, 2.5 and 1 nm. (c) The same as (b), but now a 80 nm diameter gold cylinder is located in the slit entrance.

#122264 - $15.00 USD Received 4 Jan 2010; revised 11 Feb 2010; accepted 12 Feb 2010; published 17 Feb 2010

Light transmission through a slit is usually characterized via the normalized transmission efficiency (η), which is the ratio of the transmitted power behind the slit and the incident power at the geometrical entrance of the slit. Figure 1(a) shows a comparison of the transmission efficiencies obtained by the SF and the TFSF techniques for a 100 nm wide slit in a 200 nm thick silver film as a function of the free space wavelength (λ_0). In the case (1), the slit is empty, while in the case (2), a gold cylinder, 80 nm in diameter, is located in the middle of the slit entrance. These results were obtained with a square Yee cell size of 5 nm. Figure 1(b) shows the relative percentage error between the SF and TFSF technique in the case (1) for the square Yee cell sizes of 10, 5, 2.5 and 1 nm. The Fig. 1(c) shows the same data for the case (2). In both cases, good agreement is observed between the techniques. The error clearly diminishes with the decreasing cell size.

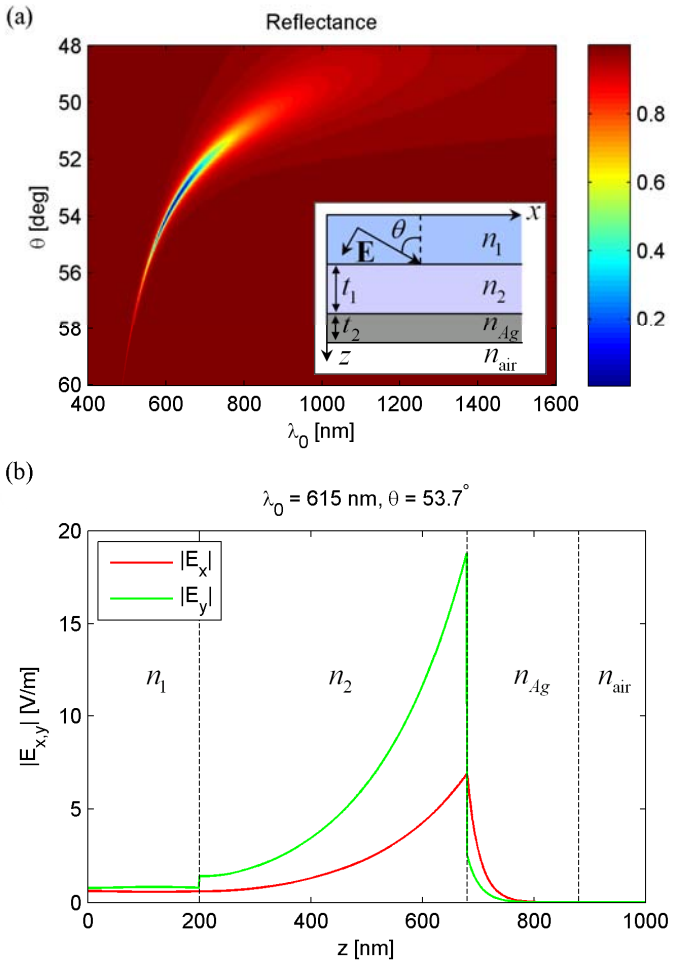

Fig. 2. (a) Reflectance of a TM polarized plane wave from the multilayer structure shown in the inset ($\boldsymbol{t}_1$ = 480 nm, $\boldsymbol{t}_2$ = 200 nm, $\boldsymbol{n}_1$ = 2.0, $\boldsymbol{n}_2$ = 1.5, $\boldsymbol{n}_{air}$ = 1.0) as a function of the angle of incidence (θ) and the free space wavelength λ_0. The plane wave is incident in the $\boldsymbol{n}_1$-medium. When θ = 53.7° and λ_0 = 615 nm, the reflectance of the structure is practically zero and nearly all incident light is coupled to SPPs. At the studied wavelength range, transmittance through the structure is always zero due to the opaque silver film. (b) Amplitude of the electric field components in the studied structure at the SPP resonance angle and the wavelength. Incident electric field amplitude is 1.0 V/m in the $\boldsymbol{n}_1$-medium. The dashed black lines show the locations of the material interfaces of the studied structure.

#122264 - $15.00 USD Received 4 Jan 2010; revised 11 Feb 2010; accepted 12 Feb 2010; published 17 Feb 2010

6. Surface plasmon polariton enhanced light transmission through a slit in a metal film

This section demonstrates the usability of the introduced SF technique in the analysis of surface plasmon polariton (SPP) enhanced light transmittance through a slit in a silver film. A SPP is a composite electromagnetic disturbance that occurs when an incident light field couples resonantly with an oscillating surface charge density distribution. Since the induced surface charge density is proportional to the discontinuity of the electric field component normal to the interface, only transverse magnetic (TM) polarized light can excite SPPs. A semi-infinite dielectric/metal-interface, in which both the metal and the dielectric medium are very thick, supports only a bound SPP mode, the field amplitude of which decays exponentially with distance on the both sides of the interface. SPPs with frequency ω have larger momentum than light that propagates in the adjacent dielectric medium with frequency ω. Therefore directly incident light cannot excite any SPP modes. Traditionally, SPPs are excited by an evanescent field produced by a prism or a grating that resides close to the dielectric/metal interface.

The inset of Fig. 2(a) shows a multilayer structure that support excitation of SPPs at the $\boldsymbol{n}_2/\boldsymbol{n}_{Ag}$-interface. The first layer ($\boldsymbol{n}_1$ = 2.0) represents the prism layer and the second layer ($\boldsymbol{n}_2$ = 1.5) is a spacer between the prism and the silver film. The incident TM polarized plane wave having free space wavelength of λ_0 is incident in the $\boldsymbol{n}_1$-layer. The angle of incidence is denoted by θ. The refractive index of silver was defined by the single pole Lorentz dispersion model introduced in the previous section. Figure 2(a) shows the calculated reflectance of the structure with $\boldsymbol{t}_1$ = 480 nm and $\boldsymbol{t}_2$ = 200 nm. The transmittance through the structure is always zero at the studied wavelength range due to the opaque silver film. When θ = 53.7° and λ_0 = 615 nm, the reflectance of the structure is practically zero and almost all light is coupled to SPPs. The electric field amplitude profiles of $\boldsymbol{E}_x$ and $\boldsymbol{E}_y$ components in this resonance case are plotted along the $\boldsymbol{z}$-axis in Fig. 2(b). The incident electric field amplitude is 1.0 V/m in the $\boldsymbol{n}_1$-layer. Due to SPPs, the electric field amplitude is significantly enhanced at the $\boldsymbol{n}_2/\boldsymbol{n}_{Ag}$-interface.

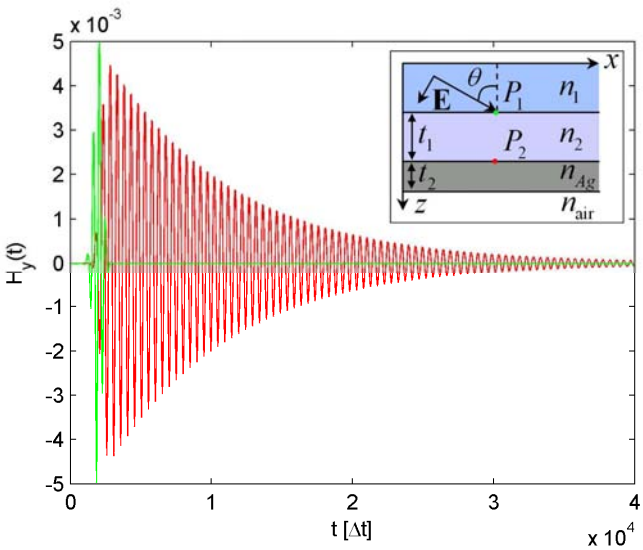

Fig. 3. The structure shown in the inset ($\boldsymbol{n}_1$ = 2.0, $\boldsymbol{n}_2$ = 1.5, $\boldsymbol{t}_1$ = 480nm, $\boldsymbol{t}_2$ = 200nm) is illuminated by a TM polarized ($\boldsymbol{H}_y$, $\boldsymbol{E}_x$, $\boldsymbol{E}_z$) plane wave pulse at the SPP resonance angle (θ = 53.7°). The pulse shape of the illuminating magnetic field is given by Eq. (13) with τ = 1.6988 fs and $\boldsymbol{f}_0 = \boldsymbol{c}_0/533.3$nm. The green line shows the magnetic field amplitude of the illuminating field in the point $\boldsymbol{P}_1$, whereas the red line shows $\boldsymbol{H}_y$ in the point $\boldsymbol{P}_2$ at the surface of the silver film. $\boldsymbol{H}_y$ in the point $\boldsymbol{P}_2$ decays slowly to zero due to SPPs propagating along the silver film.

Next, we form a 100 nm wide slit into the silver film of the considered multilayer structure and study how SPPs influence on light transmission through the slit. In the SF technique, the

#122264 - $15.00 USD Received 4 Jan 2010; revised 11 Feb 2010; accepted 12 Feb 2010; published 17 Feb 2010

first task is to calculate the solution for the incident field in the absence of scatterers. At the SPP resonance angle, a part of the incident plane wave pulse is coupled to SPPs, and a slowly decaying time domain field exists at the $\boldsymbol{n}_2/\boldsymbol{n}_{Ag}$-interface. This is demonstrated in Fig. 3, where a green line shows the $\boldsymbol{H_y}$ component of the illuminating TM-polarized ($\boldsymbol{H_y}$, $\boldsymbol{E_x}$, $\boldsymbol{E_z}$) plane wave pulse in the point $\boldsymbol{P}_1$ at the $\boldsymbol{n}_1/\boldsymbol{n}_2$-interface. The pulse shape is given by Eq. (13) with τ = 1.6988 fs and $\boldsymbol{f}_0 = \boldsymbol{c}_0/533.3$nm. The red line shows the time domain magnetic field in the point $\boldsymbol{P}_2$ at the surface of the silver film. Clearly, the time duration at which the field decays to zero at the $\boldsymbol{n}_2/\boldsymbol{n}_{Ag}$-interface is much larger than the duration of the illuminating pulse due to SPPs propagating along the interface. This has to be taken into account in the spectral sampling resolution ($\Delta\boldsymbol{f} = 1/\boldsymbol{t}_{max}$) of the illuminating plane wave pulse (for details, see Section 3). In practice, $\boldsymbol{t}_{max}$ has to be so large that at $\boldsymbol{t} = \boldsymbol{t}_{max}$ field is decayed to zero in all points of the FDTD mesh.

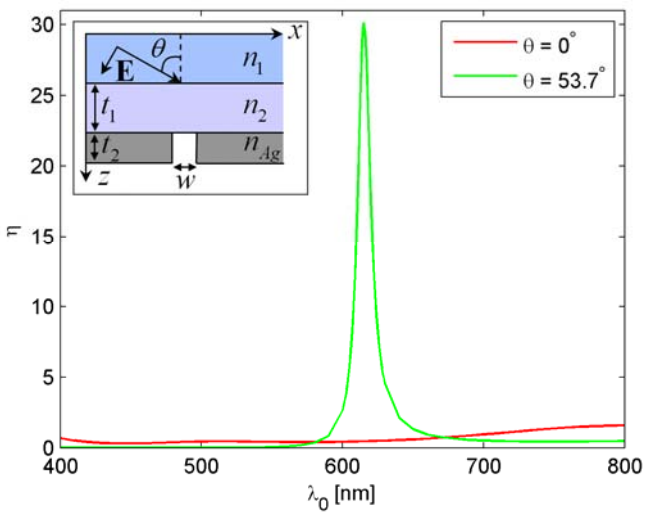

Fig. 4. Normalized transmission efficiency of a TM polarized plane wave through a slit structure shown in the inset ($\boldsymbol{n}_1$ = 2.0, $\boldsymbol{n}_2$ = 1.5, $\boldsymbol{t}_1$ = 480nm, $\boldsymbol{t}_2$ = 200nm, $\boldsymbol{w}$ = 100nm) as a function of the free space wavelength λ_0. The plane wave is incident in the $\boldsymbol{n}_1$-layer with the incidence angle of θ. When θ = 53.7° and λ_0 = 615 nm, light transmission through the slit is enhanced due to the excitation of SPPs.

Figure 4 shows the normalized transmission efficiency of a 100 nm wide slit in the silver film of the considered multilayer structure as calculated using the introduced SF technique. The used square Yee cell size was 2.5 nm. With all angles of incidence, the transmitted power through the slit is normalized by the power that would impinge on the slit entrance in the case that $\boldsymbol{n}_1 = \boldsymbol{n}_2$ = 2.0 and θ = 0°. The results clearly show that the excitation of SPPs on the surface of the silver film greatly enhances light transmission through the slit.

7. Summary and conclusions

This paper introduces a simple SF technique for dispersive scatterers in dispersive stratified media. An incident time domain plane wave pulse is first decomposed to time harmonic plane waves having angular frequency ω_i. The interaction of each time harmonic plane wave with the stratified background structure is then solved using the transmittance matrix approach. After the solution for the incident electric fields is found, the frequency domain source term is calculated according to Eq. (9). The same Eq. (9) can be used for all dispersive medium, such as Lorentz, Debye and Drude. Finally, the time domain source term is obtained from the frequency domain terms via the inverse Fourier transform. Dispersive materials are typically incorporated into the FDTD method via the auxiliary differential equation [10] or the recursive convolution method [11]. The introduced technique is compatible with the both

#122264 - $15.00 USD Received 4 Jan 2010; revised 11 Feb 2010; accepted 12 Feb 2010; published 17 Feb 2010

approaches. The introduced SF technique is not limited only to plane wave pulses but it can be used with all light beams that can be decomposed to plane waves, as is the case with e.g. the Gaussian and Bessel beams.

The introduced SF technique was verified against the TFSF technique in transmittance of a normally incident plane wave pulse through a 100 nm wide slit in a 200 nm thick silver film. In the second case, a 80 nm diameter gold cylinder was located in the slit entrance. In both cases, a good agreement between the techniques was found. Finally, we studied SPP enhanced light transmittance through a 100nm wide slit in a silver film using the SF technique. The obtained results clearly show that SPPs provide a mechanism to enhance light transmittance through a sub-wavelength slit in a metal film.

#122264 - $15.00 USD Received 4 Jan 2010; revised 11 Feb 2010; accepted 12 Feb 2010; published 17 Feb 2010

PAPER V

Readout modeling of super resolution disks

In: Japanese Journal of Applied Physics 2004.
Vol. 43, No. 7B, pp. 4718–4723.

Japanese Journal of Applied Physics
Vol. 43, No. 7B, 2004, pp. 4718–4723

Readout Modeling of Super Resolution Disks

Kari KATAJA[1,*], Juuso OLKKONEN[1,2], Janne AIKIO[1] and Dennis HOWE[2]

[1]*VTT Electronics, Kaitovayla 1, B.O. Box 1100, FIN-90571 Oulu, Finland*
[2]*University of Arizona, Optical Sciences Center, Tucson, AZ 85721-0094, USA*

(Received December 10, 2003; accepted December 26, 2003; published July 29, 2004)

We describe 3-dimensional numerical simulations (performed using a finite-difference-time-domain modeling tool) of the readout of very small marks recorded on the data surface of an optical storage medium that incorporates a super resolution (SR) structure comprised of two dielectric thin films which encapsulate a thin AgO_x film. We study how different types of light scattering objects, which are dynamically formed in the SR structure during readout of the recorded data surface, affect the characteristics of the reflected optical power modulation. [DOI: 10.1143/JJAP.43.4718]

KEYWORDS: super resolution, optical data storage, FDTD, silver oxide, readout

1. Introduction

The resolution of the conventional optical disk playback process, i.e., reading a conventional optical disk with a conventional optical head, is limited by diffraction. This means that the quality of the readout signal corresponding to the detection of very small recorded marks and spaces in the data layer of the disk is severely degraded when the size of such very small marks and spaces becomes less than the resolution limit (RL) of the conventional optical pickup head (OPU). The RL of the diffraction limited optical system is defined by the equation $d_{RL} = \lambda/4NA$, where d_{RL} is the diameter of the smallest resolvable mark, λ is the wavelength of the OPU's laser source and NA is the numerical aperture of the OPU's objective lens. Different techniques such as solid immersion lens (SIL),[1)] very small aperture laser (VSAL)[2)] and super resolution (SR) near field structure[3,4)] are being extensively studied to overcome this limit. All of these techniques improve the small mark readout signal quality by reducing the effective spot diameter at the data layer. In SIL and VSAL techniques, this is accomplished by coupling evanescent field at a flat optical exit surface of the SIL, or the near-field light at the VSAL output facet, into the data layer of a first surface recording optical disk. This requires mounting the SIL or VSAL on a flying slider whose distance from the recording medium has to be precisely controlled. However, SR systems employ a disk which has a SR structure coated directly on top of the disk's data layer. During recording and readout, the light spot focused on this structure causes an aperture that is smaller than the focused spot's full-width-half-maximum diameter to be formed in-situ (in real time) in the structure (via some kind of photo/thermal/chemical process). Evanescent light transmitted by this small aperture probes the data layer, thereby reducing the effective size of the laser spot. Therefore, the SR disk can be written and read using a conventional OPU that focuses light through the substrate, whereas the SIL and VSAL systems require using a first surface recording disk together with air-bearing slider to maintain the close distance ($\sim$100 nm) to the disk's data layer. The close flying height can be a serious problem if dust can enter the system when removable media is used.

However, the mechanism responsible for electromagnetic field coupling of the SR aperture and the data marks in the SR disk's data layer is not completely understood. Therefore, the main objective of the work reported here is to study the electromagnetic fields within several types of apertures that may be physically formed in SR structures during readout of the SR disk and try to explain the SR readout mechanism. In addition, even though recent works indicate that SR systems that employ thin films of either AgO_x[5)] or PtO_x[6,7)] function only as a write once medium, that is, the SR structure contains permanent apertures extant in its SR layer after the writing process, in this work we assume that a aperture in the SR layer opens up dynamically beneath the focused laser spot as it scans over the SR structure.

In the following, we shall assume that the data layer is a thin film of GeSbTe (GST) and that the recorded marks consist of local amorphous regions within an otherwise crystalline-phase film of this material. When marks, which are smaller in size than the RL of the conventional OPU, are illuminated with the readout spot, an evanescent field (or perhaps a surface plasmon) is generated within the disk's data layer.[8,9)] If the evanescent field is perturbed by some object or an aperture, it can partially couple with the perturbing object and further radiate to the far field (cf. frustrated total internal reflection). Depending on the coupling efficiency of the evanescent fields and the noise level of the readout system, the marks beyond the resolution limit may be resolved in the far field by a conventional readout system.

The goal of this work is to find SR aperture geometries that enhance the optical power (I) modulation when marks having diameter $< d_{RL}$ are read. That is, the modulation from the SR disk is increased versus that obtained when a conventional disk having identical size marks is read using the same OPU. Finding a SR aperture that produces the desired results would enable us to model the SR system writing and reading process and better understand the SR phenomenon. In the next Section, we briefly describe the numerical model. Results from several simulations are presented in §3 and some discussions and conclusions are presented in §4 and §5.

2. Model

The finite difference time domain (FDTD) method[10)] was used as the main electromagnetic (EM) modeling tool in this study. Our FDTD software runs on a parallel computing Beowulf cluster. The readout performance of an optical disk is modeled by first calculating the reflected EM fields in on-

*E-mail address: kari.j.kataja@vtt.fi

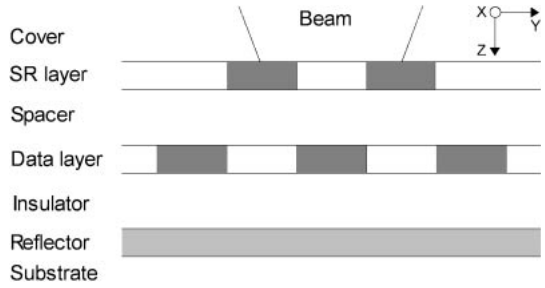

Fig. 1. System model with all the possible components. In the various simulations, some disk layers are removed. 'Beam' represents the focused readout laser beam.

mark and off-mark situations, which are assumed to correspond to the minimum and maximum I at the detector plane. The electric field components in the far field were computed via the plane wave spectrum (PWS) method,[11] and the far field intensity is obtained by summing these components in quadrature. The total I received by the detector is calculated by integrating the far field intensity over the NA of the OPU's objective lens.

A schematic of the simulation geometry is shown in Fig. 1. The layer structure consists of cover, SR, spacer, data, insulator, reflector and substrate layers. The tri-layer comprised of the cover, SR and spacer layers constitutes the SR structure; the SR layer being the "active" layer in which the aperture/scatterers are formed (in this work the SR layer is taken to be a thin film of AgO_x and a formed aperture/scatterer is comprised of two different, geometrical distributions of metallic Ag in this layer that are disposed directly beneath the focused readout light spot). The excitation plane of the incident beam is located inside the cover layer and therefore the air/cover layer interface (i.e., the upper surface of the cover layer) is neglected in the simulations. The system considered in this work does not include a land/groove structure which would affect the reflected EM fields and also causes the reflected EM fields to depend upon the playback light's polarization. That is, all the layers are just planar thin films. So far we have used only the *y*-polarized input beam, but *x*-polarized and circular polarized beams should be studied as well. In addition, in some of the simulations the reflector layer is not used. Therefore, in simplest form, the simulated structure consists only of cover, data and substrate layers (and this simple form corresponds to a conventional phase change optical disk that is designed for 'first surface' recording/playback).

The refractive indexes and layer thicknesses used for the thin films in the simulations are shown in Table I. Some of the layer thicknesses are changed in the simulations in order to optimize the readout performance. Therefore, the nominal thickness of each layer was used only as a starting point in the simulations. In addition, the cover and substrate layers do not have finite thickness, but they extend to infinity from the FDTD modeling point of view. The aperture that is formed in the SR structure's active layer is modeled as either a donut-shaped silver (Ag) ring that surrounds an oxygen bubble or as a cylinder of metallic Ag (in the sequel we refer to this latter aperture/scatterer type as an light scattering center (LSC)). Both of these types of aperture/scatterer are centered on the optical axis of the focused readout light spot.

Table I. Thin film layer thicknesses and material refractive index used in the modeling.

Layer			Refractive index	Nominal thickness [nm]
Cover	(ZnS-SiO_2)		2.2	—
SR layer	(AgO_x)		$2.50 + 0.11i$	15
	(Ag)		$0.27 + 4.43i$	
Spacer	(ZnS-SiO_2)		2.2	40
Data layer	(GST)	crystal	$4.6 + 4.2i$	20
		amorphous	$4.2 + 1.9i$	
Insulator	(ZnS-SiO_2)		2.2	20
Reflector	(Al)		$1.47 + 7.79i$	20
Substrate	(ZnS-SiO_2)		2.2	—

Note that the donut shaped aperture is also reported in the experimental work by Ho *et al.*[12] and Her *et al.*[13] The LSC type of SR aperture was previously discussed by Peng[14] and Nakano *et al.*[15] However, e.g. Liu and Tsai[16] and Kikukawa *et al.*[6] have also considered the effects of the particle-type apertures (i.e., local regions of metallic nano-particles that are formed in the SR structure's active layer) in the SR systems. We state that such a particle SR aperture model is a more realistic (physical) model than the bulk metal-type aperture that we consider, but the bulk apertures are easier to model because the random particle systems introduce noise into the calculated reflected optical power I which means that statistical methods should be used to model such a system. Finally, in our modeling, the wavelength of the source is 650 nm and the numerical aperture of the objective lens is 0.6. Therefore the smallest resolvable mark size in the conventional system is $d_{RL} = 270$ nm.

In the simulations, a constant frequency (i.e., spatially periodic) mark train is located in the data layer. The marks are circular in shape (similar to those used by Peng[14]) and the diameter of the marks is varied between 50 nm and 600 nm. In addition, the spacing between the marks is always equal to the mark size. However, in this work, the SR aperture size is not the same as the mark size as was the case reported by Peng[14] and Nakano *et al.*[15] In addition, the rounded rectangle shaped marks, which correspond better to real mark shapes than do the circular shaped marks were also used in the simulations discussed herein. In Fig. 2 are shown three mark trains with different mark sizes and two mark types. The 150 nm diameter circular marks in Fig. 2(a) which also represent the shortest rounded rectangle shaped marks (cf. Fig. 2(c)) that can occur when the width of the latter type of mark is 150 nm (note thet the rounded rectangular marks are elongated in the scan direction of the focused playback light spot). The diameter of the circular mark in Fig. 2(b) is 300 nm and the length of the rounded rectangle shaped mark is 450 nm in Fig. 2(c). It can be assumed that the mark trains depicted in Figs. 2(a) and 2(b) will produce different playback signals, even thought the sizes of the marks are equal.

Finally, readout optical power modulation is calculated from the field that is incident on the detector. The modulation is obtained from the equation $M = I_{max} - I_{min}/I_{max} + I_{min}$, where I_{min} and I_{max} are the total optical powers which impinge on the OPU's readout photodetector

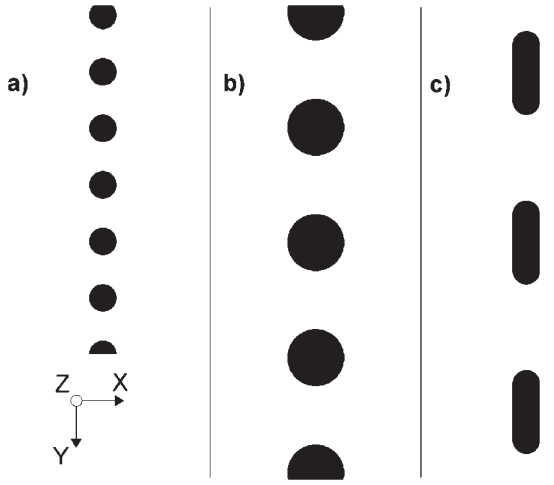

Fig. 2. Amorphous phase marks recorded in the crystal phase data layer. 150 nm diameter circular shaped mark train (a), 300 nm diameter circular mark train (b) and 450 nm long, 150 nm wide rounded rectangle shaped mark train (c). No land/groove structure has been used in the modeling, i.e. the marks lie in a planar data layer.

when the optical axis of the focused playback spot is located exactly on the centers of the amorphous marks and intervening crystalline spaces respectively. We assume that the optical power I at the detector plane can be interpolated between the simulated data points at which I_{min} and I_{max} are calculated. The modulation curves computed in this manner show some interesting features which will be described later. However, it should be remembered that, if the aforementioned assumption about using interpolation to obtain a continuous modulation curve does not hold, some features of the modulation curve are not correct. As an example, in Fig. 3 is shown the optical power at the on-mark (I_{min}) and off-mark (I_{max}) situations in the case of the conventional digital versatile disk (DVD)-type disk structure which is used to obtain reference readout signals for comparison with readout signals obtained from the SR disk systems. The DVD reference disk system is modeled as a three layer structure (cover, data and substrate layers) and the data

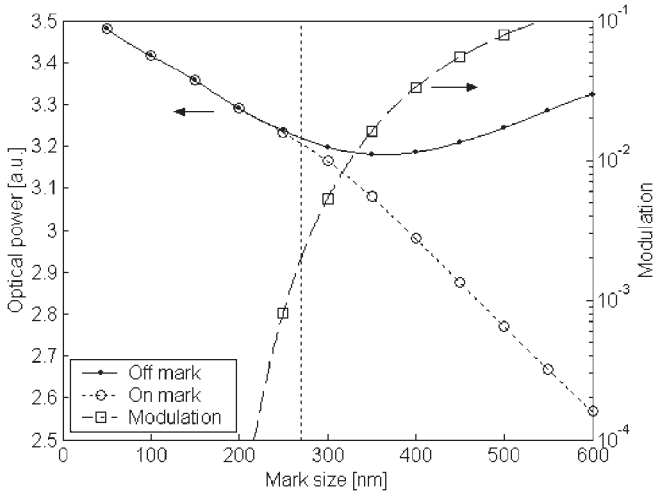

Fig. 3. I_{min} and I_{max} produced by the reference DVD system (left y-axis) and corresponding modulation (right logarithmic y-axis). Resolution limit ($\lambda/4$NA) is shown via the dotted vertical line.

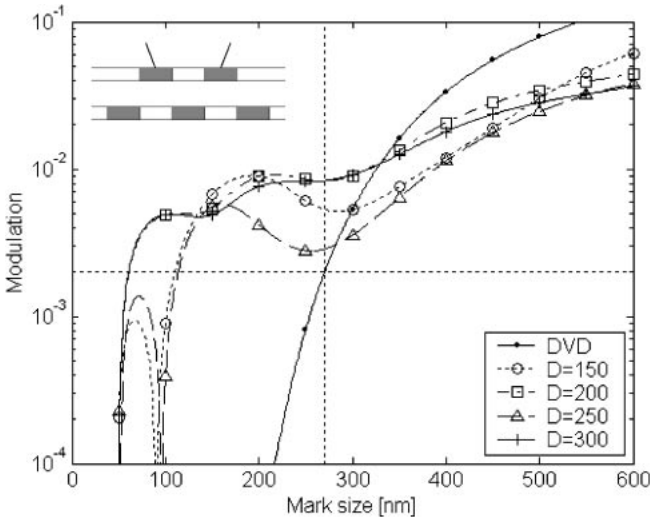

Fig. 4. Modulation from the donut shaped SR structure as a function of the mark size with different oxygen bubble diameters. Modulation from the DVD-type structure is shown as a reference. The outer diameter of the Ag donut is 3× the oxygen aperture. SR, spacer and data layer thicknesses are 15, 40 and 20 nm respectively. Resolution limit and level are shown with dotted lines. Inset shows the modeled structure.

marks have a circular shape (Fig. 2(b)) regardless of their size. The modulation produced by the reference DVD system is approximately 0.002 at the resolution limit of the conventional optical system. This modulation level is considered to correspond to the SNR of the readout signal, which is too low for reliable readout (when reasonable noise levels are assumed).

3. Results

In this section, results from the simulations are presented. Modulation as a function of the mark size from different SR apertures and thin film structure configuration are compared to the DVD type of structure.

In Fig. 4 is shown the optical power modulation as a function of the mark size with different oxygen apertures-Ag donut configurations. Oxygen aperture diameter D is varied between 150 nm and 300 nm and the outer radius of the Ag donut is 3R, where the R is the radius of the oxygen aperture. The Ag donut is the bulk material in all the simulations, and no small particles have been used. The improved performance over the conventional system is shown clearly with the small mark sizes (<300 nm). However the modulation with 150 nm and 250 nm diameter apertures goes to zero at around the 100 nm mark size. This is due to reversed I levels from the on-mark and off-mark locations. On the other hand, with 200 and 300 nm aperture sizes, the signals are not reversed and the usable modulation curve continues until about the 100 nm mark size after which it starts to decrease rapidly and reaches its minimum around the 50 nm mark. Even thought the modulations with 200 nm and 300 nm apertures are almost equal, the power with 200 nm diameter aperture is about 9% lower than with 300 nm aperture.

Similar readout modulation curves to those in Fig. 4 are shown in Fig. 5 for the LSC-type structure. This is the similar geometry that was used by Peng[14] and Nakano *et al.*[15] In Peng's study[14] however, the LSC diameter was always the same as the mark size ($D_{aperture} = D_{mark}$), but in

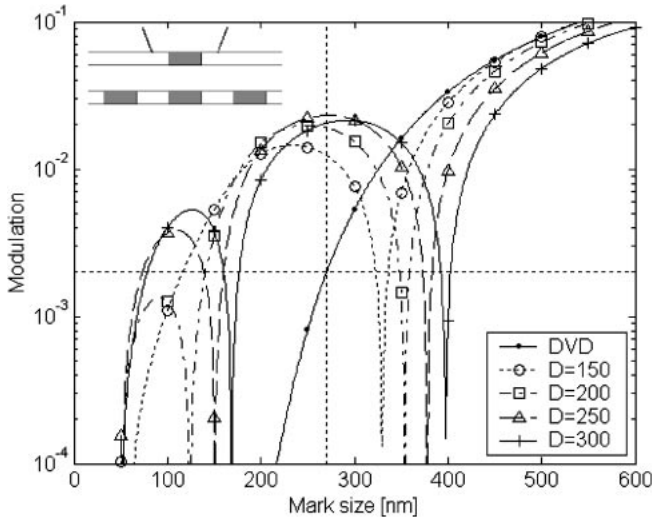

Fig. 5. Modulation from the LSC SR structure as a function of the mark size with different LSC diameters. Modulation from the DVD-type structure is shown as a reference. SR, spacer and data layer thicknesses are 15, 40 and 20 nm respectively. Resolution limit and level are shown with dotted lines. Inset shows the modeled structure.

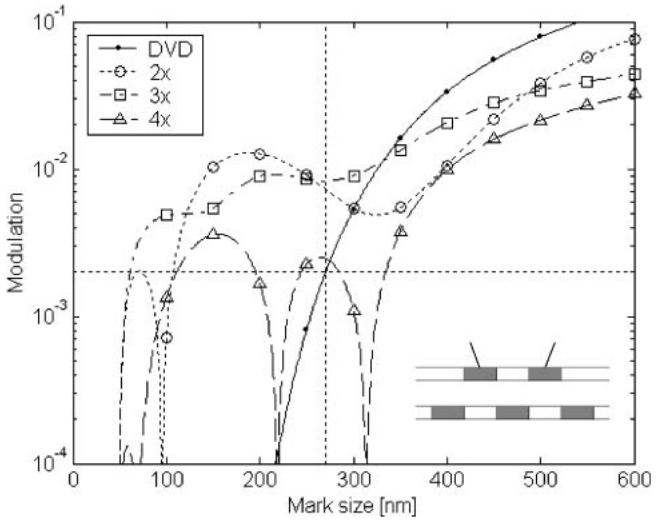

Fig. 6. Modulation from the donut shaped SR structure as a function of the mark size with different Ag donut outer diameters while oxygen aperture diameter is 200 nm. Modulation from the DVD-type structure is shown as a reference. SR, spacer and data layer thicknesses are 15, 40 and 20 nm respectively. Resolution limit and level are shown with dotted lines. Inset shows the modeled structure.

our simulations, the LSC diameter is fixed. The data marks that correspond to the Peng[14] simulations can be located in Fig. 4 and it can be seen that they are not exactly the same. In our simulations, the maximum is around the 270 nm mark size and the modulation is also higher (at the 270 nm mark, the modulation is about 0.023) than that in ref. 14. The modulation curves in Fig. 4 correspond to the E_z polarization in Fig. 12 in ref. 14. These differences most likely arise from the different material properties and the fact that in our simulations, the substrate is below the structure (first surface type recording media) whereas in Peng[14] (and Nakano *et al.*[15]) the illumination is through the substrate.

One interesting property with respect to the LSC structure, which is not reported in previous papers, is that there are periodic nulls in the modulation curve depending on the diameter of the LSC. Because if in the mark train there are different sized marks and the intensity level reverses from on-mark and off-mark situations at some point, one cannot tell whether there exists a mark or not. In that sense, the readout performance of the SR system is inferior to that of the conventional DVD disk. However, even with this structure, if the mark sizes in the disk can be chosen in such a way that the null point in the modulation curve is not crossed (e.g. mark size 130–350 nm, when the diameter of the LSC is 200 nm) the correct readout signal can be obtained.

In the next simulation set (Fig. 6), we changed the outer diameter of the Ag donut while keeping the inner diameter (diameter of the oxygen bubble) constant ($D = 200$ nm). First, it is seen that when the Ag donut diameter is 800 nm (4×) the readout performance of the SR system is actually worse than that of the conventional rewritable (RW) disk. There are three nulls at 70, 219 and 314 nm mark sizes. The large bulk Ag donut can be thought to operate as a silver thin film with the aperture at the optical axis. This structure functions as a mask layer and the transmission through the aperture is low and therefore the data cannot be read properly. When the Ag donut diameter is 400 nm (2×) the performance is much better and there is a null only at the 95 nm mark size. From these three cases it is seen that the readout performance is the best when the Ag donut diameter is 600 nm (3×). Even though there is some fluctuation in the modulation curve (local maximum at 200 nm mark size) there is no null in the curve until the drop at the 50 nm mark size. However, this test was only performed for such a small set of parameters that it is impossible to say that this is a global optimum structure. This merely shows that there can be huge differences in the performance when the aperture geometry is changed.

In the next phase, a 20 nm thick reflective Al layer (and the insulator layer between the reflector and data layers) was added below the data layer. A natural approach was to optimize the insulator and the spacer layer thicknesses. In Fig. 7 is shown the modulation from the 150 nm mark size, when the insulator thickness is changed between 10 and 60 nm. As a reference the curve (or the line) in the case, where there is no reflector layer, is plotted. The spacer layer thickness is 40 nm and the donut shaped SR structure is used and the diameter of the oxygen bubble is 200 nm. Now there is local maximum at the modulation curve when the insulator thickness is 15 nm. Of course, here we have not included any thermal effects into our model, so it may be possible that such a thin insulator is not practical for the heat transfer purposes. In addition, the performance with different mark sizes has not been taken into account.

In Fig. 8 is shown a similar layer optimization to that in Fig. 7, but for the spacer layer (the layer between the SR layer and the data layer). The insulator layer thickness is fixed at 20 nm and the aperture diameter and the mark size are the same as those in Fig. 7. The figure shows a clear maximum in the modulation at 60 nm layer thickness after which the modulation decreases significantly if the layer thickness is still increased. This behavior and also the curve

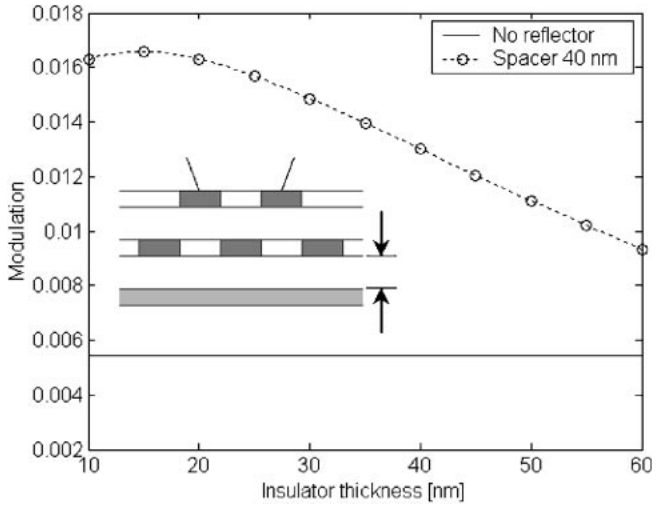

Fig. 7. Modulation from the donut shaped SR structure as a function of the insulator thickness. SR, spacer, data and reflector layer thicknesses are 15, 40, 20 and 20 nm respectively. Mark size is 150 nm and oxygen bubble diameter is 200 nm. Inset shows the modeled structure.

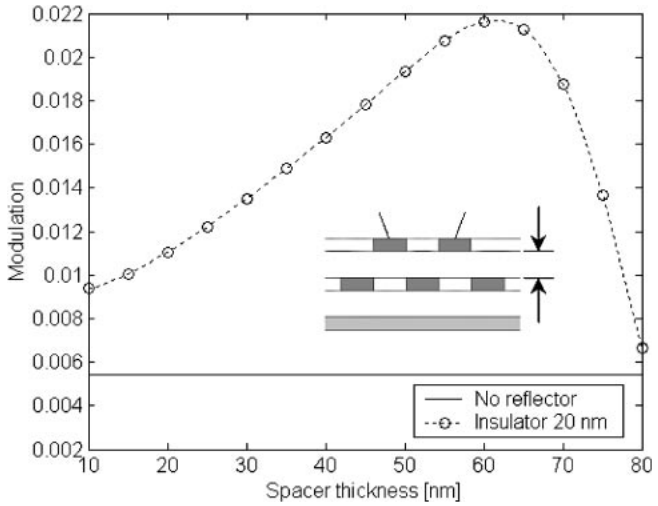

Fig. 8. Modulation from the donut shaped SR structure as a function of the spacer thickness. SR, data, insulator and reflector layer thicknesses are 15, 20, 20 and 20 nm respectively. Mark size is 150 nm and oxygen bubble diameter is 200 nm. Inset shows the modeled structure.

shown in Fig. 7 are most likely due to interference between the different thin film layers and global optimization of the whole disk layer structure is required. But, as shown in the previous figures, the SR aperture structure has significant effect on the modulation signal, therefore it is more important to determine the real SR structure before the layer structure is optimized for the best readout signal performance. Finally, the reader is reminded that the modulation was calculated only for one mark size.

In the following simulations, the mark shape is changed from circular to a rounded rectangle and the Al reflector layer is also used in the model. The reference curve without the SR layer is also calculated again in the case that in the conventional DVD there is a reflector layer. The insulator layer thickness in both the DVD and SR disk is 20 nm and the spacer layer thickness in the SR disk is 40 nm. However,

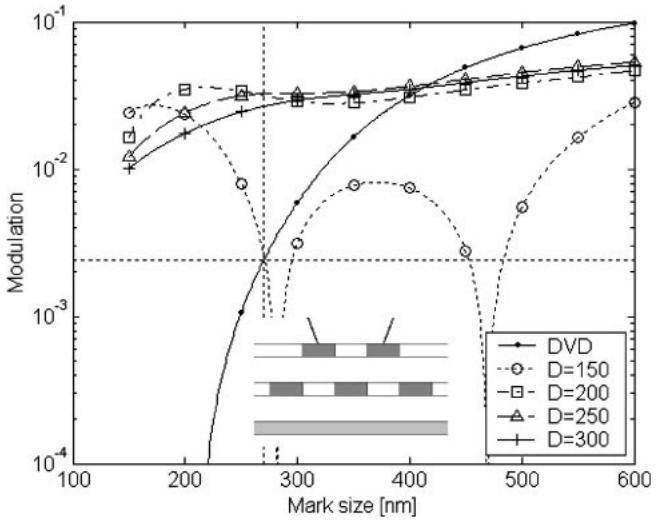

Fig. 9. Modulation from the donut shaped SR system as a function of the mark size with different oxygen bubble diameters. Modulation from the DVD-type structure is shown as a reference. SR, spacer, data, insulator and reflector layer thicknesses are 15, 40, 20, 20 and 20 nm respectively. Inset shows the modeled structure.

the disk land and groove structure has still not been used in the simulations. Now the modulation level from the DVD-type disk at the resolution limit is about 0.0024.

In Fig. 9 is shown relatively flat modulation when the donut shaped SR aperture is used in the simulations. Only with the smallest 150 nm diameter aperture, there exist nulls in the modulation curve. Even though, the modulations in the case of higher diameter apertures are close to each other, the optical powers are different. The relative mean powers at the detector are about 1.64, 1.97, 2.57, 3.15 and 2.34 for 150, 200, 250, 300 diameter oxygen bubbles and DVD respectively. Note also that the reference DVD system power is reduced compared to that shown in Fig. 3. In addition, there is a trend that with larger SR aperture diameter, the reflected power is higher. The superior modulation in comparison to that in Fig. 3 is mostly due to reflector layer used in the simulations. Note also that with the same layer thicknesses, the performance of the DVD-type structure is almost the same as that in Fig. 3 without reflector layer and with circular shaped marks.

Similar simulations to those shown in Fig. 9 for a donut shaped SR aperture were also performed using LSC SR aperture. The modulation curves are shown in Fig. 10. Improved performance over that of the reference system with small mark size is also seen. However, now there exist nulls with all aperture sizes when the mark size is between 420–530 nm. In addition, with the largest 300 nm LSC diameter, there is a null at the 160 nm mark size. As shown in Fig. 5, there is periodic type of null in the modulation curve, but in Fig. 10, the period of these nulls is longer than that in Fig. 5. Currently, we do not have an explanation for this periodic behavior of the readout power modulation, but this will be studied in more detail in the future work.

4. Discussion

In recent experiments it has been shown that a AgO_x layer is decomposed into small Ag particles and oxygen when it is

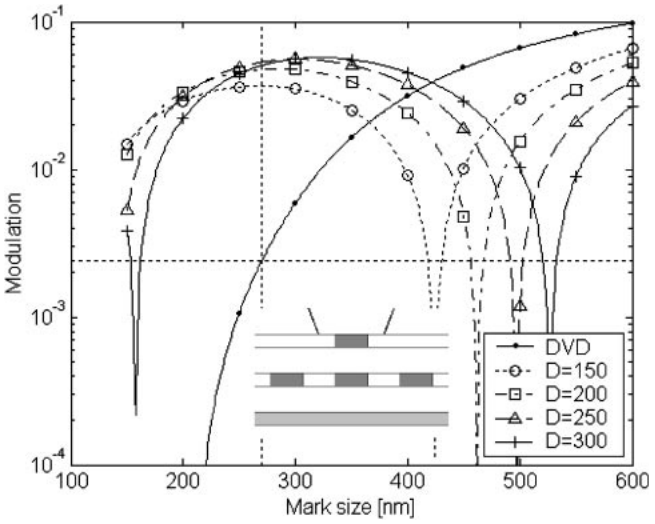

Fig. 10. Modulation from the LSC SR structure as a function of the mark size with different LSC diameters. Modulation from the DVD-type structure is shown as a reference. SR, spacer, data, insulator and reflector layer thicknesses are 15, 40, 20, 20 and 20 nm respectively. Inset shows the modeled structure.

heated with a focused laser beam. In addition, the whole SR, spacer and data layer structure is permanently damaged and it operates only as write once media.[5] A similar effect was also shown for the PtO_x material.[6] However, in our model, the aperture exists only in the region which is heated by the readout laser beam and the SR aperture structure is considered to function as a dynamical window. If one considers the case where there is always an aperture in the same location at which there is a mark present (write once media), the readout process modeled in this paper does not hold anymore. Nevertheless, we have shown that both LSC and donut shaped SR structures exhibit improved performance over the conventional phase change disk and because both these types of structures have been observed in experiments[12] we believe that the behaviors of these structures (especially the donut shaped SR aperture) are close to the real behavior of the metallic SR structures. Here, we note that in a recent work, Lin *et al.*[17] reported a donut shaped aperture when a Ag particle system is illuminated with a readout laser spot. Therefore we suggest that donut shaped aperture model can be used in the numerical simulations to study the performance of the SR disks. Finally, the reason for the change in the signal power levels at the detector from the on-mark and off-mark situations and therefore the null point in the modulation curve need to be studied in more detail, but this is left for future work.

5. Conclusion

Readout characteristics of two bulk types of Ag SR structures were studied using the 3-dimensional (3D) FDTD method. The proposed oxygen aperture system using a bulk Ag donut is currently closest to the experimental data which can explain the improved readout performance from the SR disk. However, in reality, the AgO_x layer decomposes into small particles instead of a bulk sheet of Ag and the readout characteristics of such a particle aperture might have different performance. Finally, the reversed signal levels are shown as a null in the modulation curve.

Acknowledgement

Jerome Moloney and Aramais Zakharian (Arizona Center for Mathematical Sciences, University of Arizona) are acknowledged for providing the original 3D FDTD code. Kari Kataja acknowledges the support of the Tauno Tönning Foundation and the Foundation of Technology.

1) E. Betzig, J. K. Trautman, R. Wolfe, E. M. Gyorgy, P. L. Finn, M. H. Kryder and C. H. Chang: Appl. Phys. Lett. **61** (1992) 142.
2) A. Partovi, D. Peale, M. Wuttig, C. A. Murray, G. Zydzik, L. Hopkins, K. Baldwin, W. S. Hobson, J. Wynn, G. Lopata, L. Dhar, R. Chichester and J. H.-J. Yeh: Appl. Phys. Lett. **75** (1999) 1515.
3) J. Tominaga, T. Nakano and N. Atoda: Appl. Phys. Lett. **73** (1998) 2078.
4) H. Fuji, J. Tominaga, L. Men, T. Nakano, H. Katayama and N. Atado: Jpn. J. Appl. Phys. **39** (2000) 980.
5) T. Kikukawa, A. Tachibana H. Fuji and J. Tominaga: Jpn. J. Appl. Phys. **42** (2003) 1038.
6) T. Kikukawa, T. Nakano, T. Shima and J. Tominaga: Appl. Phys. Lett. **81** (2002) 4697.
7) J. Kim, I. Hwang, D. Yoon, I. Park, D. Shin, T. Kikukawa, T. Shima and J. Tominaga: Appl. Phys. Lett. **83** (2003) 1701.
8) J. Tominaga, J. Kim, H. Fuji, D. Büchel, T. Kikukawa, L. Men, H. Fukuda, A. Sato, T. Nakano, A. Tachibana, Y. Yamakawa, M. Kumagai, T. Fukaya and N. Atoda: Jpn. J. Appl. Phys. **40** (2001) 1831.
9) J. Tominaga, C. Mihalcea, D. Büchel, H. Fukuda, T. Nakano, N. Atoda, H. Fuji and T. Kikukawa: Appl. Phys. Lett. **78** (2001) 2417.
10) A. Taflove and S. C. Hagness: *Computational Electrodynamics: The Finite-Difference Time-Domain Method* (Artech House, Boston, 2000).
11) G. Bao, L. Cowsar and W. Masters: *Mathematical Modeling in Optical Sciences* (SIAM, 2001).
12) F. H. Ho, H. H. Chang, Y.-H. Lin and D. P. Tsai: Jpn. J. Appl. Phys. **42** (2003) 1000.
13) Y.-C. Her, Y.-C. Lan, W.-C. Hsu and S.-Y. Tsai: Appl. Phys. Lett. **83** (2003) 2136.
14) C. Peng: Appl. Opt. **40** (2001) 3922.
15) T. Nakano, Y. Yamakawa, J. Tominaga and N. Atado: Jpn. J. Appl. Phys. **40** (2001) 1531.
16) W. C. Liu and D. P. Tsai: Jpn. J. Appl. Phys. **42** (2003) 1031.
17) B. S. Lin, D. P. Tsai and W. C. Lin: Tech. Dig. ISOM03 (2003) Th-H-02.

Series title, number and report code of publication

VTT Publications 745
VTT-PUBS-745

Author(s)
Juuso Olkkonen

Title

Finite difference time domain studies on sub-wavelength aperture structures

Abstract

Modern optical technologies, such as microscopy, data storage, and lithography, require optical light spots with lateral dimensions that are much smaller than the wavelength of incident light. In free space, no such light spots are known to exist due to diffraction – a phenomenon exhibited by all electromagnetic waves. In this thesis, the formation of highly confined light spots by means of sub-wavelength aperture structures in metal films is studied via finite difference time domain (FDTD) simulations. It is observed that the otherwise weak light transmittance through sub-wavelength apertures can be remarkably enhanced by filling the aperture by a high refractive index material. The transmittance through the aperture can be further increased by introducing surface corrugations that couple the light impinging outside the aperture into surface waves propagating along the film plane. It is also demonstrated that significant transmission enhancement is obtained by inserting a semitransparent metal film in front of the aperture at the distance that fulfills the Fabry-Pérot resonance condition. The gap between the semitransparent metal film and the film containing the aperture works as a light trapping cavity, enhancing the amplitude of the illuminating monochromatic plane wave.

A simple scattered field technique that allows FDTD modeling scattering of obliquely incident plane waves from objects residing in a dispersive multilayer background structure is introduced in this work. The technique is applied to study how a surface plasmon polariton field that is excited in the traditional Otto configuration couples to a 100 nm wide slit in a metal film.

As an application example of the aperture structures, the effect of the embedded non-linear aperture layer in the traditional DVD disk on the data storage density is studied via the 3D FDTD method. It is found that the aperture layer enables distinguishing of data marks smaller than 100 nanometers in the far field, making it possible to increase the storage density of DVD disks by a factor of four.

ISBN
978-951-38-7410-0 (soft back ed.)
978-951-38-7411-7 (URL: http://www.vtt.fi/publications/index.jsp)

Series title and ISSN
VTT Publications
1235-0621 (soft back ed.)
1455-0849 (URL: http://www.vtt.fi/publications/index.jsp)

Project number
35768

Date
October 2010

Language
English, Finnish abstr.

Pages
76 p. + app. 52 p.

Name of project

Commissioned by

Keywords
finite difference time domain method, apertures in metal films, surface plasmon polaritons, data storage

Publisher
VTT Technical Research Centre of Finland
P.O. Box 1000, FI-02044 VTT, Finland
Phone internat. +358 20 722 4520
Fax +358 20 722 4374

Julkaisun sarja, numero ja raporttikoodi

VTT Publications 745
VTT-PUBS-745

Tekijä(t)
Juuso Olkkonen

Nimeke

FDTD-tutkimuksia aallonpituutta pienemmistä apertuurirakenteista

Tiivistelmä

Modernit optiset teknologiat, kuten mikroskopia, tiedontallennus ja litografia, tarvitsevat optisia valopisteitä, joiden lateraalidimensiot ovat paljon pienempiä kuin valon aallonpituus. Vapaassa tilassa tällaisia valopisteitä ei tiedetä esiintyvän johtuen diffraktiosta – ilmiö, jota kaikki sähkömagneettiset aallot noudattavat. Työssä tutkitaan FDTD (Finite Difference Time Domain) -menetelmää käyttäen hyvin pienten valopisteiden muodostamista alle valon aallonpituuden kokoluokkaa olevilla apertuurirakenteilla metallikalvoissa. Työssä havaitaan, että apertuurien hyvin alhaista valonläpäisykykyä voidaan parantaa merkittävästi täyttämällä apertuuri korkean taitekertoimen materiaalilla. Valonläpäisyä voidaan lisäksi kasvattaa ympäröimällä apertuuri pintaurilla, jotka kytkevät apertuurin ympäristöön osuvan valon metallikalvon pintaa pitkin eteneviksi pinta-aalloiksi. Työssä myös demonstroidaan, että merkittävä läpäisykyvyn lisäys saavutetaan asettamalla puoliläpäisevä metallikalvo apertuurin eteen etäisyydelle, joka täyttää Fabry-Pérot-resonanssiehdon. Rako puoliläpäisevän ja apertuurin sisältävän metallikalvon välissä toimii valoloukkuna, joka kasvattaa valaisevan monokromaattisen tasoaallon amplitudia.

Työssä esitetään sirontakenttämenetelmä, jonka avulla voidaan FDTD-menetelmää käyttäen mallintaa, kuinka viistosti valaiseva tasoaalto siroaa dispersiivi¬sessä monikerrosrakenteessa olevista sirottajista. Menetelmää käyttäen tutkitaan, kuinka perinteisessä Otto-konfiguraatiossa herätetty pinta-plasmonaalto kytkeytyy 100 nm leveään rakoapertuurin metallikalvossa.

Apertuurirakenteiden sovellusesimerkkinä tutkitaan kolmiulotteisen FDTD-menetelmän avulla DVD-levyn sisässä olevan epälineaarisen apertuurikerroksen vaikutusta tiedontallennustiheyden kasvattamiseen. Havaitaan, että apertuurikerros mahdollistaa alle 100 nm:n kokoisten datamerkkien havaitsemisen kaukokentässä, mikä mahdollistaa DVD-levyjen tallennustiheyden kasvattamisen nelinkertaiseksi.

ISBN
978-951-38-7410-0 (nid.)
978-951-38-7411-7 (URL: http://www.vtt.fi/publications/index.jsp)

Avainnimeke ja ISSN	Projektinumero
VTT Publications 1235-0621 (nid.) 1455-0849 (URL: http://www.vtt.fi/publications/index.jsp)	35768

Julkaisuaika	Kieli	Sivuja
Lokakuu 2010	Suomi, engl. tiiv.	76 s. + liitt. 52 s.

Projektin nimi	Toimeksiantaja(t)

Avainsanat	Julkaisija
finite difference time domain method, apertures in metal films, surface plasmon polaritons, data storage	VTT PL 1000, 02044 VTT Puh. 020 722 4520 Faksi 020 722 4374

The squeezing of light into the sub-wavelength domain is a subject of utmost importance – in respect of both applications and the fundamental theory of light. This thesis considers the formation of tiny light spots by means of sub-λ apertures in metal films. When a light field interacts with an aperture, strong evanescent waves as well as surface charges and currents are constituted into the aperture and its vicinity, strongly influencing the transmission properties of the aperture. Accurate modeling of the interaction requires all the field components to satisfy Maxwell's equations and appropriate boundary conditions. Thus, scalar diffraction theories are not adequate, and the modeling must resort to methods based directly on Maxwell's equations. In this thesis, the finite difference time domain (FDTD) method that discretizes Maxwell equations in both time and space is used as the main modeling tool. Calculation times are shortened using parallel computing.

The thesis demonstrates via FDTD simulations that by tuning the geometrical shape, the dielectric filling, and the surface structure as well as the polarization state of incident light, optical transmission properties of sub-λ apertures in metal films can be altered drastically. The sub-λ apertures and aperture arrays are certain to benefit a variety of applications. Examples include super-resolution data storage, heat assisted magnetic recording, optical microscopy, Raman spectroscopy, biosensors, optical filters, polarizers, transparent electrodes for displays and solar cells, beam shaping and near-field focusing.

ISBN 978-951-38-7410-0 (soft back ed.)
ISSN 1235-0621 (soft back ed.)
ISBN 978-951-38-7411-7 (URL: http://www.vtt.fi/publications/index.jsp)
ISSN 1455-0849 (URL: http://www.vtt.fi/publications/index.jsp)